# Nickel Production in 1D-CCSNe

## Triggered by Different Explosion Mechanisms

**Liliya Imasheva**


München 2022

# Nickel Production in 1D-CCSNe
## Triggered by Different Explosion Mechanisms

**Liliya Imasheva**

Dissertation
der Fakultät für Physik
der Ludwig-Maximilians-Universität
München

vorgelegt von
Liliya Imasheva
aus Russland

München, den 30.09.2022

Erstgutachter: Prof. Dr. Achim Weiss
Zweitgutachter: PD Dr. Klaus Dolag
Tag der mündlichen Prüfung: 24.11.2022

# Contents

# List of Figures

# List of Tables

# Zusammenfassung

Simulationen der Kernkollaps-Explosionen in Kugelsymmetrie sind sehr wichtig, um den Ursprung der Elemente im Universum zu verstehen. Bei der Verwendung 1D künstlicher Explosionsmechanismen ist es wesentlich, die Einschränkungen der Modelle zu verstehen, da dies zu einer Fehlinterpretation der Ergebnisse der Simulationen führen könnte.

In dieser Arbeit präsentiere ich einen Überblick über drei verschiedene 1D Explosionsmechanismen: thermische Bombe, stoss- und neutrinogetrieben Explosionen. Thermische Bomben- und stossgetrieben Explosionen sind flexibel im Parameterraum, daher ist es wichtig, die Grenzen der Mechanismen zu verstehen. Ich vergleiche die Ergebnisse dieser beiden Mechanismen mit den neutrinogetriebenen Explosionen als realistischerem Mechanismus. Als Indikator für den Vergleich verwende ich die bei der Explosion entstehende Endmasse von $^{56}$Ni, da diese aus der Lichtkurvenmodellierung gewonnen werden kann, und vergleiche sie mit dem errechneten Wert.

Zunächst betrachten wir die Explosionen von thermischen Bomben mit und ohne Kollapsphase. Die Simulation der Explosion mit einer nicht kollabierten thermischen Bombe führt zu der klaren Abhängigkeit der endgültigen Nickelmasse von der Zeitskala der Energieinjektion. Es zeigt sich, dass die langsameren Explosionen dazu neigen, die Nickelproduktion zu unterdrücken, was den Ergebnissen von 3D Simulationen widerspricht. Die Simulation einer thermischen Bombe mit einer Kollapsphase zeigt jedoch, dass diese Abhängigkeit eine klare Folge des Nichtkollabierens des Kerns war, da die Nickelmasse in diesen Modellen tatsächlich nicht von der Zeitskala der Energieinjektion abhängt. Darüber hinaus haben wir auch überlegt, andere Parameter der Explosion mit thermischen Bomben zu ändern, wie z. B. die Umstellung auf die Energieinjektion im festen Volumen anstelle der Masse und die Änderung des Mindestradius für den Kollaps. Es ist ziemlich klar, dass das Verhalten der endgültigen Nickelmasse sehr empfindlich auf die Details der Explosion durch die thermische Bombe reagiert.

Dann wurde der Vergleich von drei Explosionsmechanismen: thermische Bombe, stossgetrieben und Neutrinoantrieb, vorgestellt. Stossgetrieben Explosionen neigen dazu, Nickel während der Explosion überzuproduzieren, was durch den späten Rückfall von Materie kompensiert wird. Wir haben uns auch die detaillierten Nukleosynthese-Berechnungen für alle Mechanismen für Alpha-Elemente und für die Kerne der Eisengruppe angesehen. Wir haben gesehen, dass mehr Isotope der Kerne der Eisengruppe in den innersten Regionen für die neutrinogetriebenen Explosionen produziert werden, wodurch sich die Nukleosynthese für diesen Mechanismus ziemlich von den anderen Mechanismen unterscheidet.

# Abstract

Simulations of the core collapse supernova explosions in spherical symmetry are quite important for understanding the source of the elements in the Universe. When using one dimensional artificial explosion mechanisms it is essential to understand the limitations of the models because it could lead to misinterpreting the results of the simulations.

In this thesis I am presenting the overview of three different 1D explosion mechanisms, thermal bomb, piston and neutrino-driven explosions. Thermal bomb and piston driven explosions are rather simple mechanisms, and they are flexible in the parameters space. Therefore, it is important to understand the limitations of the mechanisms. I compare the results of these two mechanisms to the neutrino driven explosions, a more realistic mechanism. As a diagnostic for the comparison I use the final mass of $^{56}$Ni produced in the explosion, since it can be obtained from light curve modeling, and compared to the calculated value.

First, we consider the thermal bomb explosions with and without a collapse phase. Simulating the explosion with an uncollapsed thermal bomb leads to the clear dependence of the final nickel mass on the energy deposition timescale; namely, the slower explosions tend to suppress the nickel production, which in fact contradicts the results of 3D simulations. Simulating a thermal bomb with a collapse phase, however, shows that this dependence was a clear consequence of not collapsing the core, because the nickel mass is actually almost independent of the energy deposition time in these models. On top of that, we also considered changing other parameters of thermal bomb explosions, such as switching to the energy deposition in the fixed volume instead of mass, and changing the minimum radius for the collapse. It is rather clear that the behavior of the final nickel mass is very sensitive to the setup of the thermal bomb explosion.

Next, the comparison of three explosion mechanisms, thermal bomb, piston, and neutrino driven, was presented. Piston driven explosions tend to overproduce nickel during the explosion, which is compensated by the late fallback. We also looked at the detailed nucleosynthesis calculations for all the mechanisms for alpha elements and for the iron group nuclei. We saw that more isotopes of the iron group nuclei are produced in the innermost regions for the neutrino driven explosions making the nucleosynthesis for this mechanism quite different from the rest of the mechanisms.

# Chapter 1

# Introduction

Everything we can see, when we look up at night, is basically a result of nuclear reactions in stars. It is fascinating to think how far away and how huge these objects are, but we can still see them with a naked eye, and moreover learn so much about them. Most of the elements we consist of were produced during the lives and deaths of stars. Nucleosynthesis studies in this context investigate the composition of stars and ultimately give us the answer to the question, what did we form from? So let me briefly define the role of the present work in this exciting process.

## 1.1 Element Production and CCSN

Any star is a cloud of gas at the beginning of its life, consisting mostly of hydrogen and helium. From the start there are two competing forces. On one hand we have gravity forcing the star to contract and to raise its temperature, and on the other hand we have pressure which is resisting gravity and prevents the stellar structure from collapsing. When the temperature is high enough, hydrogen starts to fuse into helium, producing additional energy. This process with competing forces is then repeated leading to a further increase of temperature and to helium being fused into the next so-called alpha elements: $^{12}$C, $^{16}$O, $^{20}$Ne, $^{24}$Mg, $^{28}$Si, $^{32}$S, etc. During these processes of fusion other elements and other isotopes are produced as well making stars one of the primary sources of elements in the Universe.

The point at which the fusion process stops is defined based on the initial mass of the star, which is also called a zero-age main sequence mass, $M_{\mathrm{ZAMS}}$. For massive stars ($M_{\mathrm{ZAMS}} \geq 8M_{\odot}$, where $M_{\odot} \approx 2 \cdot 10^{33}$ g is the solar mass) the fusion will proceed up to the iron group nuclei: $^{56}$Fe and $^{56}$Ni. After iron group isotopes, the fusion reactions cease to produce energy and become endothermic, since the binding energy per nucleon reaches its highest value for the mass number $A \sim 56$. This can be seen on Figure 1.1 showing the binding energy per nucleon $E_{\mathrm{B}}/A$ as a function of their mass number $A$. It represents how tightly bound the isotopes are, and it reaches its highest value for the isotope $^{56}$Fe (8.8 MeV/nucleon) meaning that the reactions that go in the direction of iron are releasing

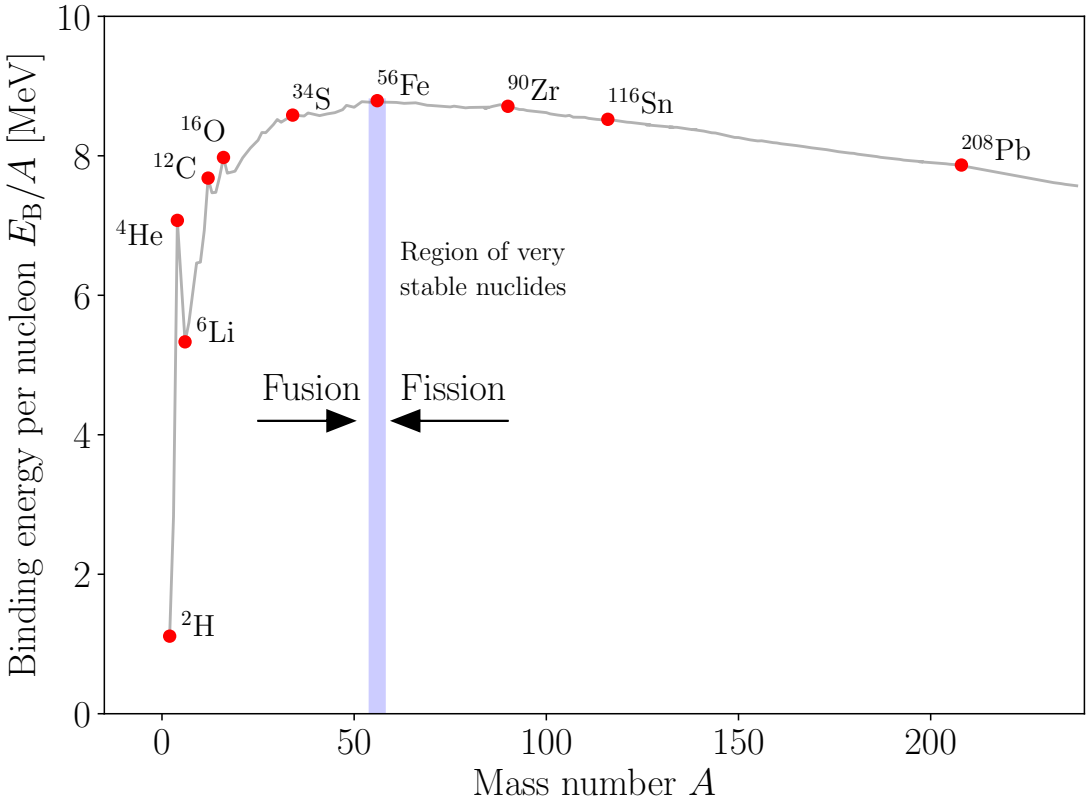


Figure 1.1: Binding energy per nucleon $E_B/A$ as a function of the mass number $A$, experimental values (Ghahramany et al., 2012).

energy.

In this way, at the end of its evolution, a massive star consists of concentric shells of the ashes of the previous core burning stages. In a simplified picture, it looks like Figure 1.2, and it is called an onion shell structure. Shells of progressively heavier elements contain the ashes of nuclear burning stages which finally build up a degenerate core of iron-group elements at the center. At this point, the composition of a massive star consists of many different elements from hydrogen to iron.

Massive stars end their lives in a collapse of the core and a subsequent violent explosion which is called a core collapse supernova (CCSN). During the explosion, the density, and temperature of the star are changing drastically inducing the synthesis of heavier and heavier new elements. These events are of a particular interest because they lead to the ejection of the envelope of the star into the interstellar medium, and this envelope consists of the elements produced during stellar evolution as well as the elements synthesized in the explosion. Just like that, the massive stars produce new elements and their explosions help to distribute them.

Understanding the origin of the elements is as challenging as it is fascinating. In Figure 1.3 one can see the mass fraction of different elements, $X$, as a function of their

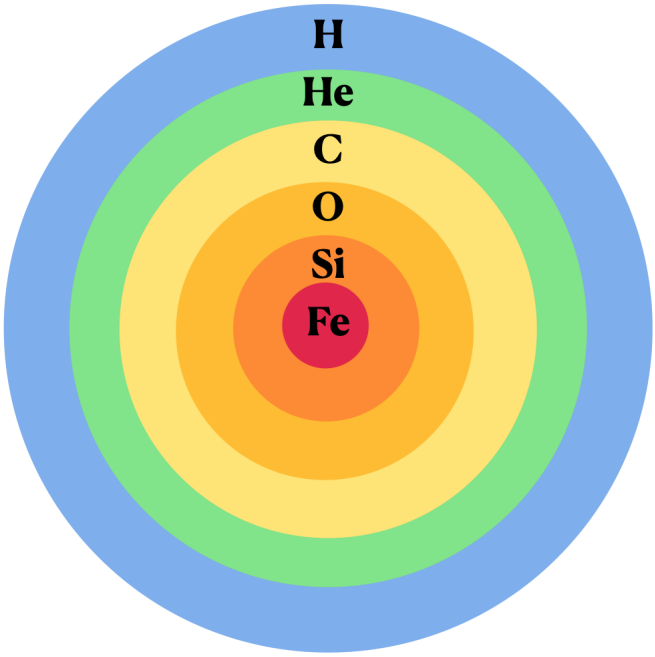


Figure 1.2: Onion-shell structure of a supernova progenitor star before the onset of stellar core collapse.

mass number, $A$, in our Solar System. This figure basically demonstrates how abundant the isotopes are in the nature. The mass fraction is the highest for hydrogen, meaning that our world mainly consists of hydrogen. The next most abundant element is helium, followed by a drop of the mass fractions, and a big peak around $A = 56$ corresponding to the iron group nuclei. There is a decline in the mass fractions after the iron peak, which can be understood from Figure 1.1; elements heavier than iron are less tightly bound than the iron group nuclei, and the fusion reactions will no longer be exothermic for these elements making them less frequent in nature. There are also certain patterns, visible on both, Figure 1.1 and Figure 1.3, showing higher mass fractions for more stable nuclei $^{4}$He, $^{12}$C and $^{16}$O. These nuclei have a higher binding energy per nucleon than their neighbors due to their inner structure, and they are also more abundant in nature. The behavior of the element distribution of our Solar System has led to a conclusion that the elements heavier than helium are produced in stars, while hydrogen and helium are mostly synthesized during the Big Bang nucleosynthesis (Burbidge et al., 1957; Hoyle et al., 1956).

Explosions of massive stars serve both to disperse the elements synthesized in massive stars during their evolution and to synthesize and disperse new elements themselves, and they are in fact one of the most important sources of heavy elements. Elements heavier than boron are mostly synthesized in stars or their explosions. Studying them can give us information on abundances of different elements. This leads to a better understanding of the stellar nucleosynthesis and chemical evolution of galaxies.

This question is addressed from two sides, that I will briefly discuss in the next sections.

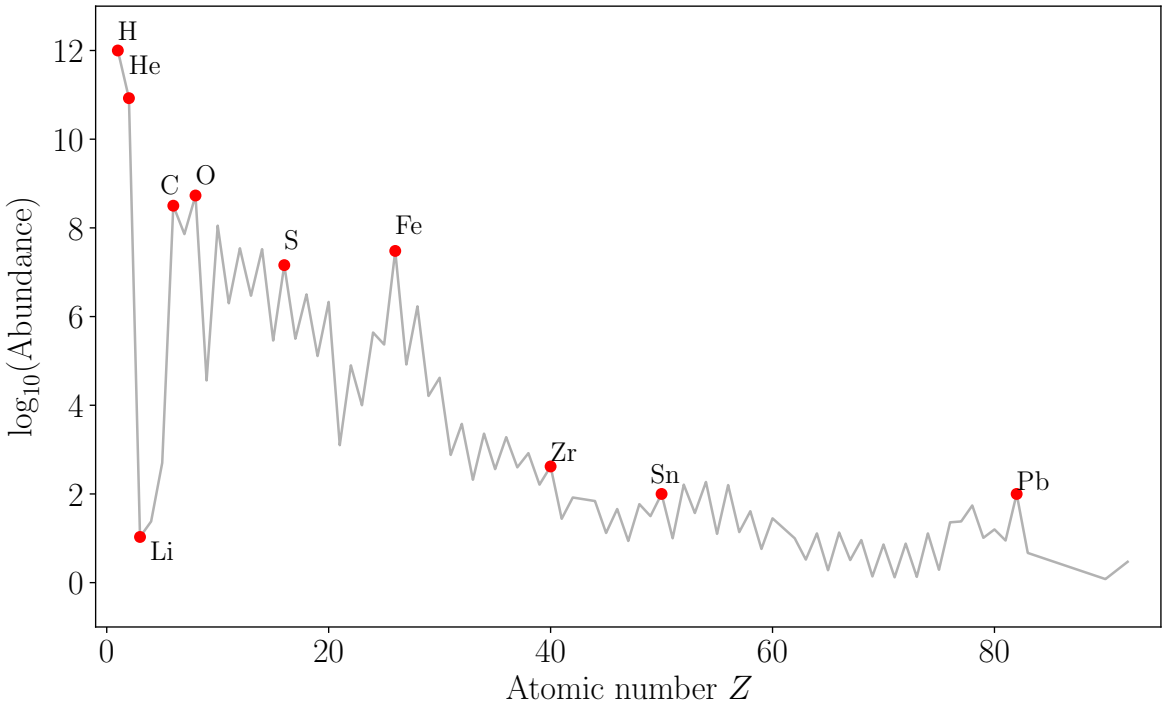


Figure 1.3: Solar photospheric abundances where the abundance of hydrogen is normalized to $10^{12}$ (Palme et al., 2014).

First, there are observational data obtained from different sources. And second, there are works on simulating the CCSN events which are constrained by observations. There are common features in the works studying nucleosynthesis in CCSN that I will also mention in this chapter.

## 1.2 Observations

There are several supernovae that have been observed. The oldest ones start already at the time before telescopes were available, so it was only possible to observe them with a naked eye. One of these historic events was SN 1054, a CCSN observed by Chinese astronomers. A compact remnant was left after the explosion, which is called the Crab nebula. Even though SN 1054 was not observed with the appropriate tools when it happened, modern observations are able to take a closer look at the remnant indicating the following properties: it was a massive star at the low-mass end for CCSNe, $\sim 8 - 10 M_{\odot}$ (Nomoto et al., 1982; Hester, 2008), which exploded with a low explosion energy, $\sim 10^{50}$erg = 0.1B, and little nickel ejecta masses (Smith, 2013; Yang and Chevalier, 2015).

Next, I want to mention a more energetic supernova SN1987A which was observed in February 1987 in the Large Magellanic Cloud (LMC). On Figure 1.4 there is an artist's impression of SN1987A, and it is based on real data from ALMA, Hubble and Chandra.

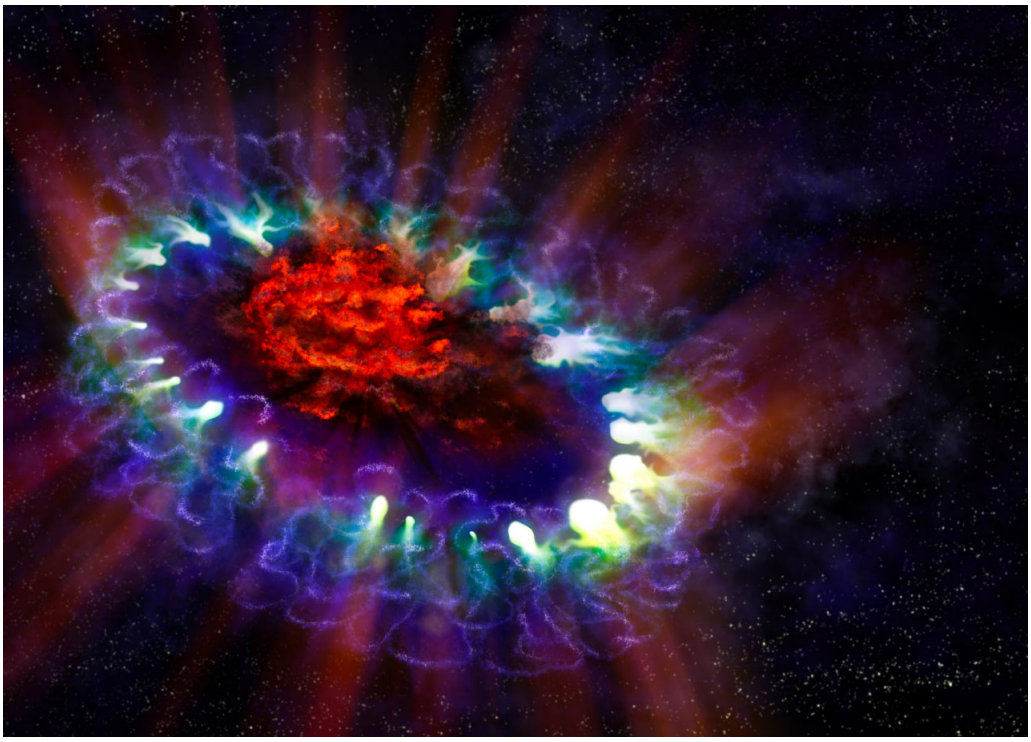

Figure 1.4: Artist's impression of the data obtained for SN1987A from different sources. Credit: A. Angelich; NRAO/AUI/NSF.

ALMA data (radio, in red) shows newly formed dust in the center of the remnant. It reveals the cold, inner regions of the remnant where tremendous amounts of dust were detected and imaged by ALMA. Hubble (visible, in green) and Chandra (X-ray, in blue) data show the expanding shock wave. This inner region is contrasted with the outer shell, the white and blue circles, where the blast wave from the supernova is colliding with the envelope of gas ejected from the star prior to its powerful detonation.

This supernova is special in a sense that it is the closest known SN for $\sim$ 300 years, so it is a very well studied case and one of the most important observations available to constrain supernova physics. The explosion energy measured for this SN is $\approx 1.5 \cdot 10^{51}$erg and the nickel ejecta mass, obtained from light curve modeling, is $0.07 M_{\odot}$ (Arnett et al., 1989; Bouchet et al., 1991; Suntzeff et al., 1992; Utrobin et al., 2015). The explosion energy is basically the kinetic energy of the material ejected from the star at infinity (Aufderheide et al., 1991). This quantity is the one that is observed in the ejecta and compared to calculated values. The progenitor star was identified to be a blue supergiant. This was unexpected at that time; a blue supergiant is more compact than a red supergiant and was therefore thought to be harder to explode.

Another observational source for SN research is the population of compact objects. The measured gravitational masses range from $\sim 1 M_{\odot}$ to a current upper limit of $\sim 2 M_{\odot}$ (Demorest et al., 2010). The upper limit imposes an important constraint on the equation

of state at high densities. Gravitational wave observations are expected to deduce a mass distribution for compact objects over time.

In the context of observations, we can see that crucial quantities here are the explosion energy, $E_{\rm exp}$, nickel mass, $M_{\rm Ni}$, and remnant mass, or the mass of the proto-neutron star, $M_{\rm PNS}$. These numbers can be used as reference for the modeling approaches of CCSN.

## 1.3 Simulations and Challenges

The details of the core-collapse supernova (CCSN) physics will be discussed in the next chapter, while here I would like to mention the challenges of its simulations. CCSN explosions have long been studied in spherical symmetry (1D) as well as with multidimensional modeling, and they both have their own advantages and goals. Both axisymmetric 2D (Müller, 2015; Bruenn et al., 2016; Chatzopoulos et al., 2016; Harris et al., 2017; Burrows and Vartanyan, 2021) and ab-initio 3D simulations (Takiwaki et al., 2014; Lentz et al., 2015; Janka et al., 2016; Müller et al., 2019; Ott et al., 2018; Burrows et al., 2020; Obergaulinger and Aloy, 2021; Bollig et al., 2021) are very essential for understanding the underlying physics of the explosion in all the details, showing the processes that are responsible for the explosion, like the development of the convective motions and hydrodynamic instabilities, stagnation, and revival of the shock wave, and the interactions with neutrinos (Murphy et al., 2013; Couch and Ott, 2015; Radice et al., 2016; Wongwathanarat et al., 2017; Glas et al., 2019). These simulations with detailed microphysics are computationally too expensive to allow long-term investigations. One very important consequence is that the simulations often do not continue long enough for the explosion energy to saturate, and it is critical in discussing the nucleosynthesis. There have been improvements in this area recently though, and this issue might be resolved in the near future. In the results from Bollig et al. (2021) the 3D simulations of CCSN were performed where they managed to continue the simulations until 7 seconds after bounce with the final energy of $\sim 1$ B, which appeared to be effectively saturated. It is quite close to the observed value of SN 1987.

With all the success of 3D modelling, there are still constraints that have to be taken into account. Due to their complexity, even with modern supercomputers, only a limited number of selected cases can be simulated and followed for at most a few seconds. But, there are several reasons why studies are needed that cover the whole range of the parameters such as an initial progenitor mass, a metallicity, and even binary evolution phases. For example, since the CCSNe contribute significantly to the galactic chemical evolution (Timmes et al., 1995; Matteucci, 2003; Hayden et al., 2015; Kobayashi et al., 2020; Wirth et al., 2021), the calculations over a large parameter space are essential for the understanding of the origin of the elements. Similarly, the statistics of the resulting compact objects, neutron stars or black holes, requires such studies (Ertl et al., 2016; Pejcha and Thompson, 2015). Here an important advantage of 1D models comes into play. They can be calculated systematically for various progenitor models, from the onset of the explosion till late times (Umeda and Yoshida, 2017, and references therein). These simulations are not intended to perfectly match observational properties, but are extremely useful in the looking at some

general trends over the large range of the progenitors.

So, 1D simulations are still widely used in the community, also for answering nucleosynthesis related questions. In spherical symmetry there are no instabilities supporting the explosion in 3D so it has to be induced artificially through explosion mechanisms. Typically, all the explosion mechanisms subject a region of the star to an additional stimulus which generates a shock wave. Spherically symmetric models have succeeded in explaining observational properties of individual SN events. These simulations are usually calibrated and constrained by observations. In this work, I will only discuss the spherically symmetric explosion models.

## 1.4 Common Features and Structure of this Work

There are common features of studying nucleosynthesis in 1D explosions in the literature. First, there is a progenitor model, which is the result of stellar evolution simulations. It basically consists of density, temperature, composition and other quantities as a function of the stellar radius or mass. Based on the progenitor model, the initial pre-collapse model is constructed for the explosion simulations. This step might include remapping of some element abundances, extending the model outside the outer radius to let the shock go further. In this work, we do not perform stellar calculations ourselves and use the progenitors that were provided by Sukhbold and Woosley (2014).

The next step is to explode the initial model with a 1D hydrodynamic code. The star does not explode by itself in 1D, so the explosion has to be induced artificially and there are several well-known ways to do it, so-called explosion mechanisms: thermal bomb, piston, and neutrino driven explosions. There are a lot of works based on only one explosion mechanism, and it is extremely important to understand the limitations of the mechanisms and to see which results and conclusions could be a feature of the mechanism used.

The last step is explosive nucleosynthesis, which is calculated by post-processing with detailed nuclear reaction networks. It means taking the density and temperature evolution through the explosion from hydrodynamical simulations and applying the network calculation to it. Detailed nucleosynthesis calculations are essential in discussing the element production in CCSN.

In the next chapter, I want to describe the theory of CCSN and the methodology of the present work. The main part of this thesis will be discussing different parametrizations of the mechanisms: collapse phase of the explosion (Chapter 3), overview of the parameters of thermal bomb explosions (Chapter 4) and a comparison between different 1D explosion mechanisms (Chapter 5). All the results will be calibrated to a certain explosion energy and discussed in the context of nickel production and the dynamics of the explosion since the final nickel mass and the explosion energy are important links to the observations. Our goal is to provide a parametric study on thermal bomb calculations and to compare explosion mechanisms with each other.

# Chapter 2

# Theory of CCSN Explosions and Methodology

## 2.1 Physics and Current Picture

Details of the underlying mechanism of massive stars explosions can be found in the following reviews: Bethe (1990); Janka et al. (2007); Foglizzo et al. (2015). In the following, I want to give a summary of the physics and nucleosynthesis in CCSN.

In the current physical picture of stellar collapse and explosion, it is believed that normal CCSN could be explained by a delayed neutrino heating model. In this model, a supernova explosion is driven by the neutrinos emitted from a proto-neutron star. The iron core, which is formed in the center of the massive star and is nurtured by the silicon shell burning around it (see Figure 1.2), increases in mass until it reaches the Chandrasekhar mass limit ($\sim 1.5 M_{\odot}$). At this point the core becomes gravitationally unstable, and electron degeneracy pressure can no longer stabilize the core against gravity, so it collapses, and the matter starts to fall inward. During the collapse, the gravitational energy is converted into internal energy, and it is mainly radiated away by neutrinos. In the early stage of the collapse, the electron fraction, which is defined as the ratio of electrons to baryons (i.e., neutrons and protons) in the matter, decreases by electron capture on iron peak isotopes. It shifts the distribution of nuclei in the core to more neutron rich matter. Moreover, many of the isotopes also experience $\beta$-decays. Electron capture, $\beta$-decay, and photodisintegration of iron group isotopes to alpha particles reduces the electron density of the core which leads to the acceleration of the collapse until the collapse is stopped. It stops due to the stiffening of the equation of state because the interaction of the nucleons has a repulsive and short range nature. Next, at around nuclear densities, a collapsing iron core bounces, and a proto-neutron star is formed at the center. Bounce leads to a formation of a prompt shock wave, which is first stalled above a proto-neutron star by interactions with infalling matter, and is subsequently revived through heating via the outstreaming neutrinos. It results in the propagation of a shock wave through the stellar envelope which destroys the rest of the star leading to a visible explosion. First stalled and then revived, the shock wave

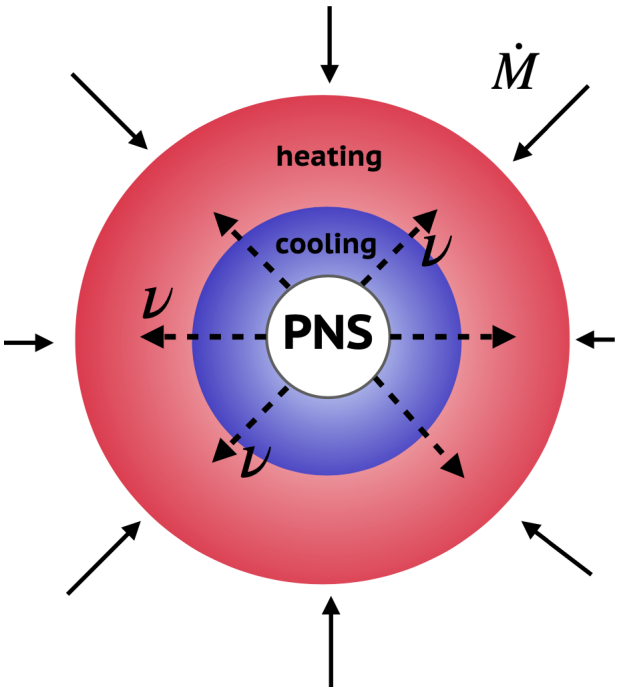


Figure 2.1: The simplified picture of the delayed neutrino heating mechanism. Proto-neutron star (PNS) is formed in the center and radiating neutrinos, while the matter $\dot{M}$ is falling inward.

leads to this model being called delayed, and neutrinos play a big role in the explosion. They heat the material and cause the shock wave to be revived after stagnation.

Neutrinos are responsible for heating up the matter, since they produce energy by the charged-current neutrino capture reactions on free nucleons:

$$\nu_e + n \rightarrow p + e^-, \tag{2.1}$$
$$\bar{\nu}_e + p \rightarrow n + e^+, \tag{2.2}$$

while they are also responsible for the cooling with the corresponding inverse reactions:

$$p + e^- \rightarrow \nu_e + n, \tag{2.3}$$
$$n + e^+ \rightarrow \bar{\nu}_e + p. \tag{2.4}$$

The summarized (and simplified) picture can be seen in Figure 2.1 presenting the iron core in the process of CCSN. A proto-neutron star (PNS) is formed in the center, and it is radiating neutrinos while the shock is developing and the matter, $\dot{M}$, is falling inward.

The composition of the ejecta is of main interest in the studies of nucleosynthesis in CCSN. According to this model, the elements in the explosion are produced in two components: in shock heated material (Thielemann et al., 1996; Umeda and Nomoto, 2002), where the shock wave interacts with the infalling matter, and in the neutrino driven wind

Table 2.1: Explosive nucleosynthesis in CCSN.

| Temperature [GK] | $> 5$ | $4 - 5$ | $3.3 - 4$ | $2.1 - 3.3$ |
|---|---|---|---|---|
| Process | Complete Si burning | Incomplete Si burning | Explosive O burning | Explosive Ne/C burning |
| Main products | Ni, Co, Zn | Si, S, Fe, Cr, Mn | Si, S, Ar, Ca | Mg, Si, S |

(Qian and Woosley, 1996; Arcones and Thielemann, 2013), where the matter is heated by outstreaming neutrinos. The explosion itself mostly produces iron group nuclei, however normal CCSNe are also partly responsible for the origin of the elements lighter than Si, though their abundances are mainly determined by the nucleosynthesis during stellar evolution.

### 2.1.1 Shock-heated Material

For the shock-heated component, the most important indicator for nucleosynthesis is the post-shock temperature. The inner region can be divided into four regions by their temperatures as one can see in Table 2.1 where a simplified representation of the explosive nucleosynthesis due to the passage of the shock wave through the different layers of the star is listed. Higher temperatures typically correspond to lower radii, or locations deeper in the star.

Once the shock wave has been launched from the core, it first encounters the Si shell inducing the complete silicon burning in the innermost region ($T > 5$ GK, 1 GK$= 10^9$ K). The main product here is $^{56}$Ni, but also the other isotopes of Co, Ni, and Zn are mostly produced here, near the proto-neutron star. Once the temperatures are high enough, the matter reaches the nuclear statistical equilibrium (NSE), when the rates of all forward and reverse reactions are in a global equilibrium. In other words, there is a global balance between the production and disintegration of the nuclei. The composition in NSE is determined by temperature, density, and the electron fraction of the matter $Y_e$ (the ratio of electrons to baryons).

The next region is between 4 and 5 GK, and it is called the incomplete silicon burning. It produces lighter Fe-peak elements and some intermediate elements, such as Si and S, and Fe, originally produced as $^{56}$Ni, as well as Cr and Mn. The temperatures $T \approx 3.3 - 4$ GK correspond to the O/Ne layer in the pre-supernova stage, and here the explosive oxygen burning occurs. O is partly burning and Mg is partly decomposed and captured with the main products here being the isotopes of Si, S, Ar, and Ca. The final region interesting for the nucleosynthesis ($T \approx 2.1 - 3.3$ GK) suffers explosive Ne/C burning, where carbon and neon are burning into the isotopes of Mg, Si and S. In the outer regions the time for which the post shock temperature ($T < 2.1$ GK) is maintained is much too short to induce a nucleosynthesis. Therefore, the layers above Ne/C are almost untouched.

Although it presents the general picture of the explosive nucleosynthesis, the exact abundances also depend on the details of the pre-supernova stellar structure. Moreover, the initial electron fraction profile $Y_e(r)$ strongly affects the result of the nucleosynthesis,

which occurs in NSE.

Explosive nucleosynthesis barely affects the final yield for major elements up to Al. The elements between Si and Ca are produced during both the stellar evolution and the SN explosion. Iron peak elements are also produced during the stellar evolution. However, they are produced mainly in the Fe core and are not ejected by the explosion. Iron peak elements in the SN ejecta are newly produced by complete and incomplete Si burnings.

### 2.1.2 Neutrino-heated Material

After CCSN has occurred, the PNS is formed at the center, and it has rather high temperatures and densities. Under these conditions, neutrinos are produced in abundance, and they carry away the gravitational binding energy of the PNS.

Then the neutrinos are also being reabsorbed by the matter close to the surface of the PNS, and they deposit enough energy for the matter to be able to escape the gravitational field of PNS. This leads to a flow of matter leaving the PNS, and it is called the neutrino-driven wind. The mass loss of the PNS is stopped after the PNS becomes transparent to neutrinos ($\sim$ 10 s). Very close to the surface of the PNS, the temperature and density are so high that the matter is mainly made of free neutrons and protons. However, the escaping of the neutrinos is followed by the cooling down of the PNS, and this allows for $\alpha$-particles, and later on heavier nuclei, to be produced.

The neutrino-driven wind is a rather interesting aspect of nucleosynthesis in CCSN, and it is a candidate site for the r-process nucleosynthesis. The conditions in the wind can lead to the production of heavy nuclei, beyond iron, on the proton- or neutron-rich side of the nuclear chart, depending on the electron fraction. However, the results strongly depend on different physical conditions, and, in particular, the structure of the progenitor. The abundances are defined, for example, by the gravitational field of the PNS, and they depend also on the properties of the emitted neutrinos, their luminosities and spectra, and the electron fraction. This component will not be discussed in much detail in the present work.

## 2.2 1D Modeling

1D modeling is very widely used in the literature (see Section 2.4). There are several artificial ways to induce an explosion in spherical symmetry. Three of them are investigated in this work:

- thermal bomb
- piston
- neutrino-driven

Here I would like to describe the main ideas of these artificial explosion mechanisms and how their comparison works, leaving all the details of their parametrization to the next

chapters (Chapter 3 and Chapter 4 for the thermal bomb, and Chapter 5 for the piston and neutrino driven explosions).

Let me start with the so-called thermal bomb approach, where the explosion is triggered by a continuous energy input at the inner boundary (IB). The inner boundary represents the proto-neutron star (PNS) surface, though the PNS core is removed for the simulations. The location of the inner boundary is in fact the first parameter of this mechanism. Other free parameters of the model are the injected or deposited energy, $E_{\rm inj}$, the volume of this deposition (mass layer), $\Delta M$, and the time during which the energy is deposited, $t_{\rm inj}$. These parameters combined define the energy input rate $E_{\rm inj}/(\Delta M t_{\rm inj})$. There could be different ways to deposit the energy, but most commonly the input energy is assumed to increase linearly. Figure 2.2 shows the radius evolution of Lagrangian mass shells with time. It is presented here as an example, all the terminology in the context of this explosion mechanism will be discussed in details in Chapter 3. The important aspect here is that, as could be seen on the plot, the deposited energy pushes the mass shells outward leading to an explosion. The thermal bomb mechanism is rather flexible; it is easy to use, and the variation of the parameters can control the dynamics of the explosion.

The next mechanism is the piston driven explosion, where the shock wave is produced by artificially moving the inner boundary with a highly supersonic velocity. The inner boundary indicates the initial piston location, and it is also a free parameter in this approach. Piston mass, $M_{\rm pist}$, is the mass enclosed by the piston, so basically the location of the inner boundary. First, the piston is moved inward for a certain time, $t_{\rm coll}$, mimicking the collapse phase of the explosion. Then it is moved outward with a given velocity $u_0$, which is a free parameter controlling the explosion. The piston velocity as a function of time is given by:

$$\frac{dr}{dt} = \begin{cases} v_0 - a_0 t & t < t_{\rm coll}, \\ \sqrt{u_0^2 + 2fGM_{\rm pist}(1/r - 1/r_{\rm min})} & t \geq t_{\rm coll}, r < r_{\rm max}, \\ 0 & t \geq t_{\rm coll}, r \geq r_{\rm max}, \end{cases} \tag{2.5}$$

where $v_0$ is the initial velocity of the shell where the piston is located, $a_0 = 2(r_0 - r_{\rm min} + t_{\rm coll} v_0)/t_{\rm coll}^2$ is a constant acceleration calculated in order to reach the minimum radius, $r_{\rm min}$, in time, $t_{\rm coll}$, with $r_0$ being the initial piston radius, and $f = -u_0^2/[2GM_{\rm pist}(1/r_{\rm max} - 1/r_{\rm min})]$ is chosen in order to ensure that the piston coasts to an asymptotic radius of $r_{\rm max}$. The piston is then held at the maximum radius.

Equation (2.5) defines the movement of the inner boundary, since the piston is located at a constant Lagrangian mass coordinate. The collapse phase is basically controlled by the parameters $t_{\rm coll}$ and $r_{\rm min}$ while the explosion phase in controlled by the parameters $u_0$ and $r_{\rm max}$. The radius evolution of Lagrangian mass shells as a function of time for this approach is shown in Figure 2.3 (note, the axes are not the same as for Figure 2.2). For this example the collapse phase is followed for $t_{\rm coll} = 0.45$ s, which is indicated by a vertical line, before the minimum radius $r_{\rm min} = 5.0 \cdot 10^7$ cm is reached by the inner boundary. The explosion velocity $u_0$ is given to the piston at $t_{\rm coll}$ leading to an expansion of the mass shells.

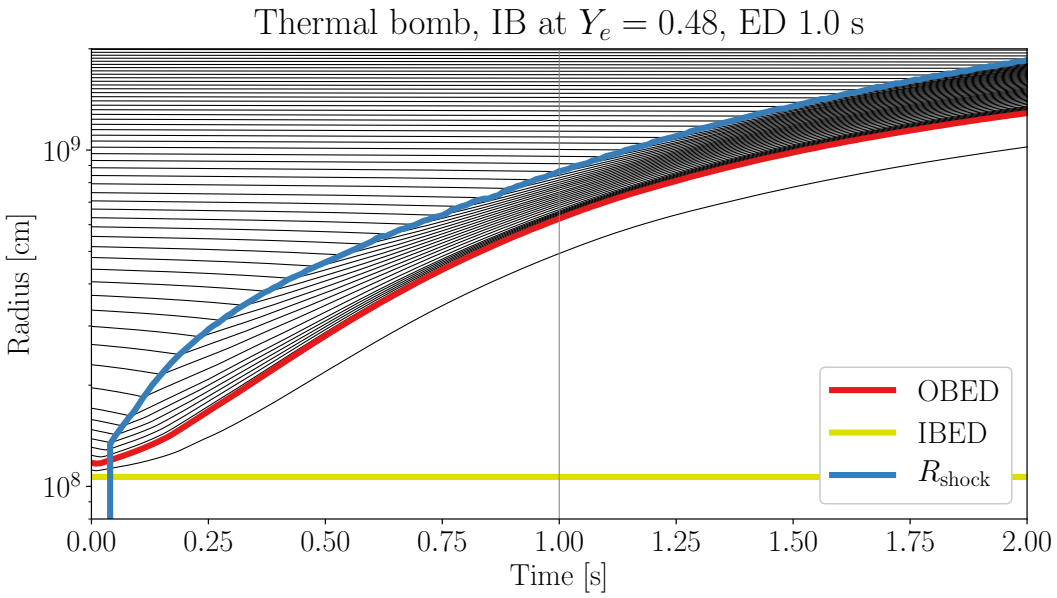


Figure 2.2: Radius evolution of Lagrangian mass shells with time for the $21M_\odot$ progenitor, thermal bomb explosion. The yellow line is the inner boundary of the energy deposition (IBED), which is the same as the inner boundary of the calculation and placed here at $Y_e = 0.48$, the red line is the outer boundary of the energy deposition (OBED), which corresponds here to $0.05M_\odot$ mass layer, and the blue line is the shock radius, $R_{\rm shock}$. The vertical line indicates the energy deposition (ED) time, which is 1 s in this case. The thin black solid lines are the mass shells, spaced in steps of $0.025M_\odot$.

You can see the difference in the dynamics with Figure 2.2. In this case the explosion is happening instantly at the bounce.

Finally, let us discuss the neutrino driven explosions which can be described in three phases from the onset of the core collapse until the neutrino driven wind becomes dynamically unimportant. I shortly summarize here the main aspects of this method discussed in details in Ertl et al. (2016), which will be used here unchanged, in order to compare with thermal bomb and piston explosions.

During the collapse phase, the innermost core is not excised, and the simulations have to go until supernuclear densities ($\sim 2.5 \cdot 10^{14}\,\mathrm{g/cm^3}$) are reached in the center in order to catch the formation of the shock. For a smooth collapse, the high density equation of state is used which takes into account heavy neutron rich nuclei. The core collapse is followed by a simple and efficient numerical scheme for the deleptonization. It is described in detail in Liebendörfer (2005) and implies an exchange of the numerically expensive solution of a transport problem with a local problem which approximates the deleptonization of the iron core. This leads to the formation of a shock at core bounce right after the collapse phase. At this point, after core bounce, it is important to be able to follow neutrino production, and the neutrino transport equation is solved by the so-called gray transport solver, which is described in Scheck et al. (2006). Basically, the word “gray” implies that the neutrino

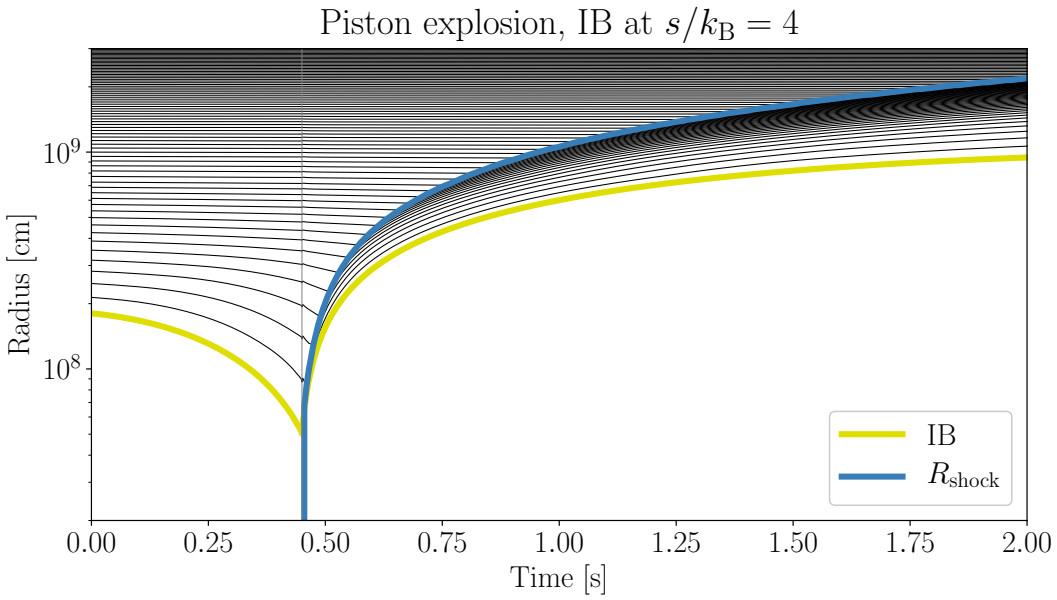


Figure 2.3: Radius evolution of Lagrangian mass shells with time for the $21M_\odot$ progenitor, piston driven explosion. The blue line corresponds to the shock radius, $R_{shock}$, the yellow line shows the movement of the mass cut according to equation (2.5), while the vertical line corresponds to bounce, which is happening at $t_{coll} = 0.45$ s. The thin black solid lines are the mass shells, spaced in steps of $0.025M_\odot$.

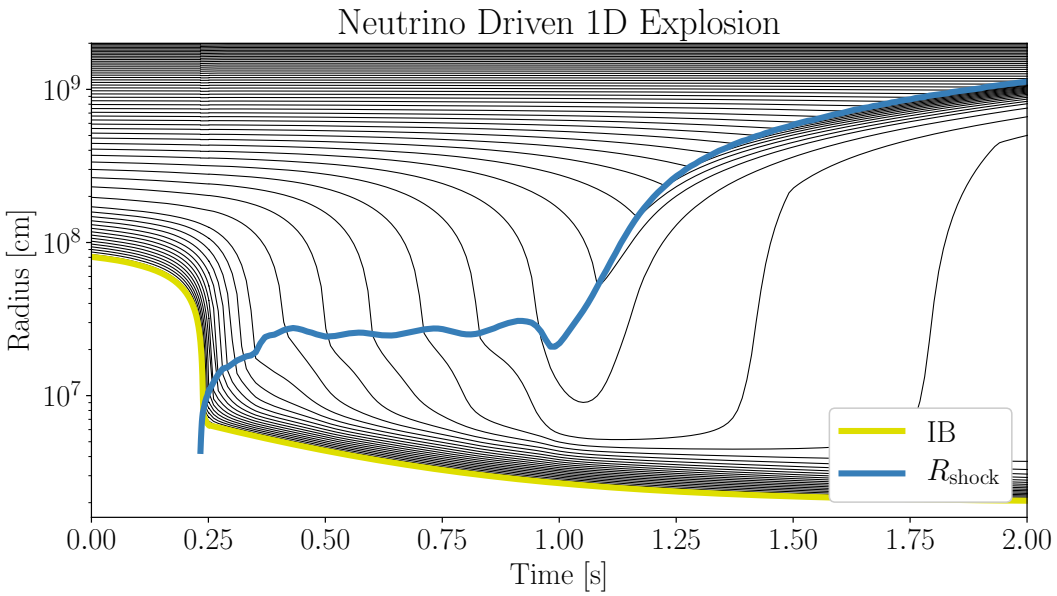


Figure 2.4: Radius evolution of Lagrangian mass shells with time for the $21M_\odot$ progenitor, neutrino driven explosion. The result is taken from Ertl et al. (2016). The blue line corresponds to the shock radius, $R_{shock}$, the yellow line is the inner boundary, the thin black solid lines are the mass shells, spaced in steps of $0.025M_\odot$.

energy is not evolved in time but only the mean energy of the neutrinos is (Ertl, 2016).

For the final phase, which is continued for $\sim 10\,\mathrm{s}$, an analytic one-zone core-cooling model is used. A core is radiating neutrinos, and their luminosity, $L_{\nu,\mathrm{c}}(t)$, is parametrized by this approach. The total core-neutrino luminosity is determined by the core mass, $M_\mathrm{c}$, the core radius, $R_\mathrm{c}(t)$, the rate of contraction of this radius, $\dot{R}_\mathrm{c}(t)$, the mass of the PNS accretion mantle around the core, $m_\mathrm{acc}$, (taken to be the mass between the inner grid boundary and a lower density of $10^{10}$ g/cm$^3$) and the mass accretion rate of the PNS, $\dot{m}_\mathrm{acc}$. The expression for the core luminosity can thus be written as

$$L_{\nu,\mathrm{c}}(t) = \frac{1}{3(\Gamma-1)}\left[(3\Gamma-4)(E_\mathrm{g}+S)\frac{\dot{R}_\mathrm{c}}{R_\mathrm{c}} + S\frac{\dot{m}_\mathrm{acc}}{m_\mathrm{acc}}\right], \tag{2.6}$$

with the factors

$$E_\mathrm{g} + S = -\frac{2}{5}\frac{GM_\mathrm{c}}{R_\mathrm{c}}\left(M_\mathrm{c} + \frac{5}{2}\zeta m_\mathrm{acc}\right), \tag{2.7}$$

$$S = -\zeta\frac{GM_\mathrm{c}m_\mathrm{acc}}{R_\mathrm{c}}, \tag{2.8}$$

and with the adiabatic index, $\Gamma$, and coefficient $\zeta$ being free parameters of the approach.

The central core of the PNS resulting from the collapse is excised from the computational volume and replaced by a contracting inner grid boundary shortly after the expanding shock has converted to a stalled accretion shock. The core radius as a function of time is defined by

$$R_\mathrm{c}(t) = R_\mathrm{c,f} + \frac{R_\mathrm{c,i} - R_\mathrm{c,f}}{(1+t)^n}, \tag{2.9}$$

where $R_\mathrm{c,i}$ is the initial PNS core radius, which is set equal to the initial radius of the inner boundary, and $R_\mathrm{c,f}$ is the final PNS core radius, which, along with the exponent, $n$, is also a free parameter of this approach.

As could be seen from radius evolution of Lagrangian mass shells plots, all three mechanisms have rather different dynamics. In order to compare different explosions with each other, no matter whether it would be different mechanisms or different parametrizations of the same mechanism, it makes sense to fix the explosion energy for the same pre-collapse star since it is an important link to observations. This comparison strategy requires a calibration of the models, which means changing the parameters responsible for the explosion in order to reproduce the desirable energy with a certain accuracy.

### 2.2.1 This Work

In this work, the explosion simulations were performed using the one-dimensional hydrodynamics code Prometheus-HOTB, or in short P-HOTB. It solves the hydrodynamics of a stellar plasma, including evolution equations for the electron fraction and the nuclear species, in a conservative manner on an Eulerian radial grid employing a higher-order Godunov scheme with an exact Riemann solver. The code utilizes a micro-physical model of the equation of state that includes a combination of non-relativistic Boltzmann gases

for nucleons and nuclei, arbitrarily degenerate and arbitrarily relativistic electrons and positrons, and energy and pressure contributions from trapped photons. Although the hydrodynamics is treated in the Newtonian limit, the self-gravity of the stellar matter takes into account general relativistic corrections. Relevant details of the code and its upgrades over time can be found in the papers of Janka and Müller (1996); Kifonidis et al. (2003); Scheck et al. (2006); Arcones et al. (2007); Ugliano et al. (2012); Ertl et al. (2016, 2020).

The first steps of my work included testing of the thermal bomb and piston mechanisms in P-HOTB. Some non-working versions of them were already in the code, and my task was to debug and polish them. Both the thermal bomb and piston methods have several modifications in parameter calibration, position of the mass cut and inclusion of the collapse phase. To use the modifications, I implemented a more convenient way of setting the trajectory into P-HOTB for piston, and successfully reproduced the results of previous works (e.g. Ugliano, 2012; Ertl, 2016). For thermal bomb, aside from a classical option, I also implemented a collapse phase that is working in a same way as for piston. These modifications will be discussed in the next chapters (Chapter 3 and Chapter 4 for thermal bomb and Chapter 5 for piston driven explosions). In order to compare the mechanisms, I calibrate all of them to the same explosion energy, so I also developed calibration pipelines for different mechanisms.

## 2.3 Nuclear Reaction Networks

The change in composition of the matter, or nucleosynthesis, is performed with the help of nuclear network calculations. The abundances of species will depend not only on the nuclear reactions which produce or destroy them, but also on the hydrodynamic effects. The volume of stellar plasma, or any astrophysical environment, can be changed due to expansion and contraction. Nuclear abundance is defined as

$$Y_i = \frac{n_i}{n} = \frac{n_i}{\rho N_A}, \tag{2.10}$$

where $n_i$ is the number density of a nuclear species, $N_A$ is Avogadro's number and $n$ is the total number of nucleons. The mass fraction of a nucleus is related to its abundance through its mass number, $X_i = Y_i A_i$, while baryon number is conserved, $\sum_i Y_i A_i = \sum_i X_i = 1$. Abundances can be calculated based on the evolution of the density, $\rho(t)$, and temperature, $T(t)$, that are taken from hydrodynamic simulations using the following expression (Müller, 1986):

$$\frac{dY_i}{dt} = \sum_j c_i(j)\lambda_j Y_j + \sum_{j,k} c_i(j,k)\frac{\rho}{m_b}\langle\sigma v\rangle_{j,k} Y_j Y_k + \sum_{j,k,l} c_i(j,k,l)\left(\frac{\rho}{m_b}\right)^2 \langle\sigma v\rangle_{j,k,l} Y_j Y_k Y_l. \tag{2.11}$$

The first term on the right hand side describes changes in composition due to $\beta$-decays, electron captures and photodisintegrations with the corresponding rates, $\lambda_j$, the second term refers to two-body reactions, such as fusion reactions, and the third term takes into

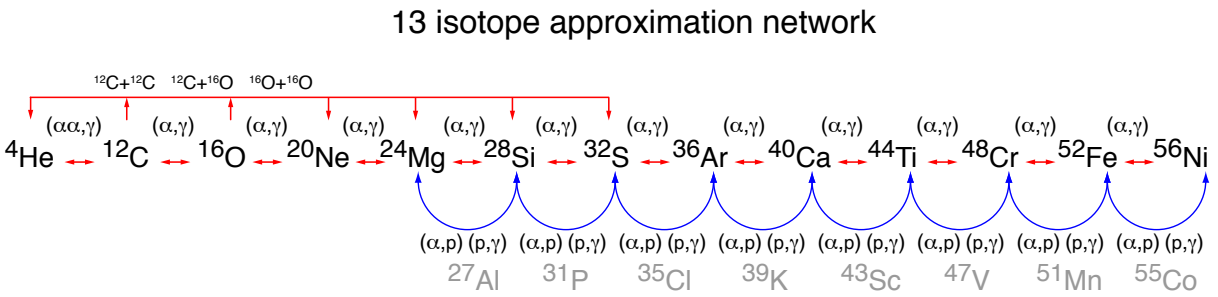


Figure 2.5: The $\alpha$-chain reaction network implemented in P-HOTB simulations. The network is capable of tracking bulk nucleosynthesis and taking into account the nuclear energy generation without making the calculations too computationally expensive to handle.

account three-body reactions, such as triple-alpha reactions. $\langle \sigma v \rangle$ terms are the thermally averaged products of cross-section times relative velocity (Fowler et al., 1975). The coefficients $c_i$ are defined as:

$$c_i(j) = \pm N_i,$$
$$c_i(j,k) = \pm \frac{N_i}{N_j! N_k!},$$
$$c_i(j,k,l) = \pm \frac{N_i}{N_j! N_k! N_l!},$$

where $N_j$, $N_k$ and $N_l$ are absolute numbers indicating how many particles of type $i$, $j$, $k$ and $l$ are involved in the reaction. The sign is defined based on whether the nucleus is produced $(+)$ or destroyed $(-)$. With the initial abundances, temperature and density evolutions, the network calculations can be either calculated in parallel with hydrodynamics or it could be done as a post-processing step afterwards.

A small $\alpha$-network is consistently coupled to the hydrodynamic modelling in P-HOTB. It is capable of tracking the bulk nucleosynthesis and thus account for the contribution to the explosion energy provided by explosive nuclear burning. The network includes the 13 isotopes of the alpha-chain, $^{4}$He, $^{12}$C, $^{16}$O, $^{20}$Ne, $^{24}$Mg, $^{28}$Si, $^{32}$S, $^{36}$Ar, $^{40}$Ca, $^{44}$Ti, $^{48}$Cr, $^{52}$Fe, and $^{56}$Ni, plus a "tracer nucleus" $^{56}$Tr, which is connected to the network with the reaction rates of $^{56}$Ni and is supposed to keep track of the formation of neutron-rich species in matter with considerable neutron excess, i.e., when $Y_e < 0.49$. The network calculations are applied for temperatures between 0.1 GK and 9 GK, whereas, for higher temperatures, nuclear statistical equilibrium (NSE) is assumed.

The reactions included can be seen on Figure 2.5, and the network is described in relevant details in Müller (1986). This network helps to take into account nuclear energy production, which means that the nuclear reactions are fully coupled to the hydrodynamics by a source term:

$$\delta Q_{\mathrm{nuc}} = n_{\mathrm{B}} \Delta \bar{m} c^2 = n_{\mathrm{B}} \sum_i (Y_{i,t_n} - Y_{i,t_n+1}) B_i(Z,A), \tag{2.12}$$

accounting for the consumption or release of internal energy, where $\Delta\bar{m}$ is the mean baryon mass and $B_i(Z, A)$ is the binding energy per nucleus $i$.

In order to perform more detailed nucleosynthesis calculations of our models in a post-processing step, we made use of the modular nuclear reaction network library SkyNet (Lippuner and Roberts, 2017). For this purpose, we extracted the temperature and density evolution of selected mass-shell trajectories from our CCSN explosion simulations with P-HOTB and applied the SkyNet network for each of these shells. The mass shells were selected starting at a location near the mass cut of the proto-neutron star, and the network calculations were constrained to the same regime in temperature as used for the small network in P-HOTB, namely to the interval between 0.1 GK and 9 GK. Adding up the nuclear abundances obtained for all mass shells that end up to be ejected (i.e., that expand outward continuously until the end of the hydrodynamic simulation) provided the integrated yields of chemical elements and isotopes. If mass shells reached a peak temperature above $T_{\mathrm{NSE}} = 9\,\mathrm{GK}$, the network calculations were started with the local NSE composition at the time when the temperature dropped below 9 GK. Otherwise, if mass shells did not reach temperatures as high as 9 GK, the initial composition was taken from the progenitor data. The mass resolution for post-processing the nucleosynthesis in the innermost ejecta was chosen to be $10^{-4}\,M_\odot$, which means that the mass shells were taken with the step $10^{-4}\,M_\odot$ and processed independently.

SkyNet allows one to define any selection of isotopes of interest and to define their relevant reactions. So theoretically we could include as many nuclear species as we wanted in our reaction network. However, generally speaking, each nucleus interacts with every other nucleus present in the matter, and even though many of the reactions can be neglected, it still makes it quite computationally expensive to find the network solution. Therefore, we investigated several options on the isotope lists in our calculations.

We took great care to employ a sufficiently big set of isotopes and to include all of their important reactions. To arrive there we started with three different sets of isotopes, inspired by their use in the literature: a small network with 160 isotopes (Sandoval et al., 2021), a medium-sized network with 204 isotopes (Paxton et al., 2015), and a large network with 822 isotopes (Woosley and Hoffman, 1992). We modified the medium and large networks in a way each network is a subset of the larger networks. On top of that, we added more light isotopes; for the largest network, for example, we included all nuclear species available in SkyNet with $Z \leq 15$ and $N \leq 15$. After these modifications, we ended up with selections of 160, 262, and 878 isotopes (see Figure 2.6). With all three versions of the network, we performed nucleosynthesis calculations for trajectories with the most extreme conditions (in density, $Y_e$, and temperature) picked from the set of our CCSN models. We found that the yields were very well determined for the 50 most abundantly produced isotopes when including 262 species compared to the case with 878 isotopes, and the order of magnitude for the last isotopes was around $\sim 10^{-6}$. Therefore, we continued all further analyses with this medium-sized network, whose selection of nuclei is listed in Table 2.2.

In the present work, we will only discuss the production of $^{56}$Ni based on our network calculations with the 262-isotope setup of SkyNet. We focus on this nickel isotope and aim at exploring the dependence of its production on the parameterization of the thermal-

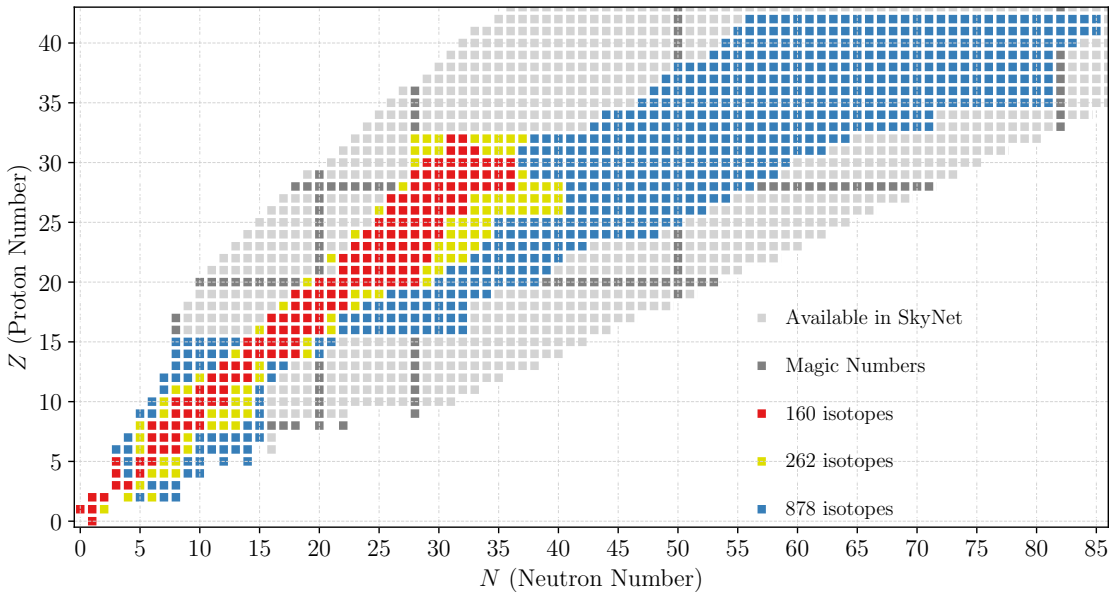


Figure 2.6: Nuclear chart visualizing the three sets of isotopes used in this work for testing the final nucleosynthetic outputs. The test calculations were done under extreme conditions of density, $Y_e$, and entropy, and were carried out until $t = 10\,\mathrm{s}$. Their results showed convergence in the final yields of the 50 most abundantly produced isotopes between the sets with 262 isotopes and 878 isotopes.

Table 2.2: Nuclear species used for the nucleosynthetic post-processing of our CCSN models with SkyNet.

| Nuclei used in the 262-species network | | | | |
|---|---|---|---|---|
| n | $^{1-3}$H | $^{3-4,6,8}$He | $^{6-8}$Li | $^{7,9-12}$Be |
| $^{8,10-13}$B | $^{11-15}$C | $^{12-16}$N | $^{13-21}$O | $^{16-23}$F |
| $^{17-24}$Ne | $^{19-25}$Na | $^{22-27}$Mg | $^{25-28}$Al | $^{27-33}$Si |
| $^{29-34}$P | $^{31-37}$S | $^{33-38}$Cl | $^{35-41}$Ar | $^{37-44}$K |
| $^{39-49}$Ca | $^{43-51}$Sc | $^{43-54}$Ti | $^{46-56}$V | $^{47-58}$Cr |
| $^{50-59}$Mn | $^{51-66}$Fe | $^{53-67}$Co | $^{55-68}$Ni | $^{57-66}$Cu |
| $^{58-66}$Zn | $^{59-67}$Ga | $^{60-69}$Ge | | |

bomb treatment and compare between different explosion mechanisms. This isotope is particularly important because the mass of $^{56}$Ni ejected in the explosion is an important diagnostic quantity for CCSN observations (Arnett et al., 1989; Müller et al., 2017b; Yang et al., 2021; Valerin et al., 2022). Any implementation of a method to artificially trigger explosions in CCSN models should therefore be checked for its ability to provide reasonable predictions of the $^{56}$Ni yield and for the robustness of these predictions concerning changes of the (mostly rather arbitrarily) chosen values of the parameters steering the trigger mechanism. The produced amount of $^{56}$Ni is particularly useful to assess these questions because the isotope is made in the innermost CCSN ejecta. Therefore, it is potentially most immediately and most strongly affected by the artificial method (or by the physical mechanism) that is responsible for initiating the explosion.

## 2.4 Literature Overview

There have been many works on the explosion mechanisms, as well as on the comparison between different mechanisms. Studying nucleosynthesis in 1D CCSNe often comes down to a question of what mechanism was used for the explosion. In this section, I want to summarize what has been done on this subject in the literature.

Thermal bomb was used, for example, in Shigeyama et al. (1988); Hashimoto et al. (1989); Thielemann et al. (1990, 1996); Nakamura et al. (2001); Nomoto et al. (2006); Umeda and Nomoto (2008); Moriya et al. (2010). It is not very computationally expensive, its usage is made very simple, the parameters make the mechanism rather flexible, and it attracts attention. A piston driven mechanism was used by Woosley and collaborators, see Woosley (1988); Woosley and Weaver (1995); Woosley et al. (2002); Woosley and Heger (2007); Zhang et al. (2008). These works are performing the large parameter space calculations, and can be used for galactic chemical evolution simulations, so knowing the limitations of the model would be rather important here. Also, multidimensional (2D, 3D) variants of the method of thermal (or kinetic) bombs exist to trigger highly asymmetric blast waves and jet-induced or jet-associated explosions, see Nagataki et al. (1997); MacFadyen and Woosley (1999); Khokhlov et al. (1999); Aloy et al. (2000); Nagataki et al. (2003); Maeda and Nomoto (2003); Nagataki et al. (2006) for a few exemplary applications from a rich spectrum of publications.

All of these methods of artificially exploding massive stars depend on numerous free parameters, for example the location of the initial mass cut, the width of the energy-deposition region and the timescale of energy deposition for the thermal bomb, the duration, and depth of the collapse-like contraction, and the initial expansion velocity and coasting radius for the piston method, the initial velocity of the kinetic bomb, or the 2D/3D geometry of the energy input. These parameters are chosen suitably to produce defined values for the explosion energy and the expelled $^{56}$Ni mass. Such degrees of freedom have an influence on the nucleosynthetic yields through the initial strength of the shock and the volume and extent of the heating achieved by the thermal energy injection. This in turn determines the ejecta mass where sufficiently high peak temperatures for nuclear reactions are reached.

Moreover, the traditional explosion recipes do not enable one to track the conditions in the innermost ejecta whose neutron-to-proton ratio gets reset by the exposure to the intense neutrino fluxes from the nascent neutron star or from an accretion torus around a newborn black hole (Bruenn et al., 2016; Müller et al., 2017a; Siegel et al., 2019; Bollig et al., 2021).

For these reasons more modern CCSN explosion treatments by means of "neutrino engines" have been introduced that attempt to capture essential effects of the neutrino-driven mechanism but which replace the highly complex and computationally intense energy and direction dependent neutrino transport used in full-fledged neutrino-hydrodynamical CCSN models by simpler treatments. This line of research has been pursued in 2D and 3D simulations either neglecting neutrino transport and replacing it by a so-called light-bulb approximation with chosen (time-dependent) neutrino luminosities and spectra (Janka and Müller, 1996; Kifonidis et al., 2000; Shimizu et al., 2001; Kifonidis et al., 2003, 2006; Yamamoto et al., 2013) or by using an approximate, gray description of the neutrino transport with a boundary condition for the neutrino emission leaving the optically thick, high-density proto-neutron star core (Scheck et al., 2006; Wongwathanarat et al., 2010, 2013, 2015, 2017).

Neutrino-engine treatments are also applied in 1D hydrodynamic CCSN simulations with neutrino transport schemes of different levels of refinement for determining the supernova and compact remnant properties as well as the associated nucleosynthetic outputs for large sets of stellar progenitor models. In these studies neutrino-driven explosions are obtained by parametrically increasing the neutrino-energy deposition behind the stalled bounce shock (O'Connor and Ott, 2011) by describing the neutrino emission of the newly formed neutron star via a model with parameters that are calibrated to reproduce basic properties of the well-observed CCSNe of SN 1987A and SN 1054 (Crab) (P-HOTB; Ugliano et al., 2012; Ertl et al., 2016; Sukhbold et al., 2016; Ertl et al., 2020), by parametrizing additional energy transfer to the CCSN shock via muon and tau neutrinos (also using observational constraints) (PUSH; Perego et al., 2015; Ebinger et al., 2019; Curtis et al., 2019; Ebinger et al., 2020), and by also including the effects of convection and turbulence through a modified mixing-length theory approach with free parameters adjusted to fit the results of 3D simulations (STIR; Couch et al., 2020). Alternatively to these novel simulation approaches, semi-analytic descriptions have been applied either by using spherical quasi-static evolutionary sequences to determine the explosion threshold and energy input to the explosion via a neutrino-driven wind (Pejcha and Thompson, 2015) or by trying to mimic the elements of multidimensional processes that play a role in initiating and powering CCSNe via the neutrino-heating mechanism (Müller et al., 2016; Schneider et al., 2021; Aguilera-Dena et al., 2022).

Despite these more advanced modelling efforts, which generally reflect more of the physics of the CCSN explosion mechanism than thermal-bomb or piston models, the latter are still widely used. In fact, thermal bombs have experienced an increase in popularity in 1D applications recently, because they are applied in the open-source codes MESA (Paxton et al., 2015) and SNEC (Morozova et al., 2015). They have the advantage of simplicity and great flexibility in their usage, allowing one to control the dynamics of the explosion by choosing the value, timescale, mass layer or volume of the energy deposition, and the

evolution of the inner boundary, i.e., if and how the collapse of the stellar core is taken into account.

The sensitivities of the traditional thermal or kinetic bombs and piston mechanisms and of the associated nucleosynthesis to the involved parameterizations and the corresponding limitations of these methods have been investigated in previous works, though never comprehensively (Aufderheide et al., 1991; Young and Fryer, 2007). In a seminal study Aufderheide et al. (1991) discussed the parameters employed in the numerical recipes to artificially launch the explosion of a $20\,M_\odot$ progenitor in 1D. They initiated explosions at different locations of enclosed mass and compared the ejecta conditions (especially the peak temperatures reached behind the outgoing shocks) as well as the explosively created nuclear yields. In particular, they considered thermal bomb and piston calculations for two variations, namely when the inner core was allowed to collapse prior to shock initiation or not. We will call such cases "collapsed" (C) versus "uncollapsed" (U) models. They concluded that the former are a better representation of the CCSN physics, which is governed by the iron-core collapse to a neutron star. However, in their study the C-cases also showed more differences between piston and bomb results. Their main concerns were the uncertainties in the choice of the mass-cut location, the assumed duration of the initial collapse phase, and the differences in the peak temperature because of too much kinetic energy being connected to the piston and too much thermal energy to the bomb mechanism. Moreover, they expressed concerns that the instantaneous energy deposition assumed in their simulations might not be appropriate if the CCSN mechanism is delayed and the shock receives energy input by neutrino heating for several seconds (as indeed seen in state-of-the-art self-consistent CCSN simulations, e.g., Bollig et al. (2021)).

In a subsequent study, Young and Fryer (2007) arrived at similar conclusions and found not only a strong sensitivity of the elemental and isotopic yields of silicon and heavier elements to the assumed explosion energy but also considerable differences in the abundances of these nuclei between piston-driven and thermal-bomb type explosions even for the same explosion energy. In particular, they considered a $23\,M_\odot$ star, whose collapse, bounce-shock formation, and shock stagnation were followed by a 1D neutrino-hydrodynamics simulation. Their work was focused on triggering explosions of different energies by thermal energy injection over time intervals of 20 ms, 200 ms, and 700 ms, starting at 130 ms after bounce (corresponding to 380 ms after the start of the collapse simulation). This leads to explosions at 150 ms, 330 ms, and 830 ms after bounce, respectively. The authors reported a considerable increase of intermediate-mass and Fe-group yields with the longer delay times of the explosion (i.e., longer duration of the energy deposition). They underlined, in particular, significantly more (orders of magnitude!) $^{56}$Ni and several times more $^{44}$Ti production for models with $1.5 \times 10^{51}$ erg explosion energy and 200 ms and 700 ms delay time compared to a case with the same explosion energy, but a short energy injection time of only 20 ms.

Recently, Sawada and Maeda (2019) (in the following SM19) published a study where they came to exactly the opposite conclusion based on 1D hydrodynamic CCSN models. Using a thermal-bomb prescription to trigger the explosions of 15, 20, and $25\,M_\odot$ progenitors, they found that the produced amount of $^{56}$Ni *decreases* with longer timescales of the

energy deposition. Observational constraints for nucleosynthesis products of CCSNe could be fulfilled only by rapid explosions when the final blast-wave energy was reached within $\lesssim 250\,\mathrm{ms}$, and best compatibility was obtained for nearly instantaneous explosions where the energy was transferred within $\lesssim 50\,\mathrm{ms}$. They interpreted their results as a serious challenge for the neutrino-heating mechanism, which delivers the explosion energy in progenitors as massive as those considered by SM19 only on timescales that are significantly longer than 1 s (Bruenn et al., 2016; Müller et al., 2017a; Bollig et al., 2021; Burrows and Vartanyan, 2021).

However, the opposite trends reported by Young and Fryer (2007) and SM19 for the dependence of the $^{56}$Ni yields on the energy-deposition timescale do not need to contradict each other. In this context, it is important to remember that the former study considered collapsed (C) models, whereas SM19 did not collapse their stars (using U models) before switching on the thermal energy deposition. This is likely to have important consequences for the hydrodynamic response of the stellar gas when the energy input happens on different timescales. With the expansion of the heated gas setting in, which is easier in an uncollapsed star, expansion cooling takes place. Therefore, slow energy input will not be able to achieve sufficiently high temperatures in sufficiently large amounts of ejecta to enable any abundant production of $^{56}$Ni.

In our work, we aim at investigating this question quantitatively by means of 1D hydrodynamical simulations within the framework of the thermal-bomb method. Two different aspects serve as motivation. First, SM19 and also Suwa et al. (2019) claimed that long energy transfer timescales or slow growth rates of the blast-wave energy ("slow explosions") suppress the $^{56}$Ni production. The authors interpreted this proposition as a problem for current self-consistent neutrino-driven explosion models and the neutrino-driven mechanism itself. Second, our study is supposed to assist the design of suitable thermal-bomb treatments that can serve as easy-to-implement methods to conduct systematic CCSN simulations in 1D for large progenitor sets without the need of a detailed treatment of neutrinos. Naturally, such approaches can never capture all aspects of "realistic" multidimensional CCSN models, in particular not with regard to the innermost, neutrino-processed ejecta. Nevertheless, such simplified explosion treatments can still be useful to answer many observationally relevant questions, in particular since the explosive nucleosynthesis past the outer edge of the silicon shell is mostly determined by the explosion energy and the progenitor structure, but little sensitive to the initiation method of the explosion (Aufderheide et al., 1991). Similarly, the explosive nucleosynthesis in these layers is also unlikely to depend strongly on the neutrino physics and the multidimensional hydrodynamic processes that play a crucial role in the CCSN mechanism and determine the observable asymmetries of the explosions.

In Chapter 3 we thus investigate the influence of the energy-deposition timescale for thermal bombs in collapsed as well as uncollapsed models. But, instead of conducting a complete survey of all free parameters needed to steer the thermal bombs, we will stick to simple and well-tested prescriptions already applied in previous publications. For a diagnostic property we will focus on the produced mass of $^{56}$Ni before any effects of fallback could modify the ejecta because fallback will also depend on the radially outward mixing of

metals and thus on multidimensional effects that can be accounted for in 1D models only with additional assumptions for parametric treatments. The amount of $^{56}$Ni produced by the CCSN "engine" is not only a crucial characteristic of the early dynamics of the explosion, but also a primary observable that governs the light curve and the electromagnetic display of CCSNe from weeks to many years (Arnett et al., 1989; Iwamoto et al., 1994). In Chapter 4 we explore a wider range of thermal-bomb parameterizations and essentially give some recommendations for thermal bomb users. All the indicators for the thermal bomb models used in this work (Chapters 3 and 4) are listed in the Appendix B. In Chapter 5 we check the thermal bomb explosions against piston-triggered and neutrino-driven CCSN explosion models to figure out how the explosion mechanism would affect the final nickel production and nucleosynthesis in 1D CCSN simulations.

# Chapter 3

# Comparison of Thermal Bomb Explosions with and without Collapse

## 3.1 Introduction

In this chapter, I will first describe the progenitor models that are used throughout this work. Then I will mention the setups of the explosions for this chapter, where we only use thermal bomb explosions and look at how the dynamics can affect the final outcome of the explosion. Special attention is drawn to the importance of the collapse phase of the explosion and how it can affect the final nickel production. We compare our thermal bomb models to the reference models from Sawada and Maeda (2019) (SM19), trying to first reproduce the behavior of their models and then to demonstrate what will happen with a changed initial setup. The content of this chapter, as well as some parts of the previous ones, is contained in the publication, which is submitted (Imasheva et al., 2022). All the models and the data analysis were done by me, as well as the development of the program, and parts of the paper were written by me together with the coauthors of the paper.

## 3.2 Inputs and Setups

In this section I describe two aspects of our calculations: the progenitors used as input models and the corresponding explosion simulations including the values of all the parameters and the modifications of the explosion mechanism. Our progenitors were taken from the work of Sukhbold and Woosley (2014), and the explosion modeling was performed using the hydrodynamic code Prometheus-HOTB (Janka and Müller, 1996; Kifonidis et al., 2003; Scheck et al., 2006; Arcones et al., 2007; Ugliano et al., 2012; Ertl et al., 2016), but without making use of the neutrino-transport module associated with this code. The detailed explosive nucleosynthesis was calculated with the SkyNet open-source nuclear network code (Lippuner and Roberts, 2017), as described in Section 2.3.

### 3.2.1 Presupernova Models

The progenitor models for this work were computed with the 1D hydrodynamics code KEPLER (Weaver et al., 1978) and are a subset of the large model set published by Sukhbold and Woosley (2014). They represent non-rotating stars with solar metallicity which were evolved from the main sequence until the onset of the iron-core collapse. The physics of this set of progenitors was discussed in detail in the literature (Woosley et al., 2002; Woosley and Heger, 2007).

In order to investigate basic features of the nickel production using different setups for the thermal bomb triggering the CCSN explosion, we selected four progenitors with zero-age-main-sequence (ZAMS) masses of $M_{\mathrm{ZAMS}} = 12.3$, 19.7, 21.0, and $26.6\,M_{\odot}$. Their characteristic properties are listed in Table 3.1, where $M_{\mathrm{pre}}$ is the total pre-collapse mass, $M_{\mathrm{He}}$ is the helium-core mass defined by the mass coordinate where $X(\mathrm{H}) \leq 0.2$, $M_{\mathrm{CO}}$ is the mass of the carbon-oxygen core associated with the location where $X(\mathrm{He}) \leq 0.2$, $M_{s=4}$ is the mass enclosed by the radius where the value of the dimensionless entropy per nucleon is $s/k_{\mathrm{B}} = 4$ (where $k_{\mathrm{B}}$ is the Boltzmann constant), and $M_{Y_e=0.48}$ is the enclosed mass where the electron fraction is $Y_e = 0.48$.

This selection of the progenitors is motivated by the aim to cover approximately the same range of progenitor masses as considered by SM19. For the lighter progenitors, we investigated two models with $M_{\mathrm{ZAMS}} = 12.3\,M_{\odot}$ and $19.7\,M_{\odot}$, representing two extreme cases with respect to their density declines at mass coordinates $m \gtrsim 1.5\,M_{\odot}$ and differing from each other by the shape of their corresponding density profiles (see Figure 3.1). Our simulations are intended to explore the uncertainties in the thermal-bomb modeling, and these progenitor models exhibit a different behavior in the explosive nickel production based on their structure and our calculations, as will be discussed in Section 3.3.

The upper two panels and the lower left one in Figure 3.2 visualize the progenitor structures in more detail by showing density, electron fraction $Y_e$, and dimensionless entropy per nucleon as functions of enclosed mass. The crosses indicate the inner and outer edges of the regions where most of the $^{56}$Ni is produced based on the results given in the lower right panel of Figure 3.2. This last panel displays, as an exemplary case, the nickel mass fractions for one of our setups (namely the uncollapsed models with deep inner boundary and an energy deposition timescale of 0.01 s, see below).The main region of $^{56}$Ni production is defined by the requirement that more than 90% of this isotope is produced between the limits marked by two crosses. Nickel and other heavy elements are mainly produced in the close vicinity of the inner grid boundaries of the simulations (for the relevant models marked by vertical pale solid lines in Figure 3.2), i.e., close to the mass region that is assumed to end up in the newly formed neutron star. Therefore, differences in the $^{56}$Ni production will be connected to differences in the progenitor structures between the inner grid boundary and below roughly $2M_{\odot}$.

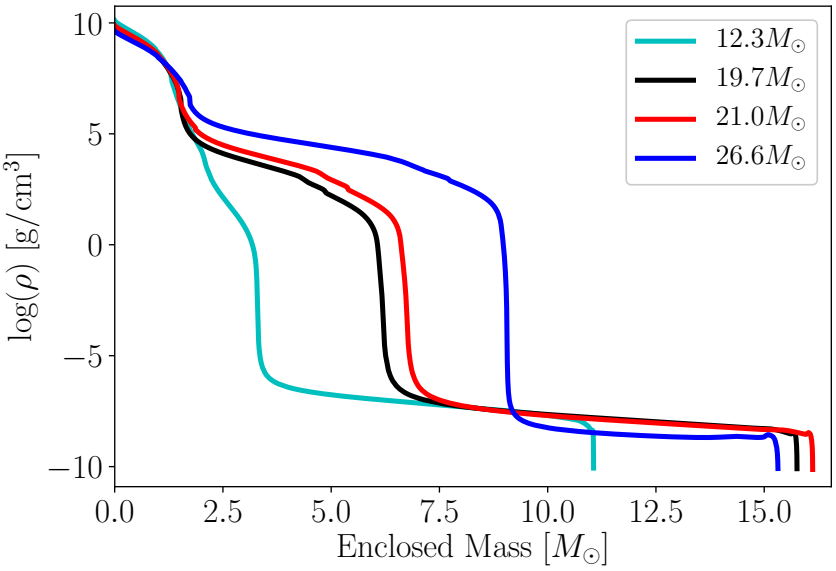


Figure 3.1: Density structure as a function of enclosed mass for the considered progenitors with $M_{\rm ZAMS} = 12.3\,M_\odot$ (cyan line), $19.7\,M_\odot$ (black line), $21.0\,M_\odot$ (red line), and $26.6\,M_\odot$ (blue line). The color convention for the progenitors is kept the same throughout our paper.

Table 3.1: Properties of the progenitors used in this work. $M_{\rm pre}$ is the total pre-collapse mass, $M_{\rm He}$ is the mass of the helium core, $M_{\rm CO}$ the mass of CO core, $M_{s=4}$ is the enclosed mass where the dimensionless entropy $s/k_{\rm B} = 4$, and $M_{Y_e=0.48}$ is the enclosed mass where the electron fraction is equal to 0.48. All the masses are in $M_\odot$.

| $M_{\rm ZAMS}$ | $M_{\rm pre}$ | $M_{\rm He}$ | $M_{\rm CO}$ | $M_{s=4}$ | $M_{Y_e=0.48}$ |
|---|---|---|---|---|---|
| 12.3 | 11.0599 | 3.29162 | 2.22902 | 1.59102 | 1.23017 |
| 19.7 | 15.7490 | 6.09592 | 4.85410 | 1.53298 | 1.25635 |
| 21.0 | 16.1109 | 6.62284 | 5.37384 | 1.48435 | 1.27209 |
| 26.6 | 15.3093 | 8.96794 | 7.69495 | 1.73833 | 1.38264 |

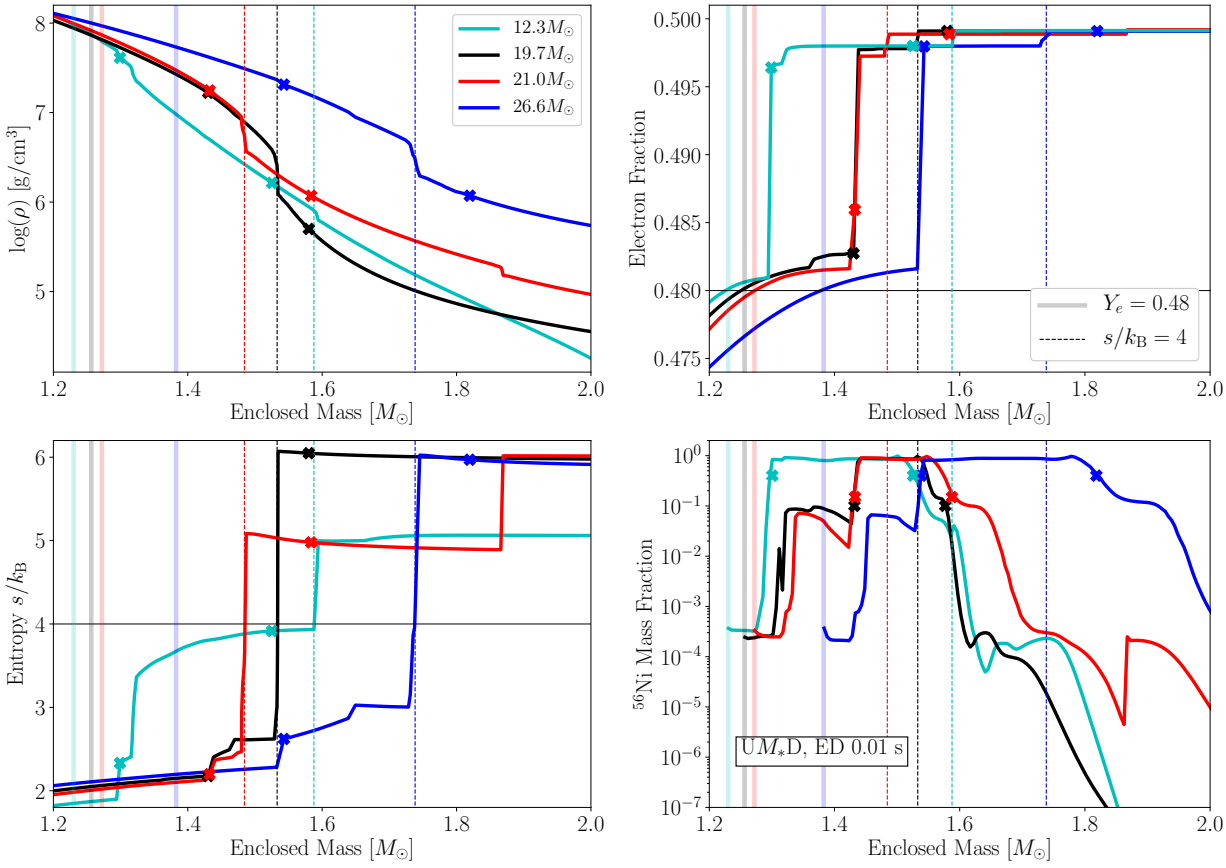


Figure 3.2: Pre-collapse structure of the progenitors used in this work, namely the density (top left), the dimensionless entropy per nucleon $s/k_\mathrm{B}$ (bottom left), and the electron fraction $Y_e$ (top right) versus enclosed mass. Vertical lines indicate the inner grid boundaries chosen in our explosion simulations with the line colors correspond to the colors chosen for the four stellar models; the pale solid lines mark the deeper locations where $Y_e = 0.48$, which is also indicated by the horizontal black line in the $Y_e$ plot, and the short-dashed lines define the points where the dimensionless entropy per nucleon $s/k_\mathrm{B}$ equals 4, which can also be seen by the horizontal black line in the $s/k_\mathrm{B}$ plot. The lower right panel displays the mass fractions of $^{56}$Ni obtained as functions of enclosed mass for our default setup of uncollapsed models with deep inner boundary. The energy-deposition (ED) timescale assumed for the displayed case is $t_\mathrm{inj} = 0.01\,\mathrm{s}$. The crosses on the stellar profiles in all panels mark the locations of the inner and outer edges of the main production region of $^{56}$Ni. Note that due to the similarity of the profiles, the red and black crosses in the two left panels and the lower right panel partly overlap.

### 3.2.2 Thermal Bomb Setups

The progenitor models were exploded by making use of the 1D hydrodynamics code PROMETHEUS-HOTB, or in short P-HOTB, as mentioned in Section 2.2. Relevant details of the code and its upgrades over time can be found in the papers of Janka and Müller (1996); Kifonidis et al. (2003); Scheck et al. (2006); Arcones et al. (2007); Ugliano et al. (2012); Ertl et al. (2016, 2020). The CCSN models discussed in this chapter were computed with a radial mesh of 2000 zones geometrically distributed from the inner grid boundary at radius, $R_{\rm ib}$, to the stellar surface with a resolution of $\Delta r/R_{\rm ib} = 10^{-3}$ in the innermost grid cell and $\Delta r/r < 0.013$ everywhere on the grid.

In order to investigate the effects of the thermal-bomb parameterization, we simulated models without a collapsing central core as well as models including the core collapse, varied the timescale $t_{\rm inj}$ of the energy deposition, and changed the location of the inner grid boundary.

- U and C are used as first letters to discriminate between the uncollapsed and collapsed models.
- A numerical value refers to the ZAMS mass (in units of $M_\odot$) of the progenitor model.
- A letter D or O is appended to distinguish the CCSN models with deep inner grid boundary at the location of the progenitor where $Y_e = 0.48$ from the models with the inner grid boundary farther out where $s/k_{\rm B} = 4$.
- A letter M at the end of the model names denotes simulations where the fixed mass value $\Delta M$ of the energy-injection layer was changed compared to the standard case with $\Delta M = 0.05\,M_\odot$.

A summary of all CCSN simulations studied for the four considered progenitor stars in this chapter is given in Table 3.2. The explosion energy, $E_{\rm exp}$, given in this table is defined as the integral of the sum of the kinetic, internal, and gravitational energies for all unbound mass, i.e., for all mass shells that possess positive values of the binding energy at the end of our simulation runs. We exploded our progenitors with an explosion energy of $E_{\rm exp} \approx 1\,{\rm B} = 10^{51}$ erg, namely 1.01 B for the $12.3\,M_\odot$ and $19.7\,M_\odot$ progenitors, 1.03 B for the $21.0\,M_\odot$ star, and 1.07 B for the $26.6\,M_\odot$ model. These energies are slightly different in order to compare the thermal bomb models discussed here to existing neutrino-driven 1D explosion models from the study by Sukhbold et al. (2016) in Chapter 5. In all cases and setups, the energy was calibrated to the mentioned value with a precision of 3%. The differences in the explosion energies of the different progenitors are not relevant for the present study.

In detail, the different setups and corresponding simulations are as follows.

#### Reference Models

We started our investigation with a setup that was guided by models discussed in SM19, i.e., the CCSN simulations did not include any collapse of the central core of the progenitors.

Table 3.2: Properties of the thermal-bomb models computed in this chapter. $M_{\rm ZAMS}$ is the ZAMS mass of the progenitor star, "Model" is our name for the specific CCSN simulation (see text), "Inner Grid Boundary" specifies the criterion for placing the inner grid boundary, $M_{\rm ib}$ is the corresponding enclosed mass, $t_{\rm coll}$ is the collapse time, $r_{\rm min}$ is the minimum radius for the collapse phase, $\Delta M$ is the mass of the energy-injection layer or, respectively, the initial mass in the volume where the energy is injected, $t_{\rm inj}$ is the range of energy-deposition timescales considered, and $E_{\rm exp}$ is the final explosion energy to which the CCSN models were calibrated. Note that per construction all 26.6 $M_\odot$ models have identical values for $\Delta M$ in this listing.

| $M_{\rm ZAMS}$ $[M_\odot]$ | Model | Inner Grid Boundary | $M_{\rm ib}$ $[M_\odot]$ | $t_{\rm coll}$ [s] | $r_{\rm min}$ [cm] | $\Delta M$ $[M_\odot]$ | $t_{\rm inj}$ [s] | $E_{\rm exp}$ $[10^{51}\,{\rm erg}]$ |
|---|---|---|---|---|---|---|---|---|
| 12.3 | U12.3D | $Y_e = 0.48$ | 1.230 | no coll | – | 0.05 | $0.01 - 2.0$ | 1.010 |
| 19.7 | U19.7D | $Y_e = 0.48$ | 1.256 | no coll | – | 0.05 | $0.01 - 2.0$ | 1.010 |
| 19.7 | C19.7D | $Y_e = 0.48$ | 1.256 | 0.45 | $5 \cdot 10^7$ | 0.05 | $0.01 - 2.0$ | 1.010 |
| 19.7 | C19.7O | $s/k_{\rm B} = 4$ | 1.533 | 0.45 | $5 \cdot 10^7$ | 0.05 | $0.01 - 2.0$ | 1.010 |
| 19.7 | U19.7DM | $Y_e = 0.48$ | 1.256 | no coll | – | 0.043 | $0.01 - 2.0$ | 1.010 |
| 19.7 | C19.7DM | $Y_e = 0.48$ | 1.256 | 0.45 | $5 \cdot 10^7$ | 0.044 | $0.01 - 2.0$ | 1.010 |
| 19.7 | C19.7OM | $s/k_{\rm B} = 4$ | 1.533 | 0.45 | $5 \cdot 10^7$ | 0.027 | $0.01 - 2.0$ | 1.010 |
| 21.0 | U21.0D | $Y_e = 0.48$ | 1.272 | no coll | – | 0.05 | $0.01 - 2.0$ | 1.026 |
| 21.0 | C21.0D | $Y_e = 0.48$ | 1.272 | 0.45 | $5 \cdot 10^7$ | 0.05 | $0.01 - 2.0$ | 1.026 |
| 21.0 | C21.0O | $s/k_{\rm B} = 4$ | 1.484 | 0.45 | $5 \cdot 10^7$ | 0.05 | $0.01 - 2.0$ | 1.026 |
| 21.0 | U21.0DM | $Y_e = 0.48$ | 1.272 | no coll | – | 0.042 | $0.01 - 2.0$ | 1.026 |
| 21.0 | C21.0DM | $Y_e = 0.48$ | 1.272 | 0.45 | $5 \cdot 10^7$ | 0.041 | $0.01 - 2.0$ | 1.026 |
| 21.0 | C21.0OM | $s/k_{\rm B} = 4$ | 1.484 | 0.45 | $5 \cdot 10^7$ | 0.068 | $0.01 - 2.0$ | 1.026 |
| 26.6 | U26.6D | $Y_e = 0.48$ | 1.383 | no coll | – | 0.05 | $0.01 - 2.0$ | 1.072 |
| 26.6 | C26.6D | $Y_e = 0.48$ | 1.383 | 0.45 | $5 \cdot 10^7$ | 0.05 | $0.01 - 2.0$ | 1.072 |
| 26.6 | C26.6O | $s/k_{\rm B} = 4$ | 1.738 | 0.45 | $5 \cdot 10^7$ | 0.05 | $0.01 - 2.0$ | 1.072 |

These U-models were supposed to permit a comparison with the results presented by SM19.

In all of the discussed U-models the inner boundary was placed at the location where $Y_e = 0.48$, and, in our default setup, the explosion energy was injected in a fixed mass layer with $\Delta M = 0.05\,M_\odot$, which was the same in all CCSN models for the set of progenitors. The inner boundary of this energy-deposition layer (IBED) was therefore chosen to be identical to the inner grid boundary. Note that in models with a fixed energy-deposition layer $\Delta M$, the outer radius of this shell, $R_{\rm OBED}$, moves outward as the heated mass, $\Delta M$, expands, whereas the inner radius, $R_{\rm IBED}$, is set to coincide with the inner grid boundary, $R_{\rm ib}$, and does not change with time in the U models.

The timescale of the energy deposition used in the energy input rate, $E_{\rm inj}/(\Delta M t_{\rm inj})$, was varied from 0.01 s to 2 s using the following values:

$$t_{\rm inj} = 0.01,\ 0.05,\ 0.2,\ 0.5,\ 1.0,\ 2.0\ {\rm s}\,. \tag{3.1}$$

We thus tested the influence of different durations of energy injection on the explosion dynamics and $^{56}$Ni production. Although our progenitors are different from those used by SM19, and also our setup for the CCSN simulations differs in details from the ones employed by SM19, the modelling approaches are sufficiently similar to permit us to reproduce the basic findings reported by SM19.

In Table 3.2 the corresponding models are denoted by U$M_*$D, where $M_*$ is used here as a placeholder for the mass value of the model. While our standard setup uses $\Delta M = 0.05\,M_\odot$, we also performed test runs with $\Delta M \approx 0.04\,M_\odot$ for the U-setup without finding any significant differences in the amount of $^{56}$Ni produced. These models are denoted by U$M_*$DM in Table 3.2. The choice of $\Delta M \approx 0.04\,M_\odot$ was made based on the requirement that at the starting time of the energy injection the radius ratio, $R_{\rm OBED}/R_{\rm IBED}$, for different models is the same for all the progenitors and corresponds to the radius ratio containing $\Delta M = 0.05 M_\odot$ for the progenitor $26.6 M_\odot$. Note, that it does not introduce new models for the $26.6 M_\odot$ progenitor based on the definition. The mass layers for the progenitors of $19.7 M_\odot$ and $21.0 M_\odot$ will not be the same and will depend on the density for each progenitor.

We did not consider any cases U$M_*$O because moving the inner grid boundary farther out will lead to lower densities in the ejecta (Figure 3.2). This will significantly reduce the amount of $^{56}$Ni synthesized in this setup, and, in particular, for long $t_{\rm inj}$ it will lead to even more severe underproduction of $^{56}$Ni compared to the yields inferred from observations of CCSNe with energies around $10^{51}$ erg (see Section 3.3.1).

### Including a Collapse Phase and Shifting the Inner Boundary

Instead of releasing thermal energy in the uncollapsed progenitor as assumed by SM19, we extended our setup by forcing the core of the progenitor to contract before depositing the energy. Adding such a collapse phase will change the dynamics of the explosion even with the same explosion energy and the same location of the inner boundary.

To this end, the inner grid boundary was moved inward for a time interval $t_{\rm coll}$ thus mimicking the collapse phase that precedes the development of the explosion. The time-

dependent velocity for contracting the inner boundary was implemented as in Woosley and Weaver (1995); Woosley et al. (2002); Woosley and Heger (2007), who applied this prescription within the framework of the classical piston method:

$$\frac{\mathrm{d}r}{\mathrm{d}t}(t) = v_0 - a_0 t \quad \text{for} \quad t < t_{\mathrm{coll}}\,, \tag{3.2}$$

where $v_0 < 0$ is the initial velocity of the inner boundary (following the infall of the progenitor model at the onset of its core collapse) and $a_0 = 2(r_0 - r_{\mathrm{min}} + v_0 t_{\mathrm{coll}})/t_{\mathrm{coll}}^2$ is a constant acceleration calculated in order to reach the minimum radius $r_{\mathrm{min}}$ after the collapse time $t_{\mathrm{coll}}$, with $r_0$ being the initial radius of the inner boundary. After this phase, the boundary contraction is stopped, matter begins to pile up around the grid boundary, and a shock wave forms at the interface to the still supersonically infalling overlying shells. Then, the deposition of internal energy by our thermal bomb was started.

So, Equation (3.2) basically defines the inward movement of the constant Lagrangian mass shell corresponding to the closed inner grid boundary. Its collapse is basically controlled by the parameters $t_{\mathrm{coll}}$ and $r_{\mathrm{min}}$, whereas the explosion phase is controlled by the thermal-bomb parameters $E_{\mathrm{inj}}$, $\Delta M$ (or $\Delta V$), and $t_{\mathrm{inj}}$ (see Section 2.2). Again, following the literature mentioned above, we adopt for our default collapse simulations $t_{\mathrm{coll}} = 0.45\,\mathrm{s}$ and the minimum radius $r_{\mathrm{min}} = 5 \cdot 10^7\,\mathrm{cm}$. In Table 3.2 the models with this collapse setup and the deep inner boundary are denoted by C$M_*$D.

In a variation of the setup for the C-models, we relocated the inner grid boundary outward to the base of the oxygen shell in the progenitor, i.e., to the radial position where $s/k_{\mathrm{B}} = 4$, with the goal of studying the influence on the $^{56}$Ni production. These models are denoted by C$M_*$O in Table 3.2. The real inner boundary would be located somewhere between D and O positions, where the D position would provide a deeper constraint for the inner boundary while being a rather extreme location.

Moreover, for both of these variations of the reference models, C$M_*$D and C$M_*$O, we also considered different mass layers of the energy deposition $\Delta M$, introducing new models C$M_*$DM and C$M_*$OM for the progenitors $19.7 M_\odot$ and $21.0 M_\odot$. The new mass layers are defined in the same way as for U$M_*$DM models, and it corresponds to the same radius ratio, $R_{\mathrm{OBED}}/R_{\mathrm{IBED}}$, containing $\Delta M = 0.05 M_\odot$ as in the $26.6 M_\odot$ progenitor. In this case, for the models C$M_*$DM, it is again $\sim 0.04 M_\odot$, while for the models C$M_*$OM, it changes to $\Delta M = 0.027 M_\odot$ for $19.7 M_\odot$ progenitor and to $\Delta M = 0.068 M_\odot$ for $21.0 M_\odot$. Such drastic changes can be explained based on the density profiles of the progenitors in the upper left panel of Figure 3.2. I want to draw your attention to the dashed vertical lines, where the location of the inner boundary is for these models. One can see that, for the $19.7 M_\odot$ progenitor, the density decline is much steeper afterwards than for the two others, explaining why the same radius ratio will be now containing much less mass.

## 3.3 Results and Discussion

The results are presented in Figures 3.4-3.8, where each panel plot corresponds to one setup: the upper panel is for the default setup U$M_*$D, the middle panel for the collapsed models

with a deep position of the inner boundary C$M_*$D, and the lower panel for collapsed models with the inner boundary at the base of the oxygen shell C$M_*$O. The models U$M_*$DM, C$M_*$DM and C$M_*$OM are also presented in Figures 3.4 and 3.8 with the dashed lines ($\Delta\widetilde{M}$ in the legend), although for the upper and middle panels they are overlapping with the solid lines and only make a difference for the lower panel.

### 3.3.1 Uncollapsed Models Compared to SM19

The nickel mass at the final time of our simulations ($t_\mathrm{f} \sim 10\,\mathrm{s}$) as a function of the energy deposition timescale in the default setup after post-processing is presented in the upper panel of Figure 3.4 for the four selected progenitors. The first thing that is immediately noticeable is a strong correlation between the nickel mass and the energy deposition time. Namely, for a short timescale the nickel mass is significantly higher, and it is getting lower as the timescale increases. This basically means that slower explosions tend to significantly suppress the production of nickel. This behavior agrees very well with the result obtained by SM19, seen in Figure 3.3, taken from SM19. This presents their results for three progenitors of 15, 20, and $25M_\odot$, and shows the final $^{56}$Ni mass produced in their explosions as a function of the energy injection timescale $t_\mathrm{inj}$, which corresponds to the energy growth timescale $t_\mathrm{grow}$ in SM19. From Figures 3.3 and 3.4, it could be concluded that faster explosions are more likely to produce enough nickel to match observations as opposed to the current physical picture of the explosion. This behavior could be understood from Figure 3.5, where there is a peak temperature as a function of enclosed mass for the $21.0M_\odot$ progenitor for different energy deposition timescales. For shorter timescales, the peak temperature is getting higher, and it takes longer for the temperature to decrease. Most of the nickel is produced during complete silicon burning, which is also indicated on the plot, and, when the temperature is higher, the cooling down or undergoing of the complete silicon burning takes longer therefore producing more nickel. There is a mass shell plot in Figure 3.6 for the $21.0M_\odot$ progenitor (for the $19.7M_\odot$ and $26.6M_\odot$ progenitors see Appendix C) where one can see the locations of the peak temperature for each mass shell, indicated by crosses. When the energy is deposited for longer the shock wave is a bit weaker, and the temperature is just not getting high enough.

For the $19.7M_\odot$ and $21.0M_\odot$ progenitors, the amount of nickel is very similar and significantly lower than for $26.6M_\odot$. As could be seen in the upper left panel of Figure 3.2, the densities for $19.7M_\odot$ and $21.0M_\odot$ are decreasing more quickly and their values are lower than for $26.6M_\odot$. As a consequence, the shock is going faster in this region, and the temperature is also decreasing more quickly (see Figure 3.7) leading to lower final nickel masses. Besides, the densities for $19.7M_\odot$ and $21.0M_\odot$ in the regions where most of the nickel is produced (these regions are indicated by crosses on Figure 3.2) are very similar to each other, and therefore the amount of nickel is very similar.

The density profile is not the only determining factor here, though, which is clear in comparison with the progenitor $12.3M_\odot$. We get an efficient production of nickel, which is much less dependent on the timescale, and this high production corresponds to high electron fraction, $Y_e$, even for lower and steeper density profiles, as can be seen in the lower

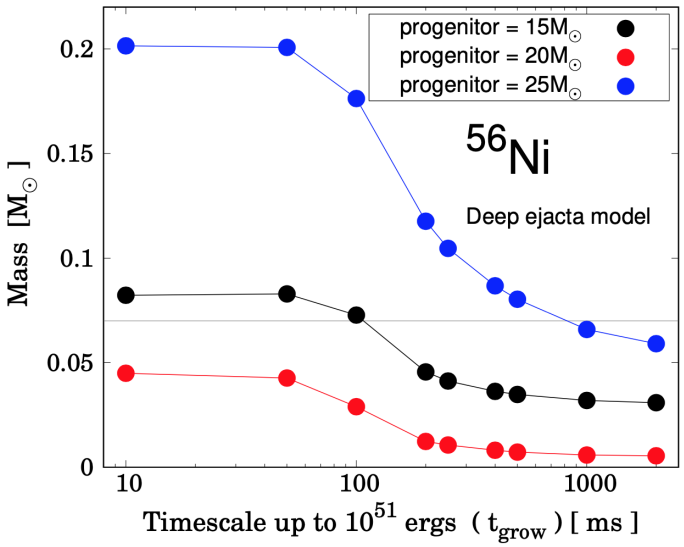


Figure 3.3: Figure 7, upper panel of SM19 reproduced, showing the final $^{56}$Ni mass produced in the explosions of their paper as a function of the energy injection timescale $t_{\rm inj}$, which corresponds to the energy growth timescale $t_{\rm grow}$ in SM19. The different colors correspond to the $15M_\odot$, $20M_\odot$, and $25M_\odot$ progenitors, as labelled in the panel. The thin gray horizontal line indicates the typical $^{56}$Ni yield of $0.07\,M_\odot$ for a $\sim 10^{51}$ erg explosion.

left panel of Figure 3.2. $12.3M_\odot$ has more shallow sensitivity to the timescale exactly because it produces nickel so efficiently. It does not really matter how much time it takes to deposit the energy, it is always producing a lot. This progenitor is very illustrative to see the spread of the models as well as that nickel production is not only relevant to the density profile of the progenitors, but also to the electron fraction.

We do not continue with the $12.3M_\odot$ progenitor because it did not show this dramatic variation with the respect to the timescale. Instead it shows an efficient production of nickel over all the timescales considered. Therefore, we continue with the models $19.7M_\odot$ and $21.0M_\odot$, which produce nearly no nickel, and $26.6M_\odot$, which has a very steep decline as a function of the timescale, as our primary models for the further discussion. One of our points is to show how the sensitivity to the timescale is dependent on the setup.

### 3.3.2 Collapsed Models

For the models C$M_*$D, the behavior of nickel production with the energy deposition timescale changes, as can be seen in the middle panel of Figure 3.4. What happens during collapse is that the material gets compressed and moved to higher densities, closer to where the shock is formed. When the matter is compressed, it affects the peak temperatures which are getting higher than for U$M_*$D models. Now the temperatures are increasing due to forced contractions of a star, while cooling down is more controlled by the energy deposition. The temperatures therefore are going more similarly through com-

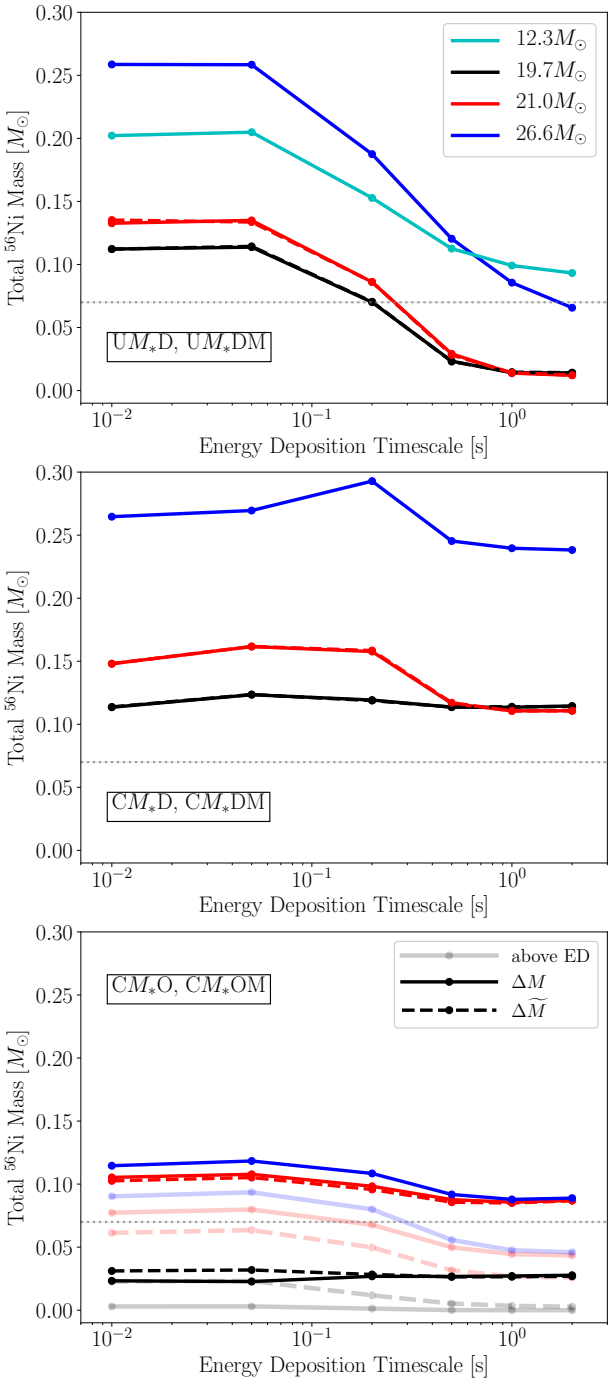


Figure 3.4: $^{56}$Ni yields as functions of energy-injection timescale for uncollapsed CCSN models (top panel) and collapsed models (middle panel) with deep inner grid boundary, and collapsed CCSN models with inner grid boundary shifted farther out (bottom panel). The different colors correspond to the different progenitors as labelled in the top panel. Solid lines belong to our standard choice of $\Delta M = 0.05\,M_\odot$ for the fixed mass in the energy-deposition layer and dashed lines refer to varied values of $\Delta M$ (see Table 3.2). Note, that in the top and middle panels the solid and dashed lines fall on top of each other. The light-colored lines (solid and dashed) in the bottom panel show the $^{56}$Ni yields when the mass in the energy-injection layer is excluded from the ejecta instead of only considering matter exterior to this layer as ejecta. Note, that in the bottom panel the blue solid and dashed lines fall on top of each other by definition. The thin gray horizontal line indicates the typical $^{56}$Ni yield of 0.07 $M_\odot$ for a $\sim 10^{51}$ erg explosion, e.g., SN 1987A (Arnett et al., 1989).

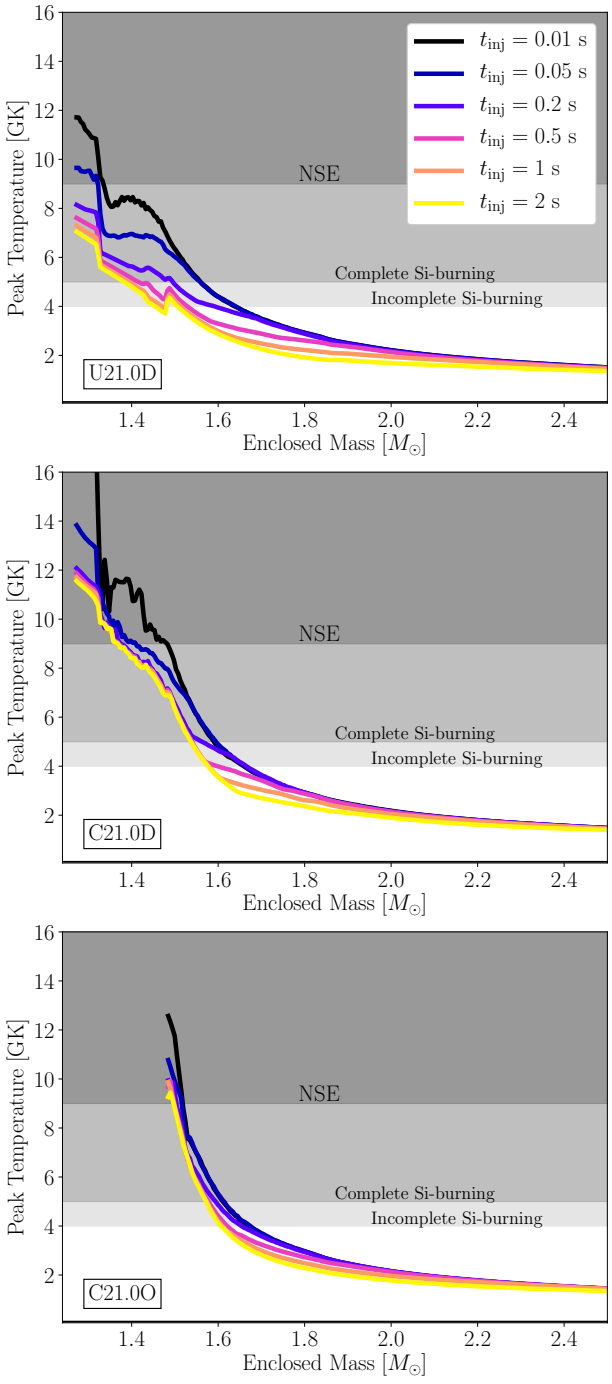


Figure 3.5: Peak temperatures as functions of enclosed mass for the CCSN runs with the $21\,M_\odot$ progenitor and different energy-injection timescales for the same modeling setups shown in Figure 3.4: uncollapsed (top), collapsed (middle), and collapsed with inner grid boundary shifted farther out (bottom). Different intensities of gray shading indicate different regimes of explosive nucleosynthesis as labelled. Note, that the peak temperatures are displayed only for the runs with our standard value of $\Delta M = 0.05\,M_\odot$ for the fixed mass in the energy-injection layer because the differences compared to the other choices of $\Delta M$ are effectively indistinguishable.

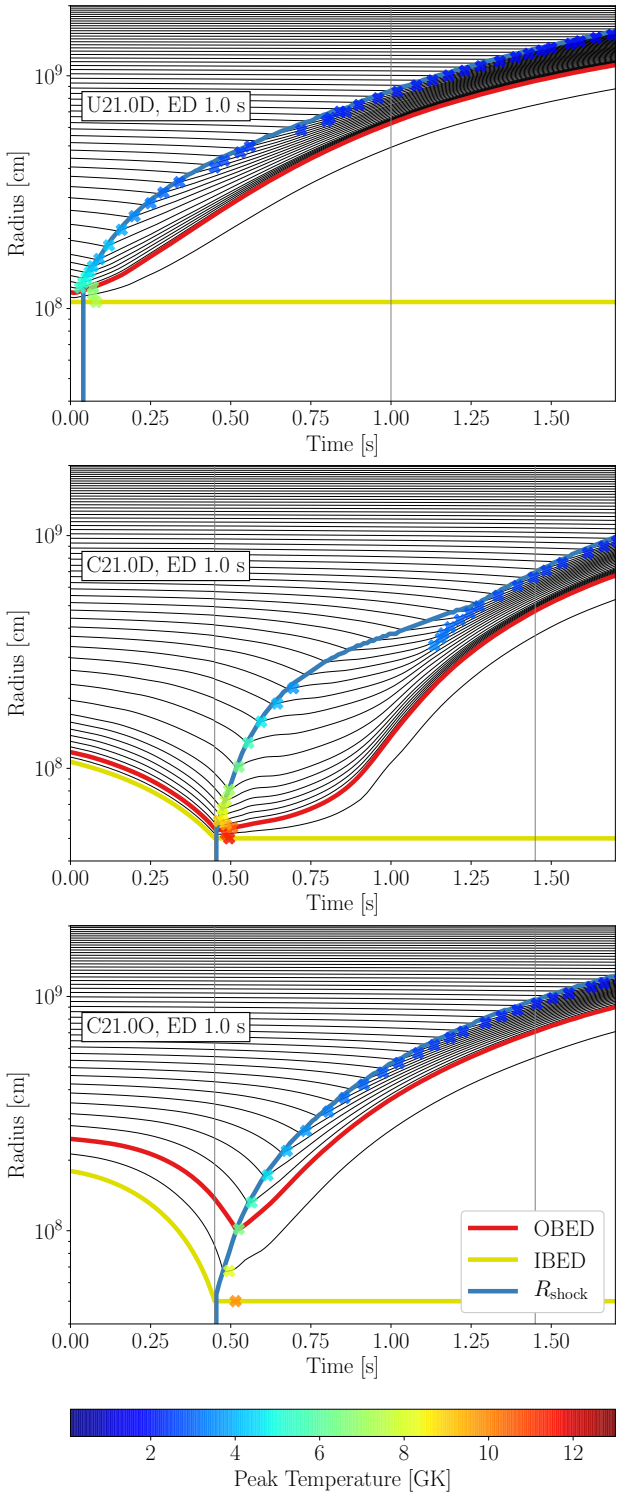


Figure 3.6: Radius evolution of Lagrangian mass shells with time for the CCSN runs of the 21 $M_\odot$ progenitor with standard value of $\Delta M = 0.05\,M_\odot$ for the fixed mass in the energy-injection layer and a representative energy-deposition timescale of 1 s: uncollapsed (top), collapsed (middle) with deep inner grid boundary, and collapsed with inner grid boundary shifted farther out (bottom). The thin black solid lines are the mass shells, spaced in steps of $0.025\,M_\odot$, the blue line marks the shock radius, the red line indicates $R_{\mathrm{OBED}}$, and the yellow line $R_{\mathrm{IBED}}$. Crosses indicate the moment when the peak temperature of each mass shell is reached; their colors correspond to temperature values as given by the color bar. Vertical lines indicate the start and the end of the energy deposition.

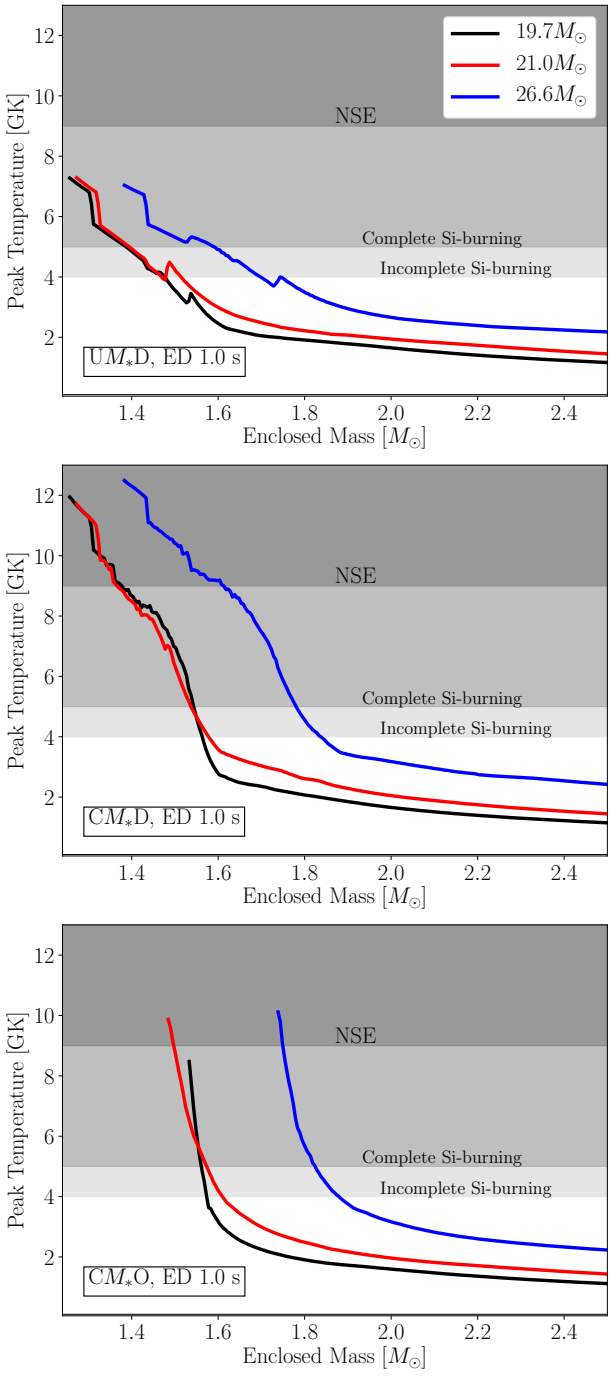


Figure 3.7: Peak temperatures as functions of enclosed mass for CCSN models for different progenitors using the standard value of $\Delta M = 0.05\,M_\odot$ for the fixed mass in the energy-injection layer and a representative energy-deposition timescale of 1 s: uncollapsed (top) and collapsed (middle) with deep inner grid boundary, and collapsed with inner grid boundary shifted farther out (bottom). Grey shading again indicates different regimes of explosive nucleosynthesis as in Figure 3.5. Note, that the peak temperatures are displayed only for the runs with our default choice of $\Delta M = 0.05\,M_\odot$, because the differences compared to the other choices of $\Delta M$ are effectively indistinguishable.

plete and incomplete Si burning for different timescales (see Figure 3.5, middle panel in comparison with upper panel). Final nickel mass is much less sensitive to the timescale and is higher than the observational value $0.07M_{\odot}$ indicating that there is no conflict with the results of 3D simulations or observations. Dramatic dependence on the timescale is only a consequence of the setup used for the models U$M_{*}$D.

For the $21.0M_{\odot}$ and $26.6M_{\odot}$ progenitors there is extra nickel produced for the timescale $t_{\mathrm{inj}} = 0.2\,\mathrm{s}$. As can be seen on the mass shell plot (Figure 3.6, middle panel), the location of the peak temperatures through the explosion indicates that there is a secondary wave produced which is more distinctive for slow explosions. If the energy is deposited very quickly, these two waves more or less immediately merge into one wave, and therefore we see nucleosynthesis from one shock. At the intermediate timescale $t_{\mathrm{inj}} = 0.2\,\mathrm{s}$ the second wave is a bit delayed compared to the first shock, and it creates extra nickel production, while, if the timescale is increased even further, the second wave does not achieve high temperatures anymore, and therefore there is no influence on the nickel production.

The overall nickel production is much higher for the $26.6M_{\odot}$ progenitor, as it was for U$M_{*}$D models due to its density structure. A less steep density profile (see Figure 3.2) results in a less steep temperature decline, as shown in Figure 3.7. Cooling for the $26.6M_{\odot}$ progenitor is slower leading to higher nickel production because the shock is a bit weaker. The $19.7M_{\odot}$ and $21.0M_{\odot}$ progenitors have similar structures and show very similar behavior for U$M_{*}$D explosions, but here they demonstrate slightly different trends. Due to its low density, the $19.7M_{\odot}$ progenitor is producing nickel very inefficiently overall, to the point where it is not sensitive to the timescale at all anymore. The density decline is steeper, and the temperature is not getting high enough even for shorter timescales leading to almost constant nickel mass value.

### 3.3.3 Shifted Inner Boundary

Once we move the inner boundary further out (see Figure 3.4, lower panel, solid lines), the amount of nickel gets much lower while still staying not very sensitive to the timescale. The amount of nickel for the $21.0M_{\odot}$ and $26.6M_{\odot}$ progenitors is very similar, despite a different progenitor structure, and the amount of nickel for the $19.7M_{\odot}$ progenitor drops almost completely to zero. Moreover, there is no formation of the secondary wave, as can be seen in the lower panel of Figure 3.6, since there is no dramatic changes in the density while depositing the energy.

Peak temperatures for different timescales look quite similar to each other (Figure 3.5, lower panel). After the drop in density, which corresponds to the base of the oxygen shell ($s/k_{\mathrm{B}} = 4$, Figure 3.2), the density for the $19.7M_{\odot}$ model decreases more steeply than for the other two models, and it affects the final nickel production through temperatures, as can be seen in the lower panel of Figure 3.7. The temperature for the $19.7M_{\odot}$ progenitor drops rather dramatically leading to a very low nickel production. Moreover, the density is generally really low, and the region corresponding to the same enclosed mass for the energy deposition is spread over a larger radius. There is a slightly different picture once the energy is deposited in the same initial radius ratio instead of the same mass interval

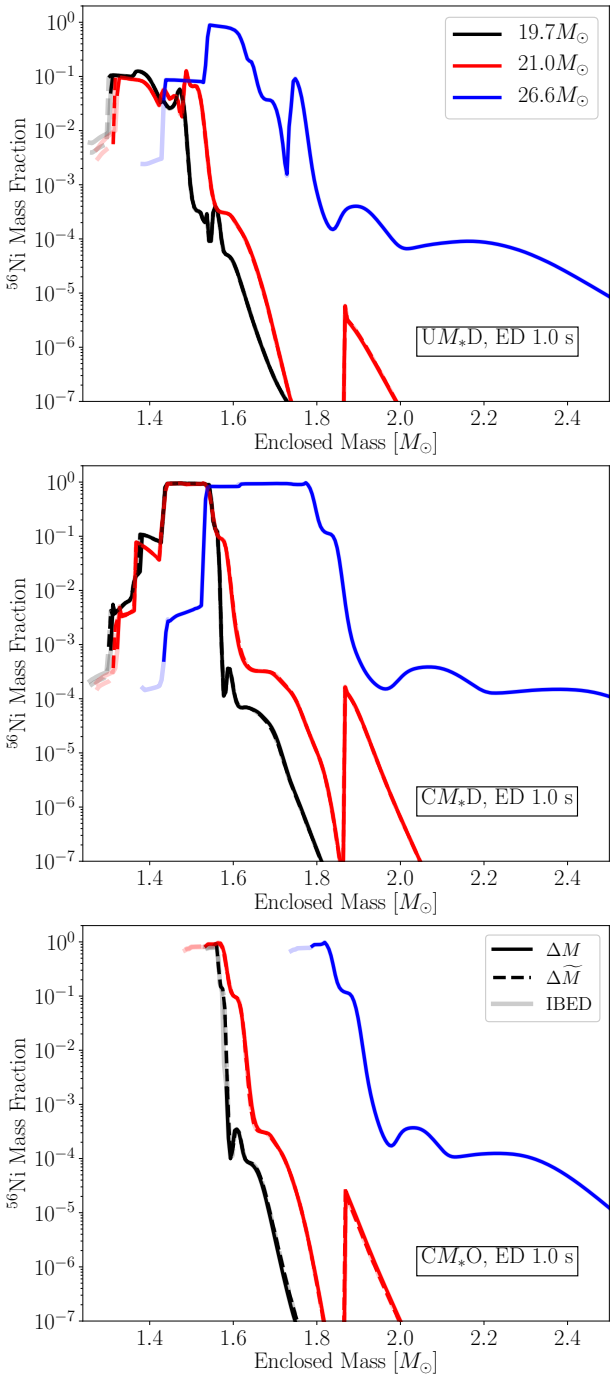


Figure 3.8: $^{56}$Ni mass fractions as functions of enclosed mass as produced in the CCSN models shown in Figure 3.7. Here, we plot the results for our standard value of $\Delta M = 0.05\,M_\odot$ for the fixed mass in the energy-injection layer (solid lines), for the cases with varied values of $\Delta M$ (dashed lines), and for the $^{56}$Ni production when the mass in the energy-injection layer is included in the ejecta (light-colored solid and dashed lines).

(see Figure 3.4, lower panel, dashed lines). It indeed changes the amount of nickel, and it is no longer zero for the $19.7M_\odot$ progenitor, while it decreases a bit for the $21.0M_\odot$ progenitor. Therefore, they become more evenly distributed in space. Due to different values of the densities in this region, the same mass interval can mean completely different volumes which is crucial for defining the dynamics of the explosion as well as for the final determination of the nickel mass. Overall one can see that the $^{56}$Ni yields in the C19.7O models are the lowest of all the three considered progenitors.

There is a difference between C-models with D-boundary and O-boundary; specifically, that in the latter the inclusion or exclusion of the heated mass $\Delta M$ in the ejecta can make a sizable difference in the $^{56}$Ni yield. In contrast to the U$M_*$D and C$M_*$D models, the simulations with collapse and O-boundary produce considerably less $^{56}$Ni when the matter in the energy-injection layer is not taken into account in the ejecta (see the light-colored solid lines in the bottom panel of Figure 3.4). In particular, C19.7O massively underproduces $^{56}$Ni in this case, and, for the models with the $21.0\,M_\odot$ and $26.6\,M_\odot$ progenitors, we again witness a strong trend of decreasing $^{56}$Ni yields with longer energy-injection timescales when only material exterior to $R_{\rm OBED}$ is counted as ejecta.

Such a trend, however, disappears essentially entirely when the $^{56}$Ni nucleosynthesized in the energy-deposition layer is included in the ejecta (heavy solid lines compared to light-colored solid lines in the bottom panel of Figure 3.4). We recall that the inclusion or exclusion of the heated mass from the ejecta does not have any relevant influence on the total $^{56}$Ni yields of our U- and C-models with deep inner boundary because the low $Y_e$ in the vicinity of this boundary location (see Figure 3.2) prevents abundant production of $^{56}$Ni in the heated mass layer (Figure 3.8, top and middle panels). The situation is different now for the O-models because $Y_e$ is close to 0.5 near the inner grid boundary in this case (Figure 3.2). Much of the $^{56}$Ni is then produced in the mass layers just exterior to $R_{\rm ib}$. Additionally, the total $^{56}$Ni yields are much smaller (Figure 3.8, bottom panel). Therefore, the $^{56}$Ni assembled in the heated mass can make a significant or even dominant contribution to the total yield of this isotope. The C19.7O models are the most extreme cases in this respect. Their $^{56}$Ni yields are extremely low when only matter exterior to the heated layer is considered as ejecta. This is especially problematic since our default value of $0.05\,M_\odot$ for the energy-injection mass, $\Delta M$, is fairly large. This fact is further illuminated in the following section, where we will discuss the results for variations of $\Delta M$.

## 3.4 Conclusions

In this chapter we presented the results of the thermal bomb calculations in comparison with the work SM19, as well as changing their setup by adding the collapse phase of the explosion and shifting the inner boundary to the base of the oxygen shell in a progenitor. The explosion results were post processed with the extended reaction network SkyNet with 262 isotopes, and the final nickel mass after post-processing was used as a diagnostic tool. The main results we considered here include the final nickel mass produced in the explosion as a function of the parameter of the thermal bomb mechanism: the energy deposition

timescale, $t_{\rm inj}$. The rest of the results contain the peak temperatures for different energy deposition timescales as well as for different progenitors, mass shell plots demonstrating the dynamics of the explosions, and the nickel mass fractions as functions of the enclosed mass.

In the first section of this chapter, the progenitors used in this work were described in all details. The progenitors have the zero-age-main-sequence masses of $M_{\rm ZAMS} = 12.3, 19.7, 21.0$ and $26.6 M_\odot$ to cover the whole relevant mass range. Based on the results of the comparison, we eliminated the $12.3 M_\odot$ progenitor since it showed much less sensitivity of the nickel production on the energy deposition timescale.

Then the thermal bomb setups were described. We adopted the prescription of SM19 for our reference models, and then added the collapse phase in the same way that is usually used for the classic piston approach. For the collapsed models, we also tried to shift the inner boundary and took a look how that will affect the dynamics of the explosions and the final nickel production.

In the next section, we presented the discussion of the results obtained with the described setups. We were able to reproduce the behavior of the final nickel mass achieved by SM19, namely the dependence of the mass on the energy deposition timescale. With the uncollapsed U$M_*$D setup, the slower explosions tend to greatly suppress the nickel production resulting in an insufficient amount of nickel for the explosions with $t_{\rm inj} > 0.2\,$s. This in fact contradicts the results of 3D simulations. To investigate this question further we added the collapse phase to the explosion, leaving all the rest of the parameters to be the same, introducing the C$M_*$D explosion models. With this change we saw that the strong sensitivity of the nickel production is gone, and the nickel mass is almost constant for all the energy deposition timescales. There is another feature that is present for this setup though, which is an increased nickel mass for the intermediate timescale $t_{\rm inj} = 0.2\,$s. We explained this via the formation of the secondary shock that has a high enough temperature to produce additional nickel. For the slower explosions with the higher energy deposition timescales, the second shock wave is formed as well, but it no longer achieves the sufficient temperatures for nickel to be synthesized. This all can be well seen in Figure 3.6.

Next we shifted the inner boundary location to the base of the oxygen shell, introducing the models C$M_*$O. The amount of nickel produced comparing to C$M_*$D is greatly reduced. The second shock is no longer formed so the feature that was present for the C$M_*$D models is not here anymore. But the results are again much less dependent on the energy deposition timescale, indicating that the strong dependence was a clear consequence of the used setup for the models U$M_*$D and has no physical meaning because the collapse is happening and cannot be ignored in the 1D-models.

Moreover, we also tried to change the mass layer of the energy deposition, setting it to be the one corresponding to the same radius ratio containing $\Delta M = 0.05 M_\odot$ in the $26.6 M_\odot$ progenitor. These results only showed some difference for the C$M_*$O setup. On top of that, for this setup, it also makes a difference which matter is considered ejected. If we only consider the matter above OBED ejected, it reduces the final nickel since it is primarily produced in the innermost region of the star very close to the location of the inner boundary.

For the main conclusion here, I want to underline that the nickel is very sensitive to the setup of the thermal bomb explosions, and it is important to understand before interpreting the results of the simulations. Once the collapse phase of the explosion is taken into account, there is no conflict with 3D results.

# Chapter 4

# Overview of the Parameters of Thermal Bomb Explosions

## 4.1 Introduction

In this chapter we want to demonstrate the broader overview of the parameters of the thermal bomb explosion mechanism. To do that we use the same progenitors that were described in details in Section 3.2.1. The main parameters of thermal bomb explosions are the amount of the injected energy, the mass layer (or volume) and the timescale of the energy deposition. Moreover, adding the collapse phase of the explosion introduces two more parameters – the minimum radius and the time where the collapse is happening. Across all the results we change the energy deposition timescale to show how different setups can change the overall picture of the explosion. The amount of the injected energy is varied in order to get the desired explosion energy. In the present chapter we first of all consider more drastic changes of the mass layer of the energy deposition. Then we take a look at what will happen if instead of depositing the energy in the constant mass layer, we do it in the fixed volume space essentially fixing the outer radius of the energy deposition. Finally we try to shrink the core to a smaller radius in the collapse phase to test how it would affect the final results. The results of this chapter are contained in the submitted publication (Imasheva et al., 2022). The current chapter partially contain the text from the paper, which was written by me together with the coauthors, and all the models were calculated by me.

## 4.2 Setups of the Explosions

To take a closer look at how changing the parameters of the explosions will change the final picture of the explosion, we exploded the progenitor stars with the code P-HOTB. To describe our models here we used the following indicators, with the first three points being the same as in Chapter 3:

- U and C are used as first letters to discriminate between the uncollapsed and collapsed models.

- A numerical value refers to the ZAMS mass (in units of $M_\odot$) of the progenitor model. It is replaced by $M_*$ as a placeholder in generic model names.

- A letter D or O is appended to distinguish the CCSN models with deep inner grid boundary at the location of the progenitor where $Y_e = 0.48$ from the models with the inner grid boundary farther out where $s/k_\mathrm{B} = 4$.

- A letter M' with a prime at the end of the model name denote simulations where the fixed mass value, $\Delta M$, of the energy-injection layer was changed to $\Delta M = 0.005 M_\odot$ compared to the standard case with $\Delta M = 0.05\, M_\odot$.

- A letter V instead of M at the end of the model names denotes those simulations where the energy is injected into a fixed volume, $\Delta V$, instead of a fixed mass shell $\Delta M$.

- Letters xC at the beginning of the model names indicate that the collapse of these models was prescribed to reach an "extreme" radius, smaller than in the C-models.

Let me now go into the details of the new setups. The details of the explosions used in this chapter are presented in Table 4.2.

### 4.2.1 Varying the Mass Layer of the Energy Deposition

In Chapter 3 we considered the default mass layer of the energy deposition to be $\Delta M = 0.05 M_\odot$ with small changes to be somewhere between $\Delta M = 0.027 M_\odot$ and $\Delta M = 0.068 M_\odot$. In this chapter, we want to take a look at the models with the mass layer of the energy deposition being drastically smaller than our default value, so we changed it to be one order of a magnitude less: $\Delta M = 0.005 M_\odot$. These models are indicated by U$M_*$DM' and C$M_*$OM'and are presented in the comparison with our default models, U$M_*$D and C$M_*$O.

### 4.2.2 Fixed Volume of the Energy Deposition

For these models, we fix the volume of the energy deposition instead of fixing the mass layer. Basically, it will change the energy input rate $E_\mathrm{inj}/(t_\mathrm{inj}\Delta M)$ to $E_\mathrm{inj}/(t_\mathrm{inj}\Delta V)$, where the initial and final radius of the energy deposition will now be fixed. Since the initial radius of the energy deposition, or $R_\mathrm{IBED}$, is equal to the inner boundary of the calculation, $R_{ib}$, and it is kept constant, it will only change the outer radius of the deposition, $R_\mathrm{OBED}$. In our simulations we chose the outer radius to be the same as for the $26.6 M_\odot$ progenitor,

Table 4.1: Parameters for our thermal-bomb models with fixed energy-deposition volume.

| $M_{\rm ZAMS}$ | C$M_*$OV | | | xC$M_*$OV | | |
|---|---|---|---|---|---|---|
| | $\Delta M$ | $R_{\rm IBED}$ | $R_{\rm OBED}$ | $\Delta M$ | $R_{\rm IBED}$ | $R_{\rm OBED}$ |
| $[M_\odot]$ | $[M_\odot]$ | [cm] | [cm] | $[M_\odot]$ | [cm] | [cm] |
| 19.7 | 0.027 | $5 \cdot 10^7$ | $17.6 \cdot 10^7$ | 0.027 | $1.5 \cdot 10^7$ | $15.88 \cdot 10^7$ |
| 21.0 | 0.068 | $5 \cdot 10^7$ | $17.6 \cdot 10^7$ | 0.068 | $1.5 \cdot 10^7$ | $15.88 \cdot 10^7$ |
| 26.6 | 0.050 | $5 \cdot 10^7$ | $17.6 \cdot 10^7$ | 0.050 | $1.5 \cdot 10^7$ | $15.88 \cdot 10^7$ |
| ratio | 3.519 | | | 10.587 | | |

corresponding to the mass layer $0.05 M_\odot$, and kept the outer radius the same for the rest of the progenitors. This ensures that the radius ratio is the same for all the progenitors:

$$\text{ratio} = \frac{R_{\rm OBED}}{R_{\rm IBED}}(26.6 M_\odot) = \frac{R_{\rm OBED}}{R_{\rm IBED}}(21.0 M_\odot) = \frac{R_{\rm OBED}}{R_{\rm IBED}}(19.7 M_\odot)\,. \tag{4.1}$$

Accordingly, the enclosed mass changes because of the different density structures of the progenitors. These models are denoted by C$M_*$OV in our list of models, and their details are presented in Tables 4.2 and 4.1.

### 4.2.3 Changing the Minimum Radius of the Collapse

Finally, we tried to change the minimum radius where the matter bounces and starts to move outward. Our initial choice of $r_{\rm min} = 500\,$km was inspired by the classic piston approach (Woosley and Weaver, 1995), and we will make use of it further to compare thermal bomb and piston driven explosions in the next chapter. However, in reality the core could be shrunk much more, so we employed another value $r_{\rm min} = 150\,$km for the test models in this chapter. It is close to the radial location of the neutrino-heating layer in neutrino-driven explosion models. It will come into play in the expression of the artificial movement of the inner boundary for the time $t < t_{\rm coll}$, where we kept the value $t_{\rm coll} = 0.45\,$s for the time of the collapse:

$$\frac{{\rm d}r}{{\rm d}t}(t) = v_0 - a_0 t \quad \text{for} \quad t < t_{\rm coll}\,. \tag{4.2}$$

Here $v_0 < 0$ is the initial velocity of the inner boundary (following the infall of the progenitor model at the onset of its core collapse), and $a_0 = 2(r_0 - r_{\rm min} + v_0 t_{\rm coll})/t_{\rm coll}^2$ is a constant acceleration calculated in order to reach the minimum radius $r_{\rm min}$ after the collapse time $t_{\rm coll}$, with $r_0$ being the initial radius of the inner boundary.

For this setup, we also considered both fixed mass layer and fixed volume of the energy deposition. These models are indicated by xC$M_*$O and xC$M_*$OV respectively in our list of models, and their details are presented in Tables 4.2 and 4.1.

Table 4.2: Properties of the thermal-bomb models computed in this chapter. $M_{\rm ZAMS}$ is the ZAMS mass of the progenitor star, "Model" is our name for the specific CCSN simulation (see text), "Inner Grid Boundary" specifies the criterion for placing the inner grid boundary, $M_{\rm ib}$ is the corresponding enclosed mass, $t_{\rm coll}$ is the collapse time, $r_{\rm min}$ is the minimum radius for the collapse phase, $\Delta M$ is the mass of the energy-injection layer or, respectively, the initial mass in the volume where the energy is injected, $t_{\rm inj}$ is the range of energy-deposition timescales considered, and $E_{\rm exp}$ is the final explosion energy to which the CCSN models were calibrated. Note that per construction all 26.6 $M_\odot$ models have identical values for $\Delta M$ in this listing.

| $M_{\rm ZAMS}$ $[M_\odot]$ | Model | Inner Grid Boundary | $M_{\rm ib}$ $[M_\odot]$ | $t_{\rm coll}$ [s] | $r_{\rm min}$ [cm] | $\Delta M$ $[M_\odot]$ | $t_{\rm inj}$ [s] | $E_{\rm exp}$ $[10^{51}\,{\rm erg}]$ |
|---|---|---|---|---|---|---|---|---|
| 12.3 | U12.3DM' | $Y_e = 0.48$ | 1.230 | no coll | – | 0.005 | $0.01 - 2.0$ | 1.010 |
| 19.7 | U19.7DM' | $Y_e = 0.48$ | 1.256 | no coll | – | 0.005 | $0.01 - 2.0$ | 1.010 |
| 19.7 | C19.7OM' | $s/k_{\rm B} = 4$ | 1.533 | 0.45 | $5 \cdot 10^7$ | 0.005 | $0.01 - 2.0$ | 1.010 |
| 19.7 | C19.7OV | $s/k_{\rm B} = 4$ | 1.533 | 0.45 | $5 \cdot 10^7$ | 0.027 | $0.01 - 0.5$ | 1.010 |
| 19.7 | xC19.7O | $s/k_{\rm B} = 4$ | 1.533 | 0.45 | $1.5 \cdot 10^7$ | 0.05 | $0.01 - 2.0$ | 1.010 |
| 19.7 | xC19.7OV | $s/k_{\rm B} = 4$ | 1.533 | 0.45 | $1.5 \cdot 10^7$ | 0.027 | $0.01 - 2.0$ | 1.010 |
| 21.0 | U21.0DM' | $Y_e = 0.48$ | 1.272 | no coll | – | 0.005 | $0.01 - 2.0$ | 1.026 |
| 21.0 | C21.0OM' | $s/k_{\rm B} = 4$ | 1.484 | 0.45 | $5 \cdot 10^7$ | 0.005 | $0.01 - 2.0$ | 1.026 |
| 21.0 | C21.0OV | $s/k_{\rm B} = 4$ | 1.484 | 0.45 | $5 \cdot 10^7$ | 0.068 | $0.01 - 1.0$ | 1.026 |
| 21.0 | xC21.0O | $s/k_{\rm B} = 4$ | 1.484 | 0.45 | $1.5 \cdot 10^7$ | 0.05 | $0.01 - 2.0$ | 1.026 |
| 21.0 | xC21.0OV | $s/k_{\rm B} = 4$ | 1.484 | 0.45 | $1.5 \cdot 10^7$ | 0.068 | $0.01 - 2.0$ | 1.026 |
| 26.6 | U26.6DM' | $Y_e = 0.48$ | 1.383 | no coll | – | 0.005 | $0.01 - 2.0$ | 1.072 |
| 26.6 | C26.6OM' | $s/k_{\rm B} = 4$ | 1.738 | 0.45 | $5 \cdot 10^7$ | 0.005 | $0.01 - 2.0$ | 1.072 |
| 26.6 | C26.6OV | $s/k_{\rm B} = 4$ | 1.738 | 0.45 | $5 \cdot 10^7$ | 0.05 | $0.01 - 1.0$ | 1.072 |
| 26.6 | xC26.6O | $s/k_{\rm B} = 4$ | 1.738 | 0.45 | $1.5 \cdot 10^7$ | 0.05 | $0.01 - 2.0$ | 1.072 |
| 26.6 | xC26.6OV | $s/k_{\rm B} = 4$ | 1.738 | 0.45 | $1.5 \cdot 10^7$ | 0.05 | $0.01 - 2.0$ | 1.072 |

## 4.3 Results and Discussion

### 4.3.1 Decreasing the Mass Layer

In our tests with a radical reduction of $\Delta M$ we changed the mass layer from our default value of $0.05\,M_\odot$ to the value of $0.005\,M_\odot$ adopted by SM19 for the fixed mass in the energy-deposition layer (U- and C-models in Table 3.2 with M' as endings of their names). These simulations reproduce the trend witnessed for the C19.7OM models compared to the C19.7O models in the bottom panel of Figure 3.4, namely that a reduced $\Delta M$ tends to increase the $^{56}$Ni production (see Figure 4.1). While the difference is small and, thus, has no relevant effect in the uncollapsed (and collapsed) models with the D-boundary (upper panel of Figure 4.1), the increase is more significant in the simulations with O-boundary (lower panel). However, considering all the results provided by Figures 3.4 and 4.1, one must conclude that, overall, the $^{56}$Ni yields are not overly sensitive to the exact value chosen for $\Delta M$, and that the corresponding variations are certainly secondary compared to the differences obtained between collapsed and uncollapsed models and between changing from D-boundary to O-boundary.

### 4.3.2 Fixed Mass or Fixed Volume of the Energy Deposition

In another variation of the thermal-bomb modeling, we performed runs with fixed volume, $\Delta V$, for the energy deposition constrained to simulations including the collapse phase and applying the O-boundary (models C$M_*$OV in Table 3.2). Since these simulations used the same volume for all three considered progenitors, the initial masses in the energy-injection volume were slightly different between these progenitors (Table 4.1). Moreover, these initial mass values were also different from the fixed masses, $\Delta M$, in the heating layer of the C$M_*$O models (except for the $26.6\,M_\odot$ case), against which we will compare the C$M_*$OV models. Although we found only a modest influence by variations of the fixed mass in the energy-deposition layer in Chapter 3, we will see that the moderate differences in the initial mass contained by the fixed heated volume can cause some peculiar relative differences in the behavior of the simulations for different progenitor masses.

Our CCSN models with a fixed volume for the energy-injection behave, overall, quite similarly to the models with fixed mass, as it can be seen, for example, in the mass shell plots on Figure 4.3 for the $21.0M_\odot$ progenitor (for equivalent plots in case of the $19.7M_\odot$ and $26.6M_\odot$ progenitors see Appendix C). This holds concerning the $^{56}$Ni yields (upper panel of Figure 4.2) as well as the explosion dynamics (left panels of Figure 4.3) and the peak-temperature distribution (left panels of Figure 4.4). However, the computation of the fixed $\Delta V$-models is partly more difficult and more time-consuming, because the time steps become small when the mass in energy-deposition volume decreases, and therefore the entropy per nucleon, $s$, increases. This implies a growth of the sound speed. Since $c_\mathrm{s} \approx \sqrt{(4/3)\cdot P/\rho} \propto \sqrt{(4/3)\cdot s\,T}$ for the radiation-dominated conditions in the heated volume, and therefore it leads to a corresponding reduction of the Courant-Friedrichs-Lewy limit for the length of the time steps. For this reason, our C$M_*$OV simulations with the

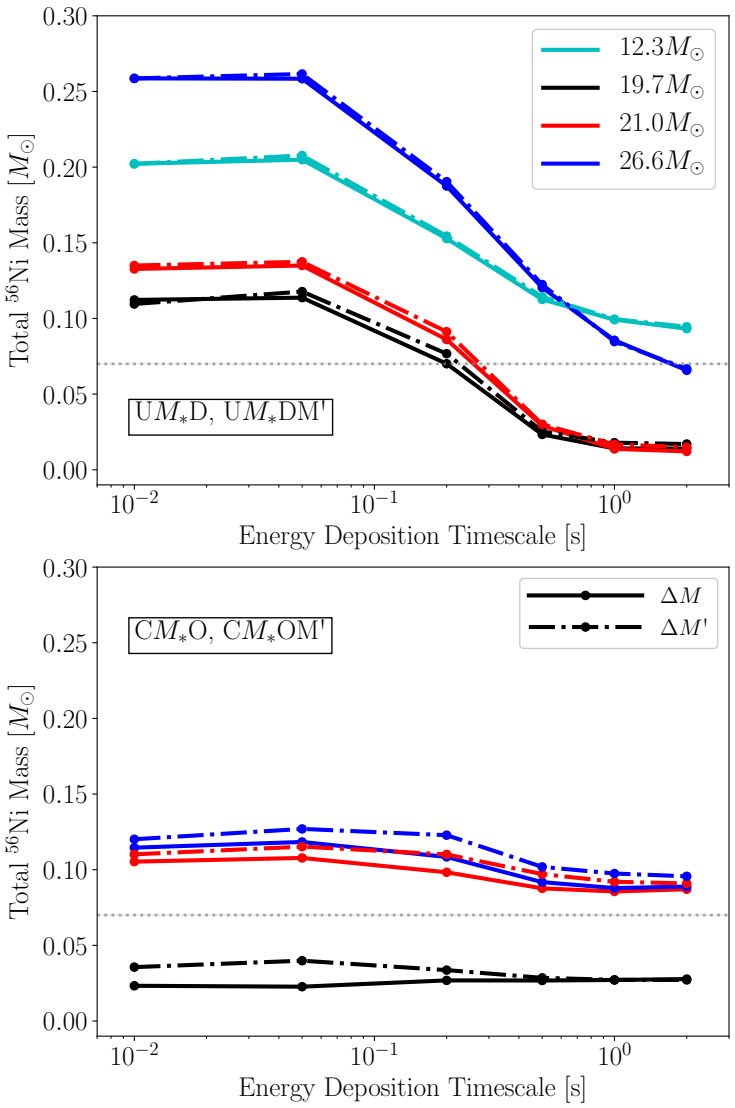


Figure 4.1: $^{56}$Ni yields as functions of energy-injection timescale for uncollapsed CCSN models (upper panel) and collapsed CCSN models with the inner grid boundary shifted farther out (lower panel). The different colors correspond to the different progenitors as labelled in the upper panel. Solid lines belong to our standard choice of $\Delta M = 0.05\,M_\odot$ for the fixed mass in the energy-deposition layer and dashed dotted lines refer to the values of $\Delta M' = 0.005 M_\odot$ (see Table 3.2). The thin gray horizontal line indicates the typical $^{56}$Ni yield of $0.07\,M_\odot$ for a $\sim 10^{51}$ erg explosion, e.g., SN 1987A (Arnett et al., 1989).

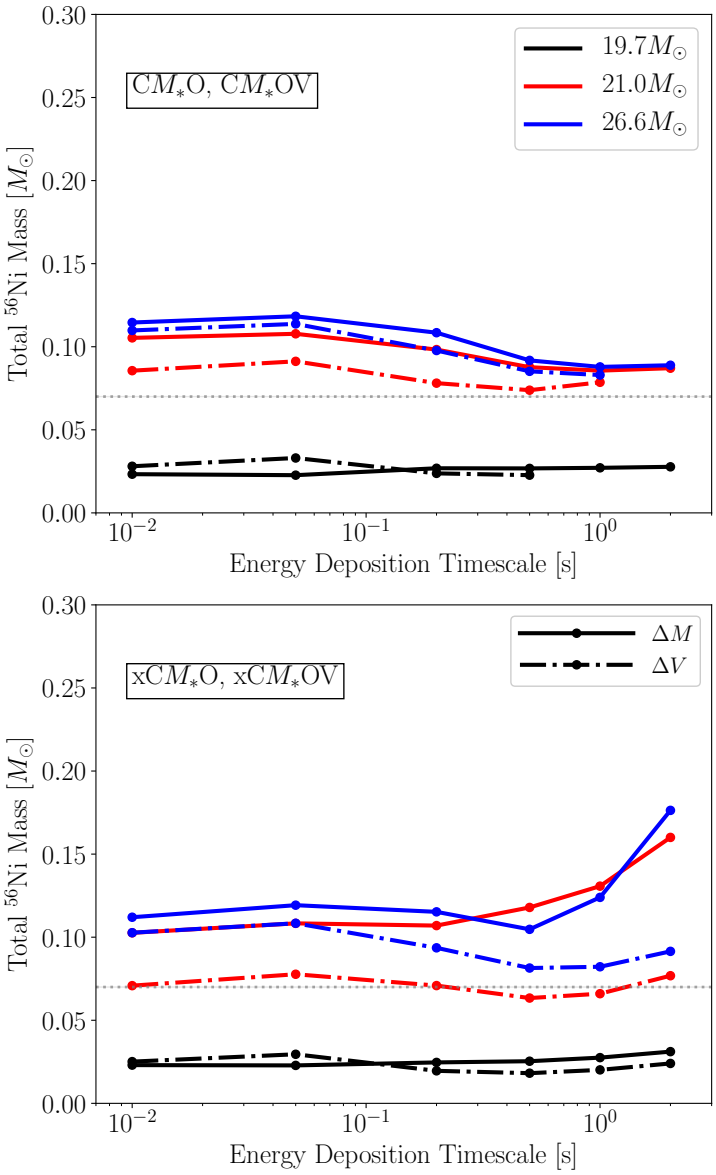


Figure 4.2: $^{56}$Ni masses as functions of energy deposition timescale for collapsed CCSN models: models with the fixed mass (solid lines) and fixed volume (dashed dotted lines) of the energy deposition with collapse to the $r_{\rm min} = 500\,$km (upper panel) and to the $r_{\rm min} = 150\,$km (lower panel). The different colors correspond to the different progenitors as labelled in the upper panel. The thin gray horizontal line indicates the typical $^{56}$Ni yield of $0.07\,M_\odot$ for a $\sim 10^{51}$ erg explosion, e.g., SN 1987A (Arnett et al., 1989).

longest energy-deposition timescales could partly not be finished due to their computational demands. Nevertheless, the available runs are sufficient to draw the essential conclusions.

In the upper panel of Figure 4.2 only minor differences in the $^{56}$Ni production are visible between the C$M_*$O models and the C$M_*$OV models. Only the 21.0 $M_\odot$ runs exhibit more sizable differences, i.e., the C21.0OV models eject systematically lower $^{56}$Ni yields than the C21.0O simulations, especially for short energy-injection times. The underlying reason for the special role of the C21.0OV models among the CCSN simulations for the three progenitors is the fact that the initially heated mass in the 21.0 $M_\odot$ models is the largest of all of the constant-volume models (see Table 4.1), whereas the heated volumes are the same for all other cases. In addition, the initial mass in the heated volume of the C21.0OV models is also larger than the mass in the heating layer of the C21.0O simulations (0.068 $M_\odot$ instead of 0.05 $M_\odot$). For this reason, the volume over which the heating is spread is greater in the C21.0OV models, reducing the heating rate per volume in the innermost ejecta. Therefore, the peak temperatures in the C21.0OV simulations remain lower than in the C21.0O models (Figure 4.4, left panels) where the heated mass is not only smaller but the energy injection also occurs into a fixed mass and thus follows the expanding gas. In contrast, in the C21.0OV simulations the heated gas expands out of the heated volume. For long heating timescales the energy injection into a fixed mass or a fixed volume makes little difference because the gas expands slowly. Therefore, the solid and dash-dotted lines in the upper panel of Figure 4.2 approach each other for all progenitors when the heating timescales are long. This is consistent with the observation that the peak temperatures in the left panels of Figure 4.4 become very similar for the higher values of $t_{\rm inj}$. Instead, if the heating timescale is short, the heated gas in the 21.0 $M_\odot$ models with fixed energy-deposition volume experiences lower heating rates per unit volume and moves out of the heated volume rather than being continuously heated as in the C21.0O models, where the heating shifts outward with the expanding matter. Therefore, the peak temperatures in particular of the innermost ejecta in the C21.0OV simulations with short $t_{\rm inj}$ remain lower than in the C21.0O models, and since the initially heated mass in the C21.0OV models is larger than in the fixed $\Delta V$-simulations for the other progenitors, this effect and the correspondingly lower $^{56}$Ni production are most pronounced in the C21.0OV runs.

### 4.3.3 Effects of Minimum Radius for Collapse

Finally, we also tested the influence of the minimum radius, $r_{\rm min}$, in the prescription of the initial collapse phase of the C-models by running thermal-bomb models with $r_{\rm min} = 150$ km, which is very close to the radial location of the neutrino-heating layer in neutrino-driven explosion models, instead of our canonical choice of $r_{\rm min} = 500$ km. For doing these tests we constrained ourselves to the models with O-boundary for a fixed mass layer, $\Delta M$, (models xC$M_*$O in Table 3.2) and a fixed volume, $\Delta V$, (models xC$M_*$OV in Table 3.2) for the energy injection, and we will compare them with the default-collapse models of C$M_*$O and C$M_*$OV. Here one has to keep in mind that all C$M_*$O and xC$M_*$O models for all progenitors were computed with exactly the same fixed mass of $\Delta M = 0.05\,M_\odot$ for the energy-injection layer. The C$M_*$OV and xC$M_*$OV models for a given progenitor had

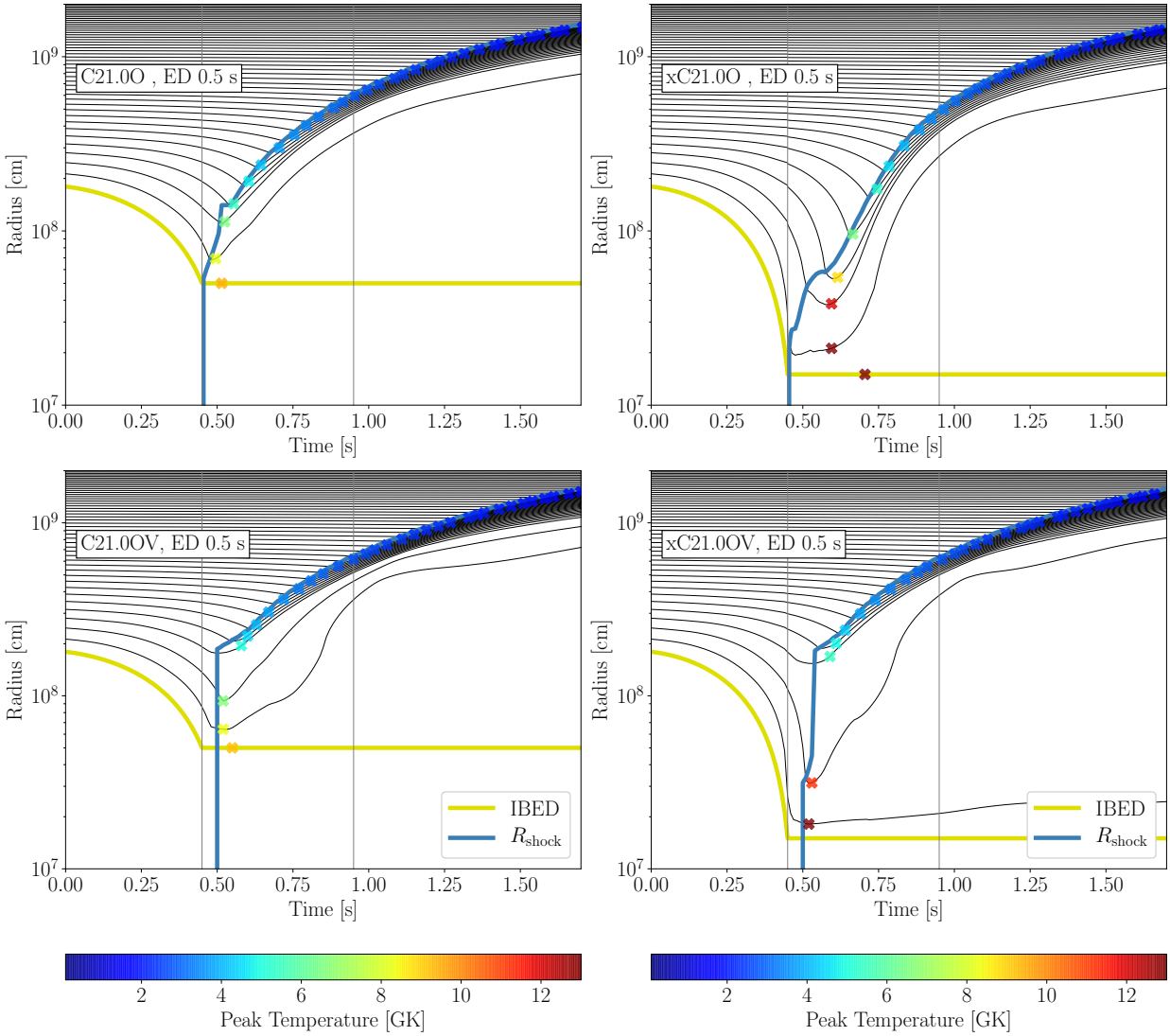


Figure 4.3: Radius evolution of Lagrangian mass shells with time for the CCSN runs of the 21 $M_\odot$ progenitor with a representative energy-deposition timescale of 0.5 s: the fixed mass of the energy deposition with collapse to the $r_{\rm min} = 500$ km (top left), the fixed mass of the energy deposition with collapse to the $r_{\rm min} = 150$ km (top right), the fixed volume of the energy deposition with collapse to the $r_{\rm min} = 500$ km (bottom left) and the fixed volume of the energy deposition with collapse to the $r_{\rm min} = 150$ km (bottom right). The thin black solid lines are the mass shells, spaced in steps of 0.025 $M_\odot$, the blue line marks the shock radius, and the inner boundary is indicated by the yellow. Crosses indicate the moment when the peak temperature of each mass shell is reached; their colors correspond to temperature values as given by the color bar in Figure 3.6. Vertical lines indicate the start and the end of the energy deposition.

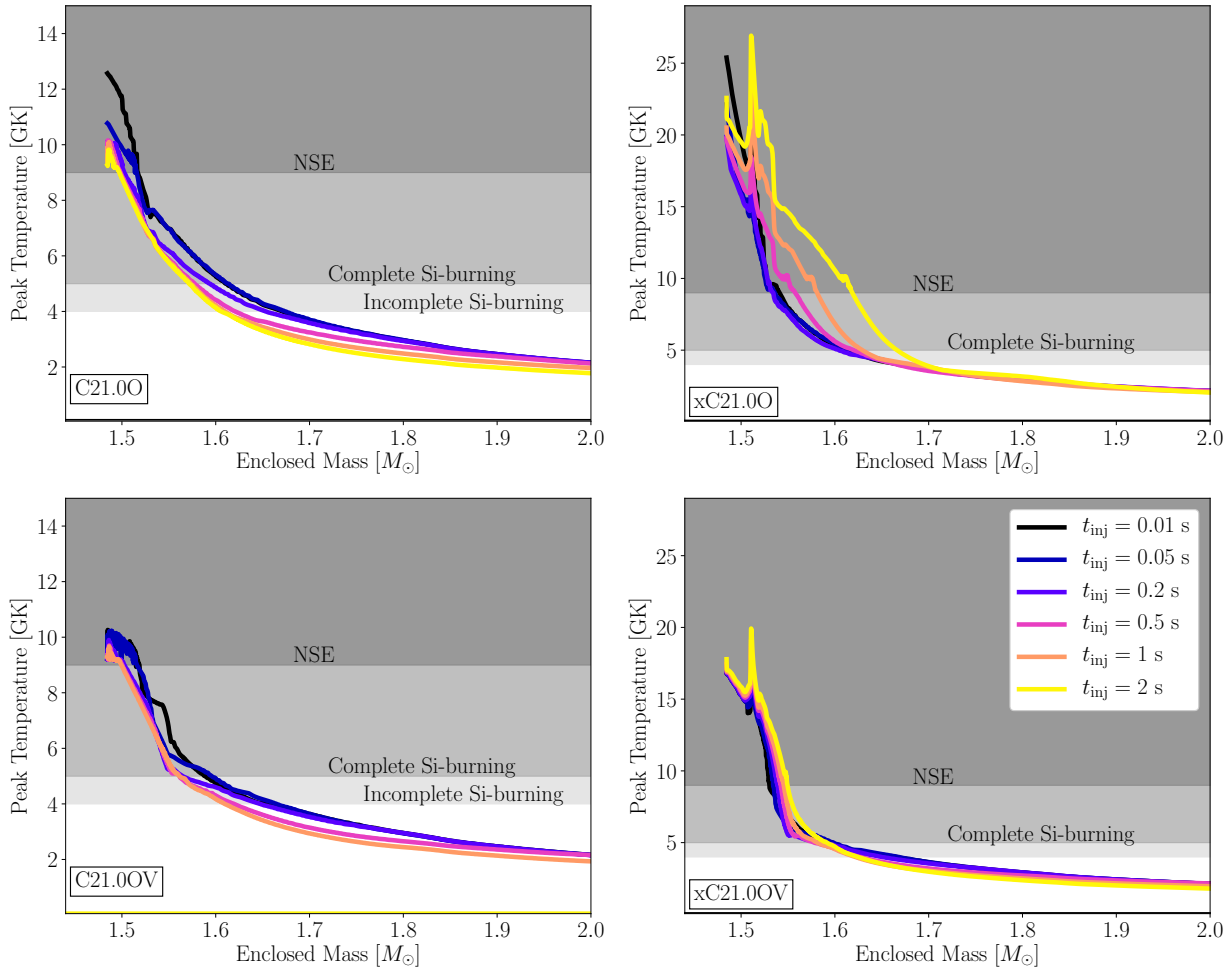


Figure 4.4: Peak temperatures as functions of enclosed mass for the CCSN runs with the 21 $M_\odot$ progenitor and different energy-injection timescales for the same modeling setups shown in Figure 4.3: the fixed mass of the energy deposition with collapse to the $r_{min}$ = 500 km (top left), the fixed mass of the energy deposition with collapse to the $r_{min}$ = 150 km (top right), the fixed volume of the energy deposition with collapse to the $r_{min}$ = 500 km (bottom left) and the fixed volume of the energy deposition with collapse to the $r_{min}$ = 150 km (bottom right). Different intensities of gray shading indicate different regimes of explosive nucleosynthesis as labelled.

effectively the same initial mass (up to the third digit) and nearly the same volume of the heated layer (Table 4.1). However, while the heated volume is the same in the CCSN runs for all progenitors, the initial masses in this volume differ between the three progenitors (Table 4.1).

Comparing the upper and lower panels of Figure 4.2, we witness only small differences in the $^{56}$Ni production for short heating timescales between the xC$M_*$O and the C$M_*$O simulations. Also, between the xC$M_*$OV and the C$M_*$OV simulations there are only relatively modest differences. The most prominent effect is a spreading between the $^{56}$Ni yields of the xC21.0O and xC21.0OV models that is about twice as big as it is between the C21.0O and C21.0OV cases. Additionally, there is a slightly greater gap between the yields of the xC26.6O and xC26.6OV simulations; this difference is again about half that size between the C26.6O and C26.6OV models and thus effectively insignificant. The reasons for the somewhat lower production of $^{56}$Ni in the fixed-volume models with short energy-injection times were discussed in Section 4.3.2, and they lead to stronger effects in simulations with more extreme collapse.

For long heating timescales we observe an interesting new phenomenon in the extreme-collapse models that is exactly opposite to the pronounced decrease of the $^{56}$Ni yields for longer $t_{\rm inj}$ in U-models reported by SM19 and reproduced by our calculations – and the similar but much weaker trends that one can spot in most of our C-models, too. Allowing for a deep collapse to $r_{\rm min} = 150\,$km we obtain increasing $^{56}$Ni yields for longer energy-injection timescales, in particular for the fixed-$\Delta M$ cases, but also, though less drastic, for the fixed-$\Delta V$ models (Figure 4.2, lower panel). (It is possible that a mild version of this trend is also present in our default-collapse models with fixed heating volume, but unfortunately the corresponding simulations for long $t_{\rm inj}$ could not be finished.) The increase of the $^{56}$Ni production for $t_{\rm inj} = 1\,$s and $2\,$s reverses the shallow decline that can be seen between $t_{\rm inj} = 0.05\,$s and $0.5\,$s.

The reason for this new effect can be inferred from the right panels of Figure 4.4. In stark contrast to all the other model sets plotted in Figure 3.5 and in the left panels of Figure 4.4, the extreme collapse models with the longest energy-injection times tend to reach higher peak temperatures in a wider mass range than the corresponding simulations with short $t_{\rm inj}$. This effect is particularly strong for the xC-models with fixed mass, $\Delta M$, of the heating layer (upper right panel of Figure 4.4 for the CCSN runs with the $21.0\,M_\odot$ progenitor). Comparing the right and left side panels of Figure 4.3 provides an explanation of this phenomenon. In the deep collapse cases, the matter is much more strongly compression-heated during the infall, and it also expands more slowly behind the shock than in the standard C-models. This effect is especially relevant when the heating timescales are long because in such cases the shock is less quickly accelerated outward, the gas ahead of the shock falls deeper into the gravitational potential of the newly formed neutron star, and when the outward moving shock sweeps up the infalling matter the higher gas velocities lead to much stronger shock heating. In addition, in the fixed-$\Delta M$ models the energy injection is initially constrained to a narrow volume containing $0.05\,M_\odot$, and it tracks the ejected matter. This leads to maximum peak temperatures in the mass shells well behind the shock (see upper right panel of Figure 4.3). In the fixed-$\Delta V$ models the heated volume

is considerably larger than the initial heating volume in the fixed-$\Delta M$ models. Therefore, the shock expansion reaches a larger radius within a shorter period of time preventing the deep infall of the preshock material in the xC-cases with fixed $\Delta V$. Consequently, the post-shock heating is less extreme in the simulations with fixed energy-injection volume than in the models with fixed mass (compare the upper and lower right panels of Figure 4.4). In the extreme collapse cases with fixed $\Delta V$, the heated volume is somewhat smaller than in the corresponding models with standard collapse because of smaller values of $R_{\mathrm{IBED}}$ and $R_{\mathrm{OBED}}$ (Table 4.1). Thus, the energy-deposition rate per volume in these xC-models is higher than in the C-models, and the innermost ejecta come from regions with stronger heating. For this reason also the xC models with fixed $\Delta V$ exhibit the trend to higher post-shock temperatures for long energy-injection timescales. Of course, the combined heating effect (compression by infall and shock plus energy injection) is significantly stronger when the heating follows the ejected mass in the xC$M_*$O models. Ergo these models exhibit a considerably steeper increase of the $^{56}$Ni production with longer $t_{\mathrm{inj}}$.

In contrast, for short heating timescales the expansion dynamics of models with default collapse and extreme collapse are quite similar, and the differences in the peak-temperature distributions are mostly connected to the initially stronger compression heating in the xC-models. However, in both prescriptions of the collapse phase, similar amounts of mass are heated to NSE and complete Si-burning temperatures (compare the upper left with the upper right panel and the lower left with the lower right panel in Figure 4.4). Therefore, the $^{56}$Ni yields for short $t_{\mathrm{inj}}$ are similar between the C-models and the xC-models of each progenitor and for both fixed $\Delta M$ and fixed $\Delta V$. The exception is the aforementioned $^{56}$Ni production in the xC21.0OV and xC26.6OV models compared to the xC21.0O and xC26.6O models is somewhat more reduced than in the C21.0OV and C26.6OV models relative to the C21.0O and C26.6O models (see the upper and lower panels of Figure 4.2).

## 4.4 Conclusions

The thermal bomb explosion mechanism is an artificial mechanism of CCSN explosion in spherical symmetry. It implies that the energy necessary for a star to explode is injected at the inner boundary in the certain mass layer and over a certain time period. It is called a thermal bomb because this energy is added to an internal energy which leads to the temperature rise. This mechanism is widely used in the community, it is very flexible and computationally not very expensive.

In this chapter, we presented an overview of the parameters of the thermal bomb explosions. First, we considered significantly decreasing the mass layer of the energy deposition while keeping the rest of the parameters fixed. These models are denoted by U$M_*$DM'and C$M_*$OM'. We found that changing the mass layer between $0.05M_\odot$ and $0.005M_\odot$ leads to some changes in the final nickel production, but the overall behavior stays the same. Namely, the slower explosions still tend to significantly suppress the nickel mass for the uncollapsed thermal bomb models, and this sensitivity to the energy deposition timescale is greatly reduced for the collapsed thermal bomb models.

Next, we tried to fix the volume of the energy deposition instead of fixing the mass. These models are indicated by C$M_*$OV. It changes the energy input rate in a way that the initial and final radius of the energy deposition will be now fixed. The volume is kept the same for all the progenitors. These models behave overall quite similarly to the models with fixed mass in the context of the final nickel mass and peak temperature distribution. The $21.0M_\odot$ progenitor shows more differences since its initially heated mass is the largest of all the constant-volume models, while the heated volumes are the same for all cases ($0.068M_\odot$ instead of $0.05M_\odot$).

Finally, we considered changing the collapse phase by reducing the minimum radius for the collapse. These models are denoted by xC$M_*$O and xC$M_*$OV. We changed the default value of 500 km, which was guided by the classic piston driven explosions, to the new value of 150 km, which is very close to the radial location of the neutrino heating layer in neutrino driven explosions. Here we considered again the fixed mass and the fixed volume of the energy deposition. There is systematically a bit less nickel produced in the fixed volume models with short energy deposition timescales, and it leads to stronger effects for more extreme collapse. Moreover, for long heating timescales and fixed mass energy deposition, we observe a new phenomenon in the extreme collapse models; namely that the final nickel mass is actually higher for longer timescales. It essentially means that slower explosions tend to overproduce nickel, which is opposite to the behavior of the uncollapsed models U$M_*$D presented in Chapter 3. It happens because the extreme collapse models with longer timescales reach higher peak temperatures in a wider mass range leading to the higher nickel production. The matter for extreme collapse is much more strongly heated during the infall, and it expands slower than in the standard C-models. At the same time, short explosions provide rather similar results for the final nickel production for both our default and extreme descriptions of collapse since similar amounts of mass are heated to NSE and complete Si-burning temperatures.

Therefore, we saw that the behavior of the final nickel mass is very sensitive to the setup of the thermal bomb explosion. For the uncollapsed models, slower explosions suppress nickel production, while for the extreme collapsed models the behavior is exactly the opposite. For the rest of the setups the final nickel mass is more or less independent of the energy deposition timescale, but, depending on the dynamics of the explosion, there could be other effects, and it is very important to understand the limitations of the explosion mechanisms as they could lead to misinterpreting the results.

Because of their numerous degrees of freedom, thermal-bomb models can certainly not be employed to assess the viability of any kind of physical explosion mechanism. For example, artificial explosion methods like the thermal bombs can hardly be expected to reproduce the dynamics of neutrino-driven explosions in a physically correct and reliable way. In particular, fixing the mass layer for the energy injection means that the energy input follows the expanding matter, which is unrealistic. Fixing instead the volume for the energy release either overestimates the heated volume or underestimates the heated mass in this heated volume, where in addition the mass decreases with time, which again is not a realistic description of the neutrino-driven mechanism. Fortunately, the $^{56}$Ni production of thermal bomb simulations that include a collapse phase turned out not to be overly

sensitive to such alternative choices.

Thermal bombs are a numerical recipe that depends on a variety of parameterized inputs that need to be defined. Nevertheless, even with the best choice of these inputs, their usefulness for quantitative predictions of iron-group and intermediate-mass-element nucleosynthesis will always be hampered by the unknown value of the explosion energy and, in principle, also of the initial mass cut. Moreover, iron-group species such as the isotopes of $^{56,57}$Ni and of $^{44}$Ti are formed in ejecta whose $Y_e$ is set by neutrino interactions and where multidimensional flows play a crucial role. Therefore, the best one can expect of any artificial explosion trigger is that the method should be set up such that it does not massively overproduce or underproduce nickel, and it should also be set up such that the correct trends of the $^{56}$Ni production with explosion energy, explosion timescale, and progenitor structure can be maintained.

Since thermal bombs provide an easy-to-apply recipe to trigger explosions, it is very likely that they will remain in use as a method of choice for the exploration of CCSN nucleosynthesis, for example in large sets of progenitor models, despite all the mentioned caveats. Summarizing the results of Chapters 3 and 4, the following prescriptions are recommended:

- Include a collapse phase before the energy release of the thermal bomb is started. A minimum collapse radius near 500 km seems to be sufficient and is computationally less demanding than a smaller radius.

- Since self-consistent simulations of neutrino-driven CCSNe show that the explosion sets in when the infalling Si/O interface reaches the stagnant bounce shock, the initial mass cut should be chosen near the $s/k_\mathrm{B} = 4$ location instead of putting it close to the edge of the iron core. Consequently, $Y_e$ in the layer of energy injection by the thermal bomb is very close to 0.5 (typically higher than 0.497).

- For this reason, $^{56}$Ni will be efficiently produced in the energy-injection layer, and the matter in this layer should be included in the ejecta if it becomes gravitationally unbound by the explosion.

- Using a fixed mass layer, $\Delta M$, for the energy injection is numerically easier than a fixed volume, and neither choice leads to any major differences. The exact value of $\Delta M$ is not crucial. We suggest $0.05\,M_\odot$, but smaller masses lead to very similar nickel yields.

- With the recommended setup, the $^{56}$Ni production is basically insensitive to the timescale chosen for the energy injection by the thermal bomb.

# Chapter 5

# Comparison between Different 1D Explosion Mechanisms

## 5.1 Introduction

The goal of this chapter is to look at all three explosion mechanisms simultaneously: thermal bomb, piston and neutrino-driven explosions. The main focus is again the final nickel production and what it depends on. While discussing the CCSN in spherical symmetry, people often use one explosion mechanism or one setup of a chosen explosion mechanism, but it is actually quite important to understand the limitations before discussing the results of any particular model, and here I want to demonstrate how the results can be affected by the mechanism used.

We selected two progenitors for this chapter, $21.0M_{\odot}$ and $26.6M_{\odot}$ from the previous chapter, since these two progenitors have the explosion energy $E_{\rm exp} \sim 1\,\mathrm{B}$ in the neutrino driven explosions, and they represent two different mass ranges. We are not aiming at providing a close investigation of the parameters here, but more at showing the general trends in the comparison. The summary of the models presented in this chapter can be found in Table 5.2.

## 5.2 Setups of the Explosions

Neutrino-driven explosions demonstrate the mechanism that is the least dependent on free parameters, since the final proto-neutron mass and the explosion energy are not in fact parameters of the mechanism but are calculated based on the neutrino engine simulating the shock wave. In order to compare different mechanisms with each other, all of them were calibrated with 3% precision to the same explosion energy given by the neutrino-driven explosion. The explosion energy is defined here as the integral of the sum of the kinetic, internal and gravitational energies for all the mass shells with a positive binding energy. It is usually converged after around 80 s of simulation time for thermal bomb and piston explosions. Let me now briefly describe the setups of the explosions that were used in this

chapter.

### 5.2.1 Piston

The classical procedure of the piston prescription was introduced by Woosley and collaborators (Woosley and Weaver, 1995; MacFadyen et al., 2001). It implies a certain position of the inner boundary, $M_{\rm pist}$, time, and the location of the bounce. The parameters are set to $t_{\rm coll} = 0.45\,{\rm s}$ and $r_{\rm min} = 5 \cdot 10^7\,{\rm cm}$, with the mass cut placed at the base of the oxygen shell (defined as the point where the dimensionless entropy $s/k_{\rm B}$ is equal to 4). For the classical piston, the collapse phase is simulated in the same way with the same $t_{\rm coll}$ and $r_{\rm min}$ for all the progenitors. The inner boundary is kept closed and reflective for the first 100 s to provide the necessary pressure to the model while the explosion is still developing (MacFadyen et al., 2001). At this point the boundary is open which allows for the matter to fall back onto the proto-neutron star.

By changing the parameters $t_{\rm coll}$, $r_{\rm min}$ and $M_{\rm pist}$ it is possible to set up a more physical trajectory of the inner boundary. A piston placed too deep in the star would accrete too much matter while waiting for neutrinos to reverse the accretion. Similarly, a piston placed too far out would experience an inadequate peak temperature to make iron. Some experimentation on the optimal piston trajectory was made in Sukhbold et al. (2016). Here their prescription of a so-called "special trajectory" was adopted for the comparison. These setups are dependent on the neutrino driven explosions for the same progenitors, as they try to mimic the neutrino driven explosions with piston trajectories. These trajectories are defined using Lagrangian mass coordinates that mark the first mass shell in the neutrino driven explosion to be accelerated outward when the stalled shock revives. For piston, it changes the time, $t_{\rm coll}$, and the location, $r_{\rm min}$, of the bounce, and the position of the inner boundary, for the dynamics to be more similar to the neutrino-driven explosion.

It can be seen in detail on Figure 5.1, showing the radius evolution of Lagrangian mass shells with time for the neutrino-driven explosion. The red line indicates the mass enclosed in the neutrino trajectory, which is chosen as the first mass shell crossing the blue line, or the shock radius, when it starts to move outward and the shock is revived after the stagnation. On top of the mass shells structure for the neutrino driven explosion, there is a green line, indicating the corresponding inner boundary trajectory for the piston driven explosion. You can see how the green line is defined based on the neutrino trajectory; they have the same time and location of the minimum.

There is also another modification of the trajectory, which was presented in the work of Ertl et al. (2020). It is similar to the special trajectory prescription, but with the piston placed deeper, indicating the final fallback for the neutrino-driven explosion, and it is called "fallback trajectory". In the fallback trajectory prescription, as well as in the special trajectory prescription, the parameters $t_{\rm coll}$, $r_{\rm min}$ and the inner boundary are defined by neutrino driven explosion and are different for each individual progenitor. The explosion velocity is varyied in order to get the desired explosion energy. These prescriptions depend on the neutrino driven explosion, and it might be hard to reproduce the results without them.

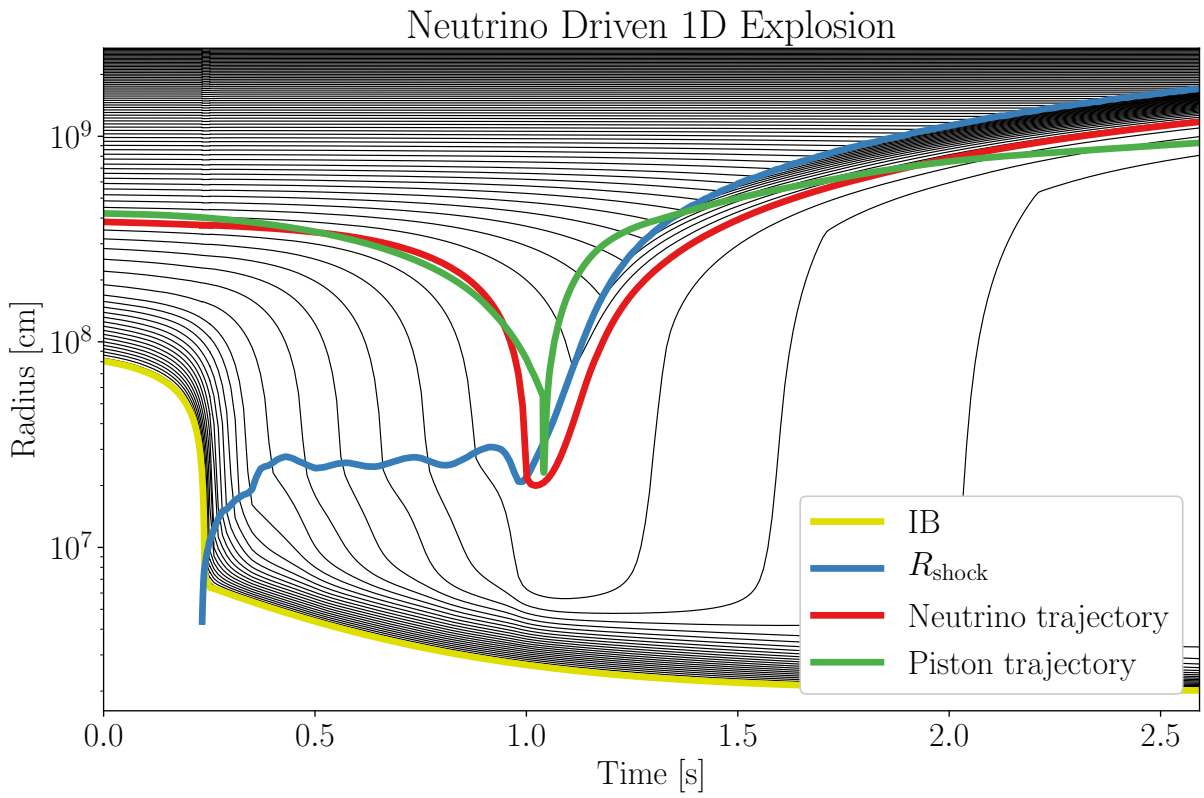


Figure 5.1: Radius evolution of Lagrangian mass shells with time for the progenitor $21M_{\odot}$, neutrino driven explosion. The result is taken from Ertl et al. (2016). The blue line corresponds to the shock radius $R_{\mathrm{shk}}$, the yellow line is the inner boundary, the thin black solid lines are the mass shells, spaced in steps of $0.025M_{\odot}$. The red line shows the chosen trajectory for the neutrino driven explosion, which marks the first mass shell to be moving outward when the shock revives, the green line represents the movement of the inner boundary of the corresponding piston driven explosion, or the piston trajectory.

In this work, we consider the classic procedure of the piston driven explosion, and the special trajectory prescription for the comparison.

### 5.2.2 Thermal Bomb

For the thermal bomb approach, the same collapse phase as in the classic piston was added to mimic a more realistic explosion. The energy is injected in $0.05M_{\odot}$ at the outer edge of the PNS. The energy growth time scales are taken to be 0.01 s and 2.0 s, as the examples of short and long explosions. The total energy injected, $E_{\mathrm{inj}}$, is varied to get the same explosion energy as for the neutrino driven explosion. The mass cut is placed at the base of the oxygen shell, which is defined, as for the piston explosions, where the dimensionless entropy, $s/k_{\mathrm{B}}$, is equal to 4. This case was considered in the present work earlier in the

context of studying the importance of the collapse phase. It corresponds to the models C$M_*$O of Chapters 3 and 4. It is used here as a reference thermal bomb case, since the collapse phase is exactly the same as in the piston explosion, and, in this way, only the method of starting the explosion after bounce is different.

For all the variations of thermal bombs, as well as piston driven explosions, a reflecting inner boundary condition is employed for the first 100 s in order to not remove pressure support from the model too early (MacFadyen et al., 2001). Then it is switched to an open boundary.

This setup was extensively discussed, and also put in the context with other thermal bombs setups, in the previous chapters, so I will not go into the details here. The new labels for the explosions are used here, t$M_*$l for the long explosion and t$M_*$s for the short explosion, and t$M_*$ for all the timescales.

### 5.2.3 Neutrino Driven Explosion

The details of the neutrino driven explosions are presented in Section 2.2 and extensively discussed in Ertl et al. (2016); Sukhbold et al. (2016). Here I want to briefly mention the calibration procedure, since the calibration in the neutrino driven explosion works a bit differently.

First, there are a couple of progenitors that are only used for the calibration to achieve a certain explosion energy and nickel mass, and they are chosen in a way that they are rather close to the observational data. Once these selected calibration models achieve the desired explosion energy and nickel mass, the parameters are fixed and can be used for a wide range of progenitors. Each calibration progenitor corresponds to one fixed set of the parameters. Thus, the outcomes will be different for all non-calibrating models, and therefore the explosion energy, nickel production and the final proto-neutron star mass are not free parameters for all the other progenitors anymore, but are calculated based on a chosen and fixed parameters of the calibration models.

A fixed combination of the parameters ($\Gamma$, $\zeta$, $R_\mathrm{c}(t)$, $n$), where $\Gamma$ is the adiabatic index, $\zeta$ is the coefficient $0 < \zeta \leq 1$ (see Equations 2.7 and 2.8), $R_\mathrm{c}$ is the core radius, and $n$ is the exponent (see Equation 2.9) defines the so-called neutrino engine, and it is the same for both of our progenitors here. The parameters are presented in Table 5.1.

The neutrino engine is calibrated based on the experimental data of SN 1987A and SN 1054-Crab. The chosen parameters correspond to the calibration model W18 from Sukhbold et al. (2016) where it is discussed in detail. This model results in a blue supergiant progenitor producing a large amount of oxygen with the enhancements in surface helium and nitrogen abundances.

Table 5.2 summarizes all the explosions that are used in this chapter, with the first letter describing the mechanism: t for thermal bomb, p for piston and n for neutrino driven explosions, and the letter after the progenitor mass for thermal bomb and piston defines the setup, t$M_*$ corresponds to the model C$M_*$O from Chapter 3, p$M_*$o corresponds to a classical piston, and p$M_*$t to the piston with the special trajectory.

Table 5.1: PNS core model parameters for the neutrino driven explosions used in this work, for the reference see Equations 2.6-2.9.

| $R_{\mathrm{c,f}}$ [km] | $\Gamma$ | $\zeta$ | $n$ |
|---|---|---|---|
| 6.0 | 3.0 | 0.65 | 3.06 |

Table 5.2: Properties of the explosions for thermal bomb, piston and neutrino driven mechanisms used in this chapter. $M_{\mathrm{ZAMS}}$ is the ZAMS mass of a progenitor, model is our indications of the explosions, $M_{\mathrm{IB}}$ is the position of the inner boundary, $M_{\mathrm{PNS}}$ is the mass of the proto-neutron star after fallback, $t_{\mathrm{coll}}$ is the collapse time, $R_{\mathrm{min}}$ is the minimum radius for the piston driven explosions, $E_{\mathrm{exp}}$ is the final explosion energy used for calibration.

| $M_{\mathrm{ZAMS}}$ $[M_\odot]$ | model | $t_{\mathrm{coll}}$ [s] | $R_{\mathrm{min}}$ [cm] | $M_{\mathrm{IB}}$ $[M_\odot]$ | $M_{\mathrm{PNS}}$ $[M_\odot]$ | $E_{\mathrm{exp}}$ $[10^{51}\,\mathrm{erg}]$ |
|---|---|---|---|---|---|---|
| 21.0 | t21.0 | 0.45 | $5.00 \cdot 10^7$ | 1.484 | | 1.026 |
| | p21.0o | 0.45 | $5.00 \cdot 10^7$ | 1.484 | 1.609 | |
| | p21.0t | 1.04 | $1.29 \cdot 10^7$ | 1.633 | 1.671 | |
| | n21.0 | | | | 1.560 | |
| 26.6 | t26.6 | 0.45 | $5.00 \cdot 10^7$ | 1.725 | | 1.072 |
| | p26.6o | 0.45 | $5.00 \cdot 10^7$ | 1.725 | 2.187 | |
| | p26.6t | 1.09 | $1.23 \cdot 10^7$ | 1.872 | 1.966 | |
| | n26.6 | | | | 1.799 | |

## 5.3 P-HOTB Results and Fallback

The dynamics of the explosions are different for the three mechanisms and can be considered in the context of the P-HOTB results. The first thing that is fundamentally different is the final remnant mass as could be seen in the upper panel of Figure 5.2 for the progenitor $M_{\mathrm{ZAMS}} = 21.0 M_\odot$ and in the lower panel of Figure 5.2 for the progenitor $M_{\mathrm{ZAMS}} = 26.6 M_\odot$. The calculations for piston driven explosions (red and magenta lines) were carried out until $10^4$ s to observe the behavior of the fallback. For the first 100 s the inner boundary is kept reflective, so the matter cannot fall back onto the PNS, but as soon as the inner boundary condition is changed and the explosion is developed, some of the matter feels the gravitational pull of the compact remnant in the center and develops negative velocities, falling through the inner boundary on the remnant and increasing its final mass. The fallback consists of the material that remains close to the piston, and is accreted on the compact remnant very quickly after the boundary is opened. On the other hand, taking a look at the thermal bomb explosions (green and olive lines), one can see that it does not affect the final remnant mass that much. The calculations for thermal bomb are presented here to demonstrate that they are not very sensitive to the fallback, and they were not carried out until very long times. For thermal bomb explosions, the fallback does not exceed $0.01 M_\odot$ for either progenitor. Neutrino driven explosion (blue lines) are presented here for a general comparison.

Moreover, for the piston driven explosion, the fallback is higher for the classical ap-

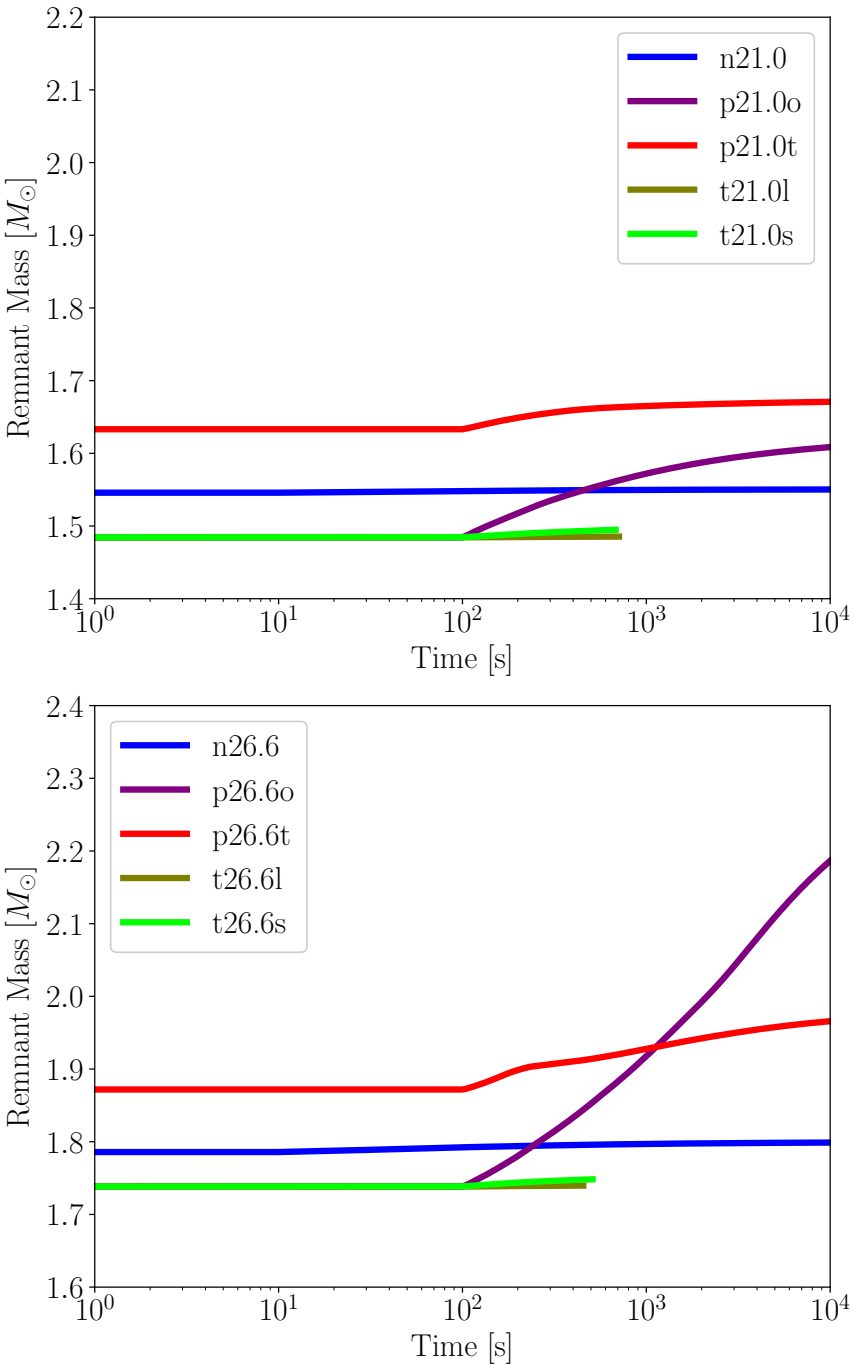


Figure 5.2: The behavior of the fallback for the explosions triggered by different mechanisms: neutrino driven n$M_*$ (blue), classical piston p$M_*$o (magenta), piston with a special trajectory p$M_*$t (red), and thermal bomb, long t$M_*$l and short t$M_*$s explosions (olive and green respectively). The results are presented for two progenitors: $21.0M_\odot$ on the upper panel and $26.6M_\odot$ on the lower panel.

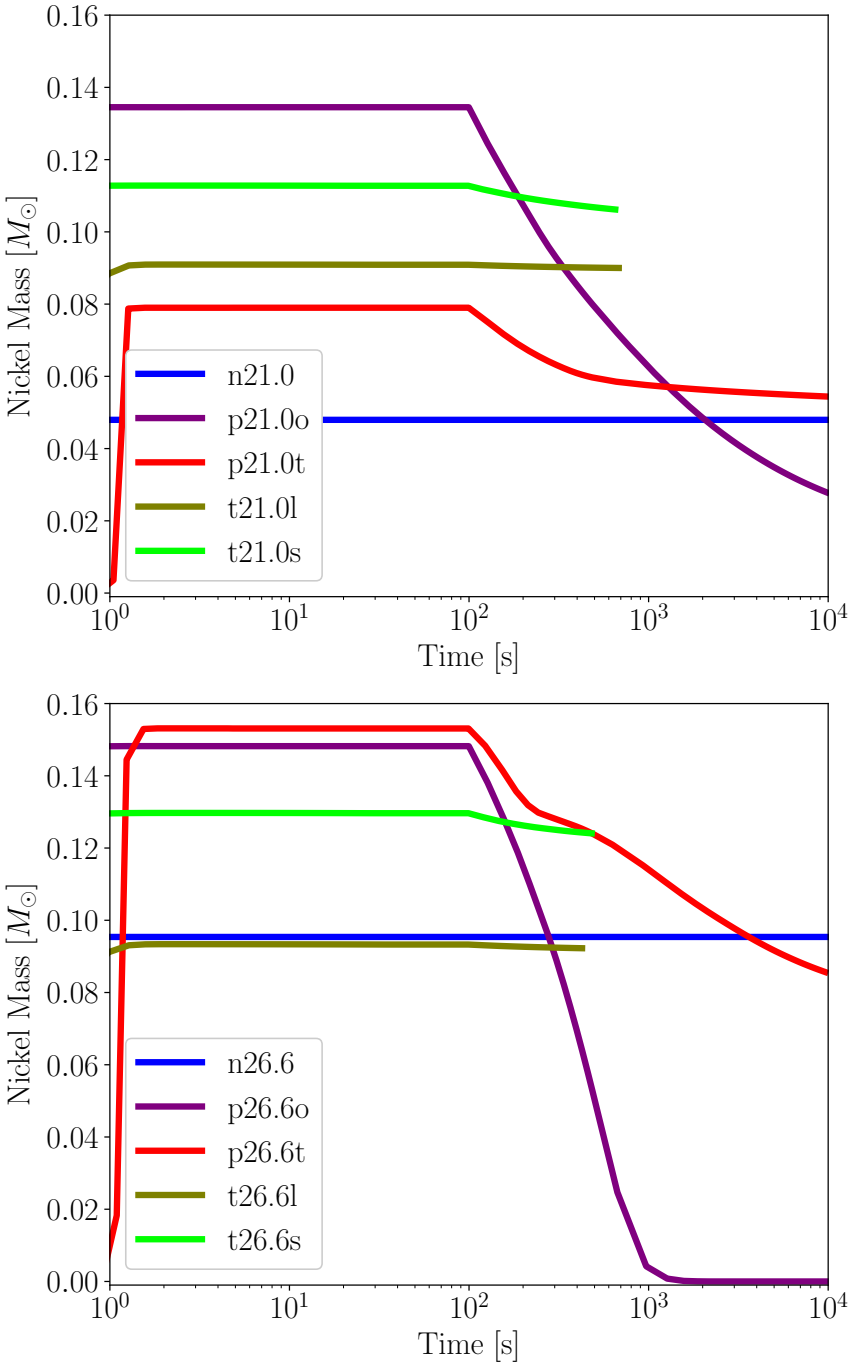


Figure 5.3: $^{56}$Ni mass as a function of time for all the mechanisms considered in this chapter: neutrino driven n$M_*$ (blue), classical piston p$M_*$o (magenta), piston with a special trajectory p$M_*$t (red), and thermal bomb, long t$M_*$l and short t$M_*$s explosions (olive and green respectively). The results are presented for two progenitors: $21.0 M_\odot$ on the upper panel and $26.6 M_\odot$ on the lower panel. The figures only reflect the results from P-HOTB simulations with a small alpha network and are intended to demonstrate how fallback affects the nickel produced during the explosion.

proach (magenta line) than it is for the special trajectory (red line), where the collapse is usually deeper, and it is happening at a later time, around $\sim 1\,\mathrm{s}$. The fallback reaches $0.129M_\odot$ for the $21.0M_\odot$ progenitor and a quite high value of $0.448M_\odot$ for the $26.6M_\odot$ progenitor for the classic piston approach as compared to $0.038M_\odot$ and $0.094M_\odot$ for the special trajectory piston respectively. It is happening due to the fact that the initial mass cut is put further out for the special trajectory, and the matter is more inclined to escape in that region. When the piston is placed further out for the special trajectory cases, the material ahead of the shock is much less dense and bound, and the shock is more efficient in pushing the material away from the boundary. Therefore, the amount of the fallback is reduced.

The fallback is also higher for the more massive progenitor, $26.6M_\odot$, which is in agreement with the results from Ugliano (2012), who also considered classic piston driven explosions. Basically here we compare the fallback for the classic piston, $0.448M_\odot$, and for the special trajectory piston, $0.094M_\odot$, for the $26.6M_\odot$ progenitor to the same mechanisms with $0.129M_\odot$ and $0.038M_\odot$ respectively for the $21.0M_\odot$ progenitor. Depending on the mechanism the difference in the fallback varies from more massive to less massive progenitors, but the general trend stays the same. The matter ahead of the shock is much more bound than in lower mass stars and the energy which is carried by the shock initiated with a piston is not enough to unbind it. Therefore, a higher amount of the matter stays close to the inner boundary and starts to come back as soon as the boundary is opened.

The effect of such matter flow has on the final nickel production can be explained by Figure 5.3 which depicts the nickel mass as a function of time. It shows that, for all mechanisms, nickel mass increases for the first 10 seconds and subsequently decreases due to the fallback. Once again, the case of the thermal bomb does not result in more than $\sim 0.007M_\odot$ change in nickel mass, which is about an 8 percent from the total mass, while piston driven explosions results in the largest difference. With reference to Figures 5.2 and 5.3, there is an obvious correlation between the final nickel mass and the amount of fallback for the piston driven explosions. This is due to the fact that nickel is being produced very close to the inner boundary and remains close to it as the explosion develops. As soon as the boundary is open, nickel falls back on the compact remnant and does not get ejected.

Nickel is much more stronger reduced for the case of the classic piston explosions as for that of the special trajectory pistons. Specifically, in the case of the $21.0M_\odot$ progenitor, the reduction in nickel is $0.107M_\odot$ and $0.025M_\odot$ for the cases of classic explosions and special trajectory, respectively. While for the case of the $26.6M_\odot$ progenitor, the reduction is $0.148M_\odot$ and $0.067M_\odot$ for the two aforementioned cases, respectively. Just as for the fallback, the nickel mass cut is put further out for the special trajectory cases. As nickel is not strongly bound, it tends to escape the PNS much more easily as compared to the classic piston case.

For the cases of classic and special trajectory pistons, the nickel mass is much more strongly reduced for the more massive progenitor, which is explained by the fallback behavior. More massive progenitors tend to have less bound matter and more energy to unbind them, thus increasing the amount of fallback. This leads to greater nickel mass reduction, as nickel tends to stay close to the boundary.

In that way, discussing the fallback and carrying the simulations out until rather late times is actually quite crucial for analyzing the piston driven explosions. The effect could be stronger or weaker depending on the progenitor and the initial conditions, but either way the effect is quite noticeable.

## 5.4 Nickel Production

To go into the details of the nickel production, we also performed the calculations with an extended reaction network from SkyNet for piston and neutrino driven explosions using the same setup that was used for thermal bomb calculations, with 262 isotopes and $T_{\rm NSE} = 9\,{\rm GK}$ (see Section 2.3 for the details). The main quantity that affects the nucleosynthesis is the peak temperature, which is presented in Figure 5.4 as function of the enclosed mass with the same color convention that was used for Figures 5.2 and 5.3. Nickel mass, which is produced during the explosion (in the first $\sim 10\,{\rm s}$), is presented in the upper panel of Figure 5.5, and it is basically defined by the areas of the complete and incomplete Si-burning on the peak temperature plots. For thermal bomb simulations in Figure 5.5, we used the results with all the timescales that were considered in the previous chapters. Since $t_{\rm inj}$ is only a parameter for the thermal bomb explosions, the nickel mass is constant over the energy deposition timescale for the rest of the mechanisms. The lower panel of this figure shows the nickel production after the fallback (at around $10^4\,{\rm s}$).

One can see that the peak temperatures for the special trajectory cases (p$M_*$t) gets as high as for the neutrino driven explosions (n$M_*$) – the red and blue lines, respectively – since the special trajectory is actually guided by the neutrino driven explosions. But from the nickel production (the dashed dotted line for the p$M_*$t cases and the dashed line for the n$M_*$ cases) we can see that the neutrino driven explosions still produce less nickel than the special trajectory, as well as less than all the rest of the mechanisms. This is because, in the case of the neutrino driven mechanism, the peak temperature is decreasing steeper with the enclosed mass which means that it is going faster through the phases of the complete and incomplete Si-burning, and does not have enough time to produce more nickel.

It is interesting to note the behavior of the classic piston (p$M_*$o) and the short explosions of the thermal bomb (t$M_*$s) (magenta and green lines respectively on the peak temperature plots). The dynamics of these two mechanisms is actually not that different. They both represent instant explosions, and the temperature decrease is quite similar which leads to the similarities in the final nickel masses (solid lines for the p$M_*$o cases and solid lines with dots for the energy deposition timescale, $\sim 0.01\,{\rm s}$ for the t$M_*$s cases). The classic piston still produces a little bit more nickel since in the short thermal bomb explosions there is an abrupt change in peak temperature decrease, as can be seen in Figure 5.4, green lines, at about $1.5 M_\odot$ of enclosed mass on the upper panel and at about $1.8 M_\odot$ on the lower panel. This abrupt change marks the end of the mass layer where the energy is deposited, so it is the result of the fact that the energy is injected over the spread in the mass.

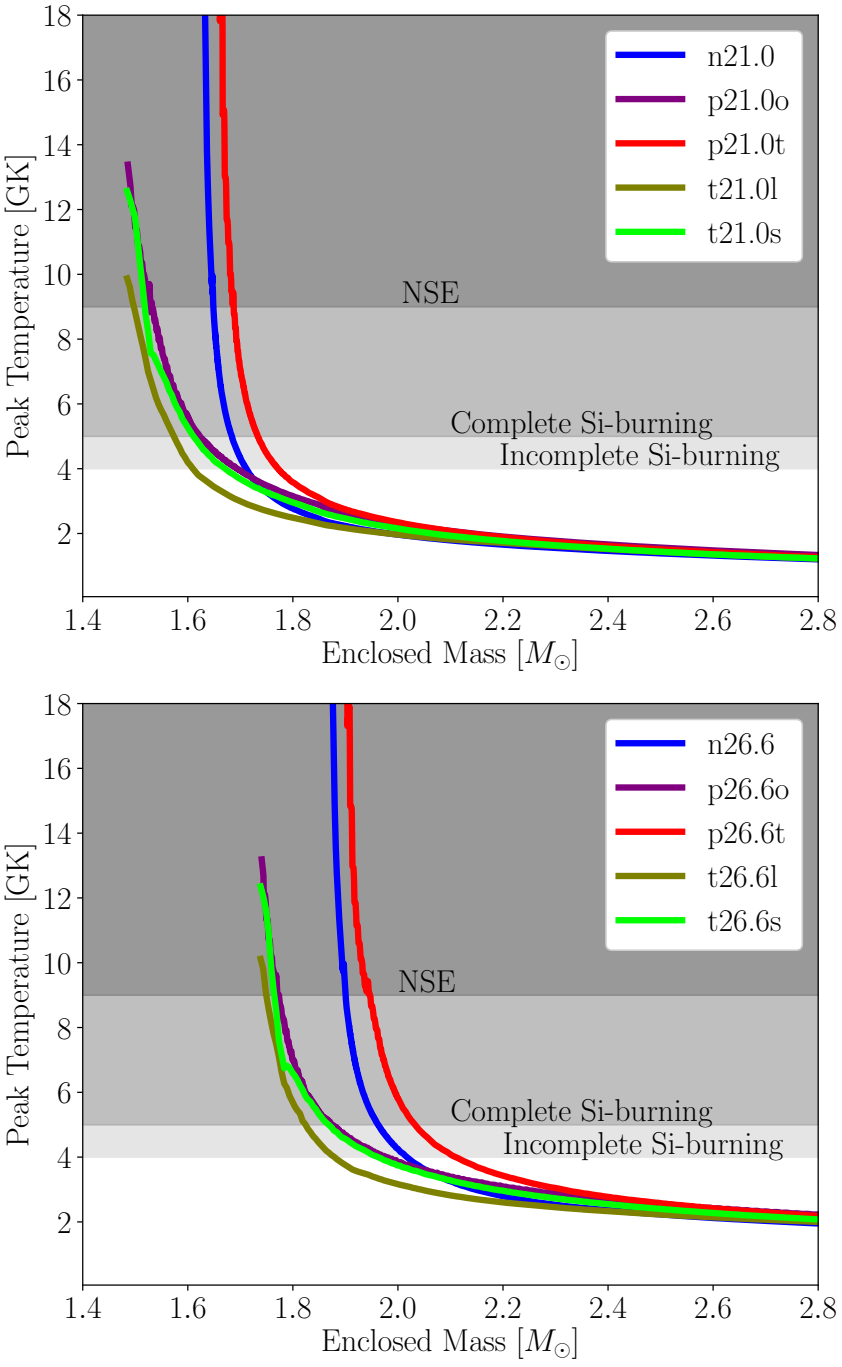


Figure 5.4: Peak temperature as a function of the enclosed mass for all the mechanisms considered in this chapter: neutrino driven n$M_*$ (blue), classical piston p$M_*$o (magenta), piston with a special trajectory p$M_*$t (red), and thermal bomb, long t$M_*$l and short t$M_*$s explosions (olive and green respectively). The results are presented for two progenitors, $21.0 M_\odot$ on the upper panel and $26.6 M_\odot$ on the lower panel. The regions of nuclear statistical equilibrium (NSE, higher than 9 GK), complete (between 5 and 9 GK) and incomplete (between 4 and 5 GK) Si-burning are marked by different shades of grey.

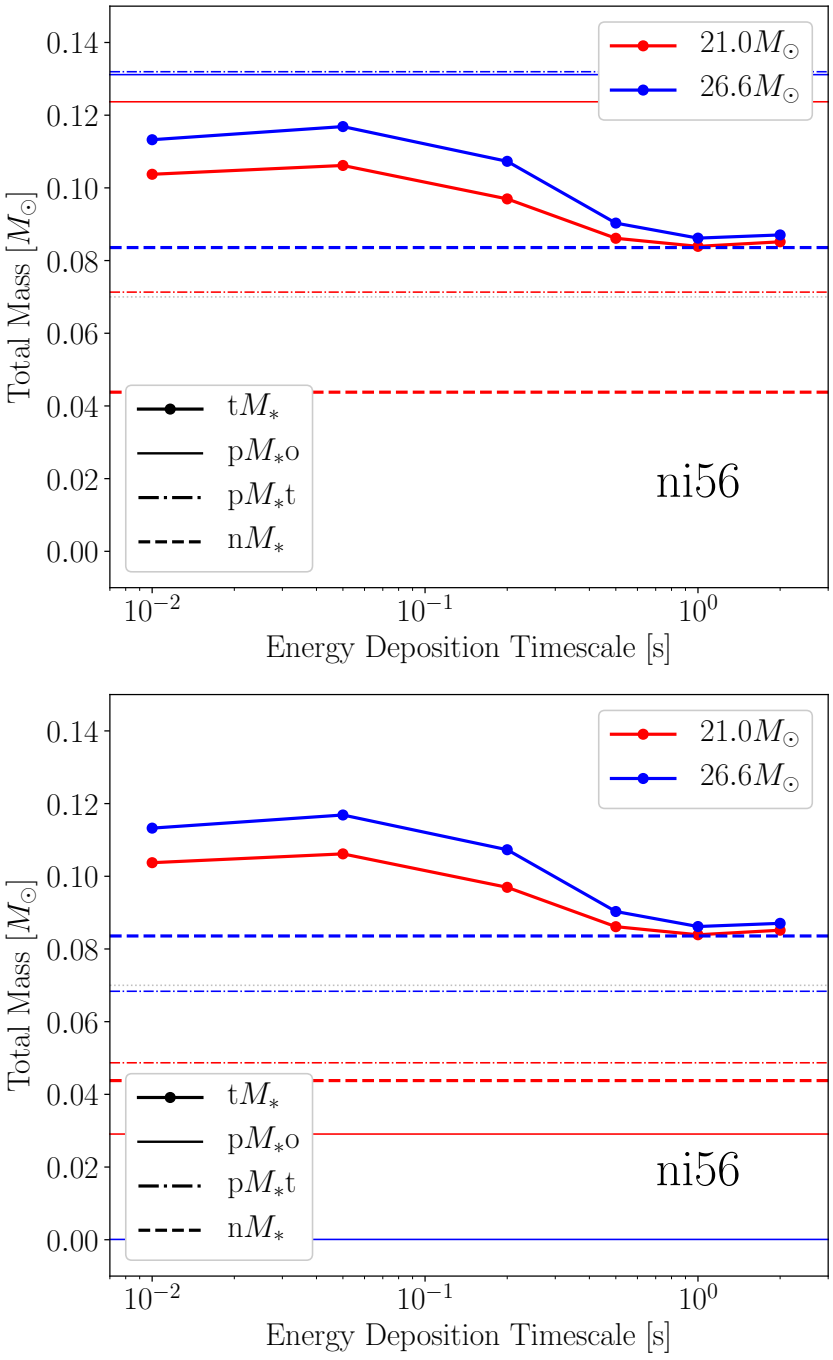


Figure 5.5: Final $^{56}$Ni mass as a function of the energy deposition timescale for all the mechanisms considered in this chapter: neutrino driven n$M_*$ (dashed), classical piston p$M_*$o (solid), piston with a special trajectory p$M_*$t (dashed dotted), and thermal bomb simulations for the energy deposition timescales from 0.01 s to 2.0 s (solid lines with dots, behavior as in Fig. 3.4, lower panel). Since the energy deposition timescale is only a parameter for the thermal bomb explosions, the values for nickel masses are constant for the rest of the mechanisms. The upper panel demonstrates how much nickel is produced during the explosion, i.e., in the first $\sim 10$ s, and the lower panel demonstrates how much nickel is left after the matter falls back onto the PNS, i.e., at around $10^4$ s. Since the fallback is only significant for the piston driven explosions, both classic and special trajectory, they are the only ones that are greatly affected by the fallback. The results are presented for two progenitors, 21.0$M_\odot$ (red) and 26.6$M_\odot$ (blue).

Then the trends for the mechanisms differ between different progenitors. For the $21.0M_{\odot}$ progenitor (upper panel in Figure 5.4 and the red lines in Figure 5.5), the special trajectory piston mechanism produces less nickel than for the long thermal bomb explosions, while, for the $26.6M_{\odot}$ progenitor (lower panel in Figure 5.4 and the blue lines in Figure 5.5) it is actually the other way around, i.e., the nickel mass for special trajectory case is much greater than that of the long thermal bomb explosions. At the same time, for the $21.0M_{\odot}$ progenitor, the neutrino driven explosion produces less nickel than for the long thermal bomb explosions. Furthermore, for the $26.6M_{\odot}$ progenitor there is an agreement on the nickel production between the neutrino driven explosion and the long thermal bomb explosion. It indicates that for these cases there are no common trends and the results would be dependent on the internal progenitor structure, but there is no clear answer which mechanism represents the neutrino driven explosions the best.

Let us now look at the lower panel of Figure 5.5 where the nickel mass is presented after taking into account the fallback for piston driven explosions. It changes the general picture. Now the highest nickel mass is produced for the thermal bomb explosions (solid lines with dots), while the amount of nickel for piston driven explosions, both classic and special trajectory cases (solid lines and dashed dotted lines respectively), is greatly reduced. For the $21.0M_{\odot}$ progenitor (red lines), the special trajectory nickel mass is the closest to the neutrino driven explosions, and, for the $26.6M_{\odot}$ progenitor, the difference between the special trajectory and the neutrino driven explosions is higher. This can be explained by the higher amount of the fallback for this progenitor (see Figure 5.2) resulting in more nickel falling back on the PNS. For the classic piston driven explosions, the final nickel mass is now much lower than for the neutrino driven explosions, and it is almost zero for the $26.6M_{\odot}$ progenitor. Taking the fallback into account, the classic piston can no longer represent the realistic values for the final nickel mass that is ejected into the interstellar medium. Based on the plot, we can conclude that the special trajectory explosions reproduce the nickel production in the neutrino driven explosions the best, which is not that surprising, since these explosions use the neutrino driven explosions for setting up the parameters. Considering that, it would not be the best mechanism for the explosion since it cannot be calculated independently of the neutrino driven explosions, and it makes this mechanism rather inflexible. On the other hand, the thermal bomb calculations provide the upper limit for the nickel mass which could be used as a constraint. This is particularly true for the long thermal bombs since no other explosions get higher nickel masses than any thermal bomb simulations with this setup.

## 5.5 Nucleosynthesis in 1D CCSN Explosions

In this section, I would like to present the results of the nucleosynthesis calculations discussed in this chapter. The calculations were performed by post-processing of the hydrodynamic simulations using different explosion mechanisms with the extended reaction network SkyNet. The main elements of interest here are the alpha elements, which are most abundant in the stars experiencing the explosions, and the iron group isotopes, which are

primarily produced during CCSNe. The final abundance distributions for different explosion mechanisms are presented in Figures 5.6-5.11.

### 5.5.1 Regions of Explosive Ne/C Burning

The isotope $^{12}$C is a product of helium burning during the evolution of a massive star. However, compared to other nuclei produced by massive stars, the yield of $^{12}$C is too small to account for its solar abundance, and lower mass stars are mostly responsible for the difference (Woosley and Weaver, 1995). The most abundant isotope of oxygen, $^{16}$O, is produced by both helium burning during stellar evolution and neon burning during the explosion.

Let us first look at the final element distribution in the piston driven explosions in Figure 5.6 for the $21.0M_{\odot}$ progenitor. For the classic piston (upper panel), the region of the explosive Ne/C burning starts at $\sim 1.78M_{\odot}$, which corresponds to $\sim 3.3\,\mathrm{GK}$ (see Table 2.1, and it is in accordance with the peak temperature plots, presented on Figure 5.4), and it ends at $\sim 2.09M_{\odot}$. For the special trajectory piston (lower panel), the region ends at the same $\sim 2.09M_{\odot}$ indicating that for both pistons the composition is pretty much unchanged for $> 2.09M_{\odot}$. But, for the special trajectory case, the Ne/C burning starts later at $\sim 1.83M_{\odot}$. It is a direct consequence of placing the mass cut further out for the special trajectory.

A slightly different situation is presented in the comparison of the short and long thermal bomb explosions (Figure 5.7) of the $21.0M_{\odot}$ progenitor. For the short explosion, similar to the classic piston driven explosions, the area of the explosive Ne/C burning is between $\sim 1.75M_{\odot}$ and $\sim 2.02M_{\odot}$, while for the long thermal bomb explosion the area is actually moved deeper in the star, spreading now from $\sim 1.66M_{\odot}$ to $\sim 1.93M_{\odot}$. Although the width of the region is very similar for both explosions, the location of the region affects the final nucleosynthesis. It will lead to higher amounts of $^{28}$Si, $^{32}$S and $^{20}$Ne, and slightly lower amounts of $^{16}$O for the longer explosion.

For the neutrino driven explosion (Figure 5.8), the area starts at $\sim 1.75M_{\odot}$ and ends $\sim 1.94M_{\odot}$. It actually starts at the same point of the star as for the short thermal bomb explosion and earlier than for both pistons, but the end of the region is in a good agreement with the long thermal bomb explosion. It would still produce slightly higher amounts of oxygen and lower amounts of neon than the long thermal bomb, and it probably is more comparable with the special trajectory piston in this region.

A large part of the oxygen-neon shell does not get hot enough for explosive nucleosynthesis and is ejected essentially unchanged. Therefore, the isotopes of O, Ne, and Mg consist of the contributions from both explosive and hydrostatic burning, and the hydrostatic burning is dominant. For all the explosions this part starts somewhere between $1.93M_{\odot}$ and $2.09M_{\odot}$, so the explosion mechanism only affects the innermost part of the star, leaving the isotopes up to silicon not significantly altered by the explosion.

For $26.6M_{\odot}$ the progenitor the trends are quite similar. For the piston driven explosions (Figure 5.9), the regions of the Ne/C burning start at $\sim 2.13M_{\odot}$ for the classic piston and at $\sim 2.23M_{\odot}$ for the special trajectory piston. So, it starts deeper in the star for the

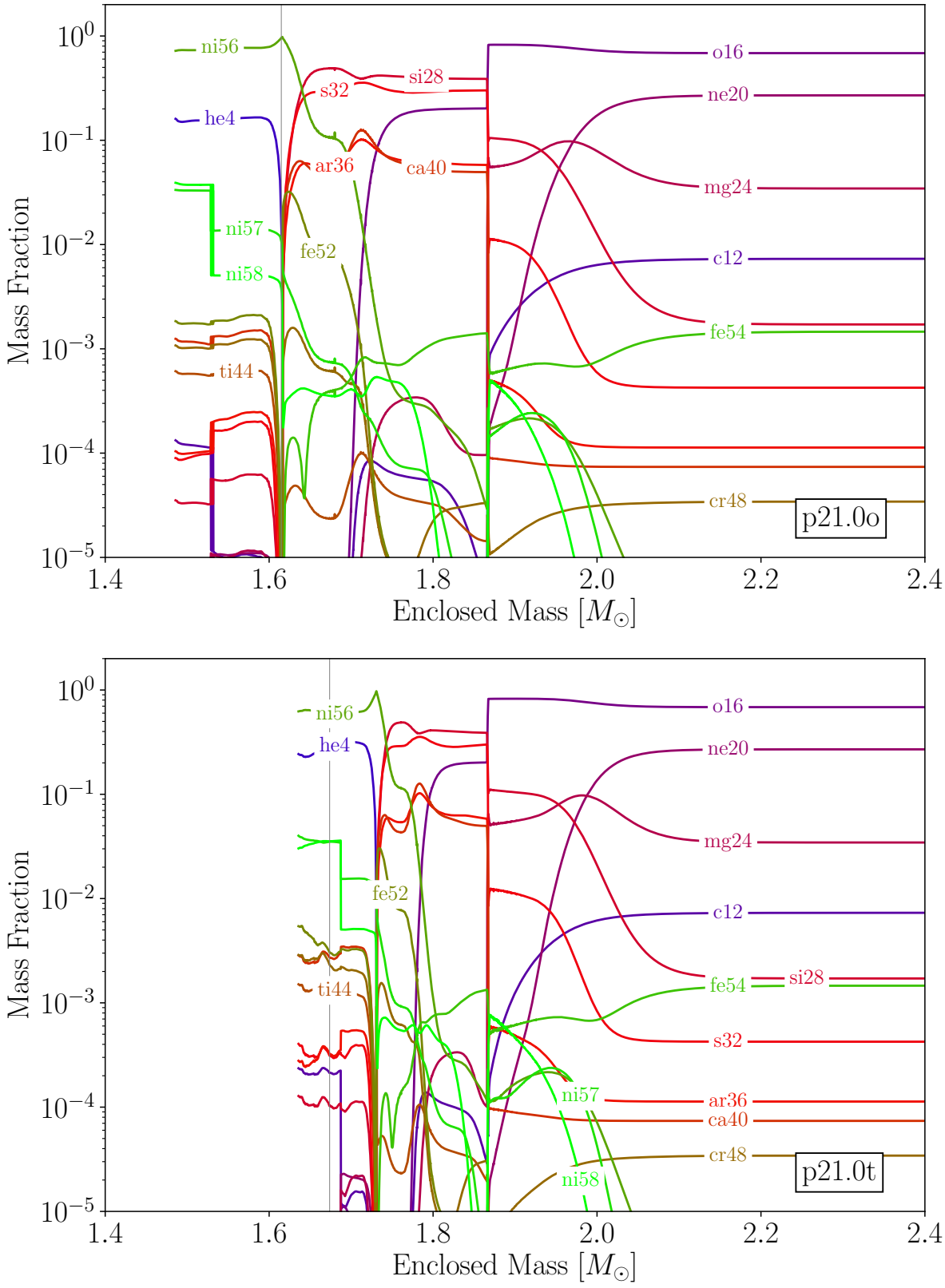


Figure 5.6: Final mass fraction distribution (at around 10 s) as a function of the enclosed mass in the inner region of the $21.0 M_\odot$ progenitor for the main alpha elements and some of the iron group isotopes. The results are presented for the piston driven explosions: classic piston p21.0o on the upper panel and special trajectory piston p21.0t on the lower panel. Vertical line marks the fallback at $\sim 10^4$ s.

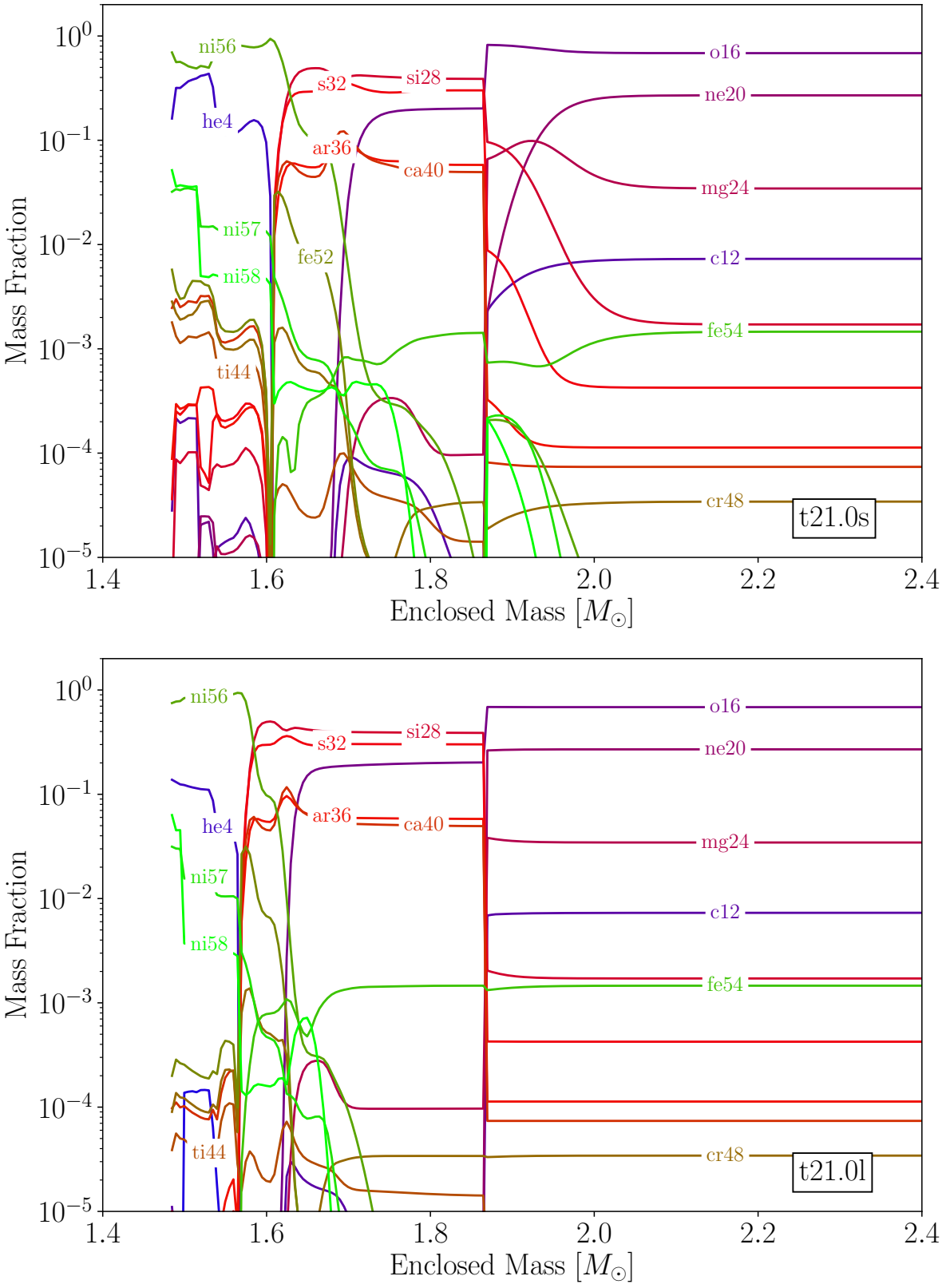


Figure 5.7: Final mass fraction distribution (at around 10 s) as a function of the enclosed mass in the inner region of the $21.0M_\odot$ progenitor for the main alpha elements and some of the iron group isotopes. The results are presented for the thermal bomb explosions: short explosion t21.0s with $t_{\rm inj} = 0.01$ s on the upper panel and long explosion t21.0l with $t_{\rm inj} = 2$ s on the lower panel.

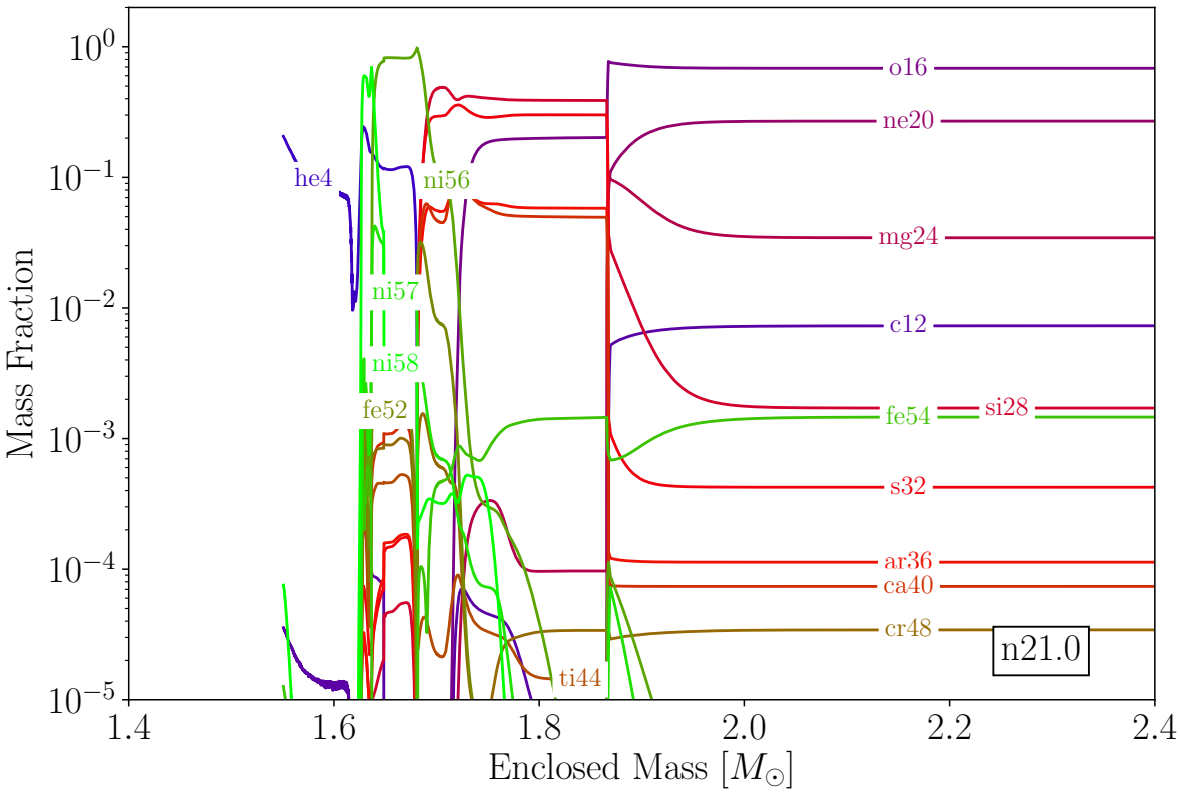


Figure 5.8: Final mass fraction distribution (at around 10 s) as a function of the enclosed mass in the inner region of the 21.0$M_\odot$ progenitor for the main alpha elements and some of the iron group isotopes. The results are presented for the neutrino driven explosions n21.0.

classic piston because of the deeper mass cut position. For the thermal bomb explosions, the region starts deeper for the long explosion, at $\sim 1.97 M_\odot$, than for the short explosion, at $\sim 2.09 M_\odot$. Again, the start of the region for the short thermal bomb explosion is in good agreement with the neutrino driven explosion, and it is deeper than for both pistons. So the comparison between the mechanisms is not very dependent on the progenitor for the starting point of the explosive Ne/C burning, but, for more massive progenitors, the regions have higher widths (now ending somewhere between $2.62 M_\odot$ and $2.95 M_\odot$ based on Figure 5.4).

### 5.5.2 Regions of O Burning

The final mass fractions of the intermediate mass elements, such as the isotopes of Si, S, Ar, Ca, include contributions from both hydrostatic and explosive burning processes. During the explosions these elements are produced mainly through explosive oxygen burning which consumes a fraction of the $^{16}$O in the progenitor star. $^{28}$Si is depleted during Si burning and created through oxygen burning, the intermediate elements like $^{32}$S and $^{36}$Ar are fully produced by oxygen burning, and the $^{40}$Ca is primarily made through the incomplete Si burning.

Oxygen burning takes place in regions where the temperature ranges from $\sim 3.3$ GK to $\sim 4$ GK (see Figure 5.4). For the piston driven explosions in the $21.0 M_\odot$ progenitor, this region is located between $1.69 M_\odot - 1.78 M_\odot$ for the classic piston. This is again deeper than for the special trajectory piston where the region lies between $1.77 M_\odot - 1.83 M_\odot$. The classic piston is again quite similar to the short thermal bomb explosion, where this region extends from $\sim 1.67 M_\odot$ to $\sim 1.75 M_\odot$, which is further out than it is for the long thermal bomb explosion ($1.61 - 1.66 M_\odot$). The region for the short explosion has a higher width which will lead to the higher amounts of $^{28}$Si. For the neutrino driven explosion, the width is the lowest, just from $\sim 1.71 M_\odot$ to $\sim 1.75 M_\odot$, with the next closest to it being the long thermal bomb explosion, and the special trajectory piston explosions. This is to be expected, since the dynamics of both the long thermal bomb explosion and the special trajectory piston explosions is designed to be more similar to the neutrino driven explosions. The results for the $26.6 M_\odot$ progenitor are again quite similar, with the oxygen burning regions being $1.98 - 2.13 M_\odot$ for the classic piston, $2.11 - 2.23 M_\odot$ for the special trajectory piston, $1.96 - 2.09 M_\odot$ for the short thermal bomb, $1.88 - 1.97 M_\odot$ for the long thermal bomb, and $2.02 - 2.09 M_\odot$ for the neutrino driven explosions.

### 5.5.3 Iron Group Elements

Explosions of massive stars contribute significantly to the iron group isotopes which are made in the inner layers of the star. The final mass fractions are therefore sensitive to the explosion details. For example, the mass cut determines how much of the silicon-oxygen shell that undergoes explosive burning is ultimately ejected. $^{54}$Fe is produced in the layers where the electron fraction $Y_e > 0.5$ and in the incomplete Si burning zone, while $^{56}$Ni and $^{57}$Ni are produced in the neutron rich layers, where alpha-rich freeze-out happens, and $^{58}$Ni

is made in Si burning zones (Curtis et al., 2019). Iron peak elements are also produced during stellar evolution, but they are mainly produced in the iron core and are not ejected by the explosion.

In the innermost region, silicon is first mostly decomposed via endothermic reactions into alpha particles, which can be seen as an increased helium mass fraction. Then, as the temperature decreases, helium starts to recombine and alpha-rich freeze-out nucleosynthesis takes place, which is exothermic (Umeda and Yoshida, 2017). Therefore, the composition of the innermost region of the complete Si burning is dominated by the isotopes of nickel, mostly $^{56}$Ni, alpha particles and some amounts of $^{57}$Ni and $^{58}$Ni.

For the piston driven explosions in the $21.0M_{\odot}$ progenitor (Figure 5.6), the regions of the complete Si burning are below $1.62M_{\odot}$ for the classic piston and below $1.73M_{\odot}$ for the special trajectory. Since the mass cut is placed deeper for the classic piston, the region of the nickel production has a larger width than for the special trajectory which leads to more nickel produced in the classic piston. Most of what was the silicon shell in the pre-explosive star is first burned to $^{56}$Ni, but, as we have seen earlier, a large portion of the produced nickel falls back to become a part of the compact remnant. The production of these isotopes in the innermost region is very sensitive to fall back and the location of the piston essentially determines the final nickel mass in the piston driven explosions. Some of the iron group elements are produced by incomplete Si burning which takes place from $1.62M_{\odot}$ to $\sim 1.69M_{\odot}$ for classic piston and from $1.73M_{\odot}$ to $\sim 1.77M_{\odot}$ for special trajectory piston. For example, $^{52}$Fe is produced in these parts of the stars, and the length of these regions defines how much of this isotope will be produced, which is higher for the classic piston.

For the thermal bomb explosions (Figure 5.7), the regions have greater extents for the short explosion (below $1.61M_{\odot}$ for complete Si burning and $1.61M_{\odot} - 1.67M_{\odot}$ for incomplete Si burning) than for the long explosion (below $1.57M_{\odot}$ for complete Si burning and $1.57M_{\odot} - 1.61M_{\odot}$ for incomplete Si burning). This indicates that there will be slightly more isotopes of nickel and iron produced in the short explosion. This statement is in agreement with Figure 5.5. The regions for the short explosion are comparable with the ones in the classic piston explosion.

For the neutrino driven explosion (Figure 5.8), the region of complete Si burning is below $1.68M_{\odot}$, which is somewhere between the classic piston and the special trajectory piston and higher than for both thermal bombs. What is unique to the neutrino driven explosion is that the formation of the nickel isotopes $^{58}$Ni and $^{57}$Ni is higher than for all the rest of the mechanisms. Thus, there are more nickel isotopes produced in total. The region of incomplete Si burning is very narrow though, only from $1.68M_{\odot}$ to $1.71M_{\odot}$, leading to less $^{28}$Si and $^{52}$Fe produced in the neutrino driven explosion.

Let us now take a look at the $26.6M_{\odot}$ progenitor. Even though the mass cut for the classic piston is placed deeper than for the special trajectory, and the regions for the complete Si burning have different locations, below $1.87M_{\odot}$ for the classic piston and below $2.03M_{\odot}$ for the special trajectory, the lengths of the regions are quite comparable which results in the similar amount of nickel produced in these explosions (Figure 5.9). This conclusion is in agreement with the upper panel of Figure 5.5. Incomplete Si burning is

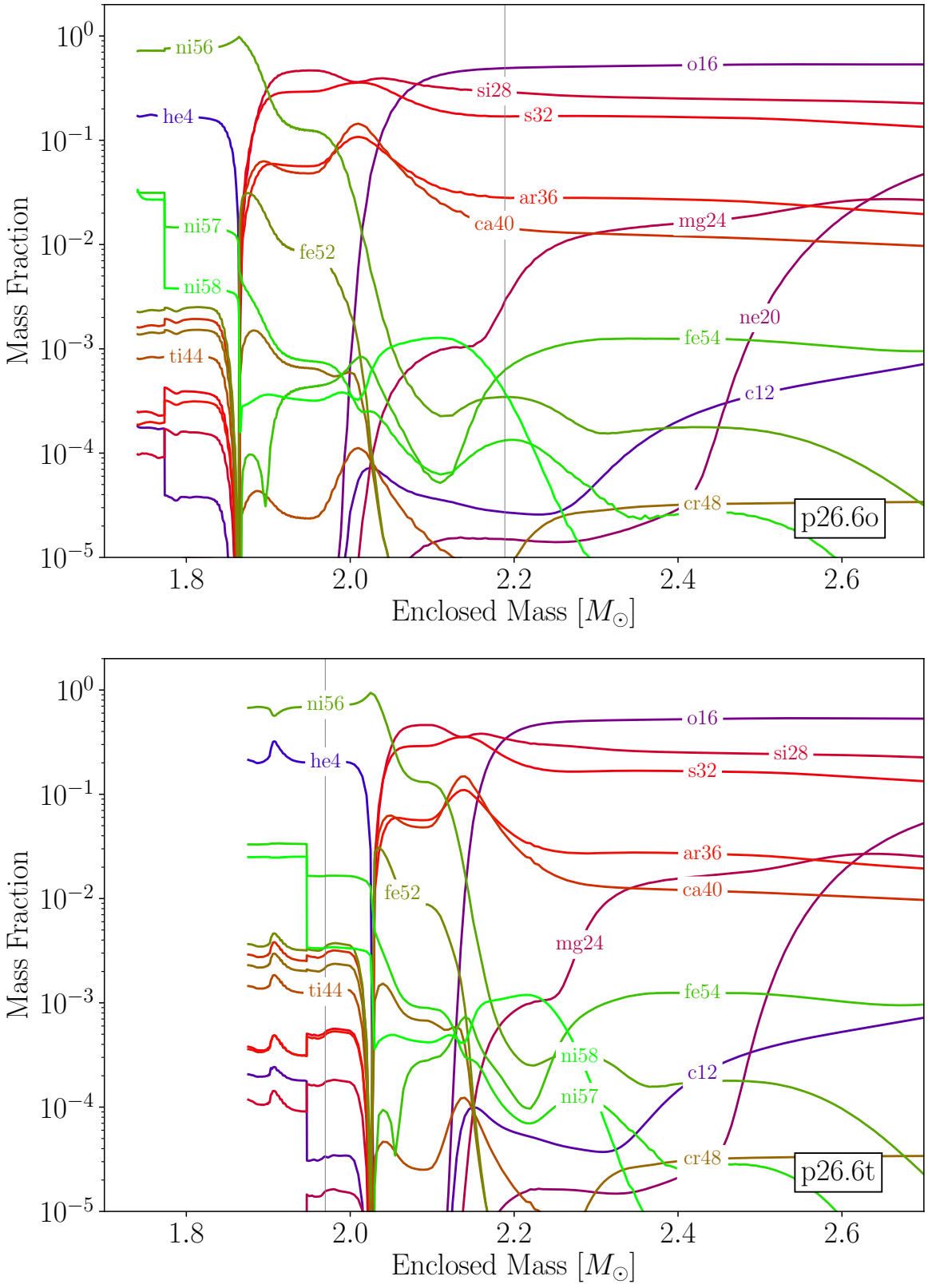


Figure 5.9: Final mass fraction distribution (at around 10 s) as a function of the enclosed mass in the inner region of the $26.6 M_\odot$ progenitor for the main alpha elements and some of the iron group isotopes. The results are presented for the piston driven explosions: classic piston p26.6o on the upper panel and special trajectory piston p26.6t on the lower panel. Vertical line marks the fallback at $\sim 10^4$ s.

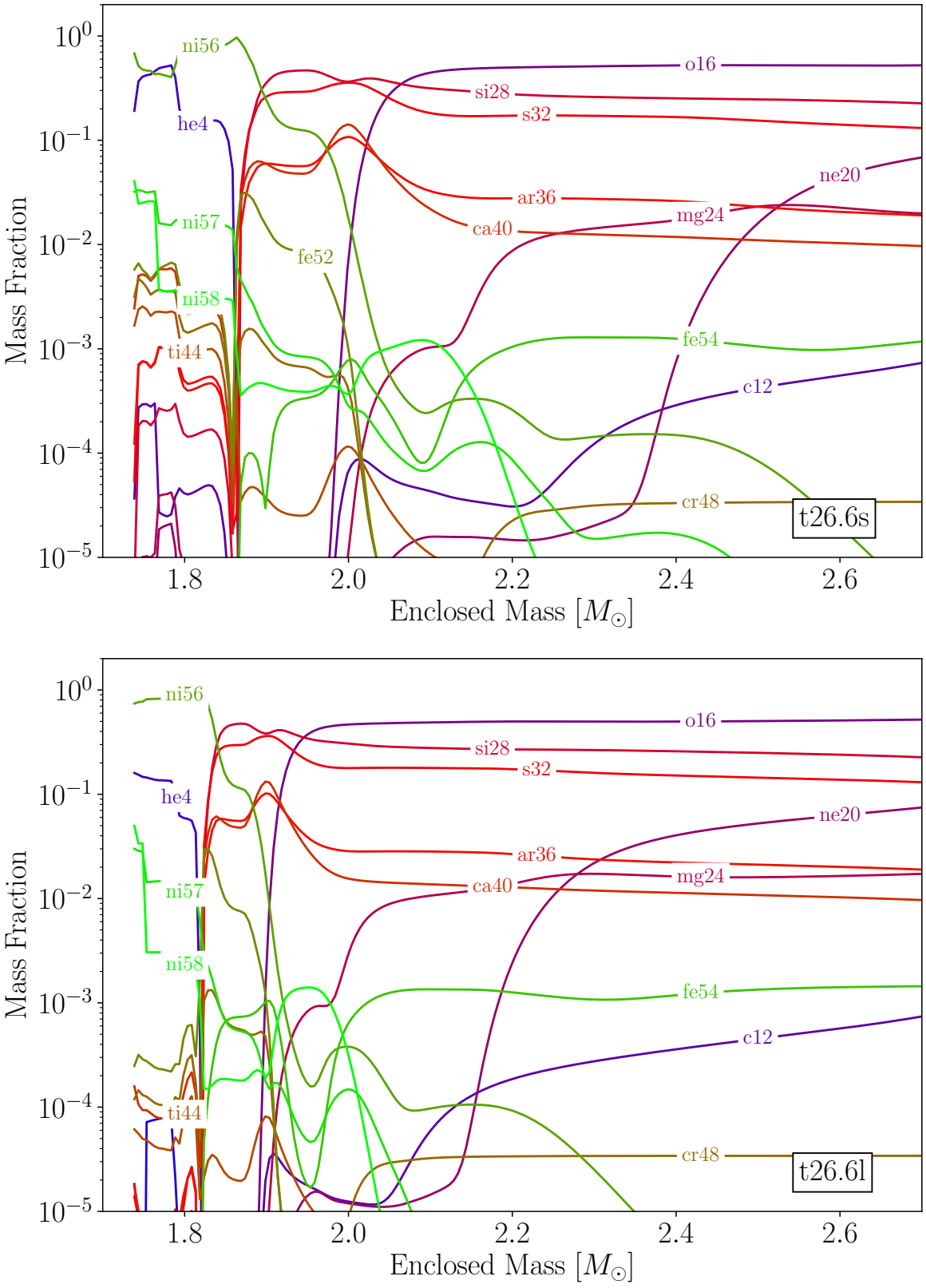


Figure 5.10: Final mass fraction distribution (at around 10 s) as a function of the enclosed mass in the inner region of the $26.6M_\odot$ progenitor for the main alpha elements and some of the iron group isotopes. The results are presented for the thermal bomb explosions: short explosion t26.6s with $t_{\rm inj} = 0.01$ s on the upper panel and long explosion t26.6l with $t_{\rm inj} = 2$ s on the lower panel.

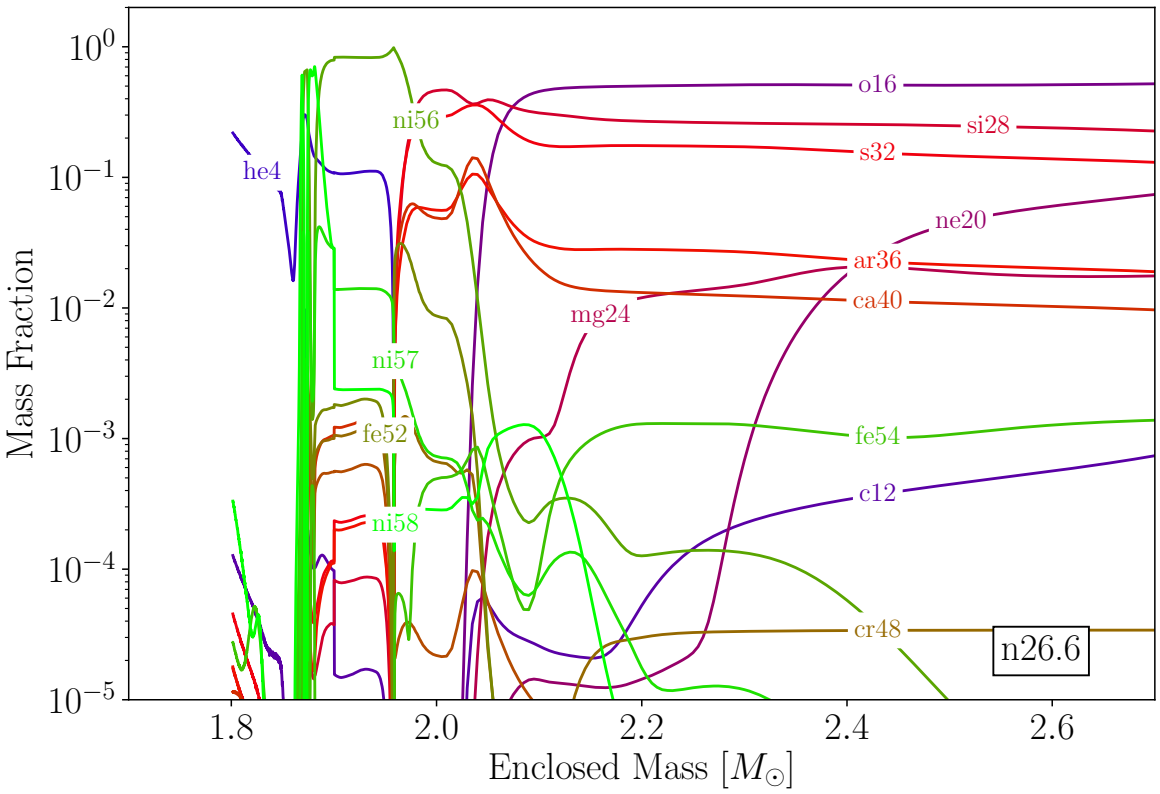


Figure 5.11: Final mass fraction distribution (at around 10 s) as a function of the enclosed mass in the inner region of the 26.6$M_\odot$ progenitor for the main alpha elements and some of the iron group isotopes. The results are presented for the neutrino driven explosions n26.6.

happening from $1.87M_\odot$ to $1.98M_\odot$ for the classic piston and from $2.03M_\odot$ to $2.11M_\odot$ for the special trajectory piston, so the region is wider for the classic piston leading to higher production of $^{28}$Si and $^{52}$Fe as well as for the $21.0M_\odot$ progenitor.

The thermal bomb explosions for the $26.6M_\odot$ progenitor (Figure 5.10) demonstrate very similar behavior as for the $21.0M_\odot$ progenitor. Namely, the region of complete Si burning is higher for the short explosion (below $1.87M_\odot$) than it is for the long explosion (below $1.82M_\odot$) causing slightly more nickel to be produced in the short explosion.

In the neutrino driven explosion of the $26.6M_\odot$ progenitor (Figure 5.11) one can see that the region of $^{56}$Ni production is wider than for the $21.0M_\odot$ progenitor, since the complete Si burning now has a higher width (below $1.96M_\odot$). There is also more other isotopes of nickel produced than for other explosion mechanisms. The area of incomplete Si burning is from $1.96M_\odot$ to $\sim 2.02M_\odot$, being again smaller than for other mechanisms, but comparable with the long thermal bomb explosion (where it is from $1.82M_\odot$ to $1.88M_\odot$). It will result in less production of the $^{28}$Si and $^{52}$Fe isotopes in the neutrino driven and long thermal bomb explosions.

Overall, one can see that there are some similarities between the isotopes produced in the explosion in the classic piston and in the short thermal bomb explosions, but the final result will be altered by the fallback in the piston driven explosions. There is also some resemblance between the long thermal bomb and the neutrino driven explosions, but mostly the picture of the nucleosynthesis in the neutrino driven explosion is actually quite different than in all the other mechanisms.

## 5.6 Conclusions

In this chapter, we looked at the comparison between different explosion mechanisms in spherical symmetry for two progenitors, $21.0M_\odot$ and $26.6M_\odot$. The mechanisms considered here are two variations of the piston driven explosions (classic piston and special trajectory piston), two variations of the thermal bomb explosions (short $t_{\rm inj} = 0.01\,$s and long $t_{\rm inj} = 2.0\,$s explosions), and we compared them to the neutrino driven explosions. The summary of the explosions used in this chapter are presented in Table 5.2.

In Section 5.3 we looked at the results of the hydrodynamic simulations with P-HOTB and analyzed the general dynamics of the explosions. Specifically the amount of the fallback for all the cases and how it affects the final nickel ejected into the interstellar medium was investigated. The effect is not very noticeable for the thermal bomb and the neutrino driven explosions, but, in the case of the piston driven explosions, there is a lot of material falling back onto the proto-neutron star after 100 s, when the inner boundary condition is changed from a reflective to an open boundary. As soon as the inner boundary is open, the matter close to the piston starts to feel the gravitational pull of the compact remnant in the center. The amount of fallback is generally higher for the classic piston approach than for the special trajectory piston because the piston is generally located further out for the special trajectory, and it is easier for the matter in this region to escape since it is much less dense and bound. We also observed that the amount of fallback is generally

higher for a more massive progenitor. The reason for this is that the matter ahead of the shock is more bound in more massive progenitors, and the energy carried by the shock is no longer enough to unbind it.

Since the iron group nuclei are mainly produced in the innermost region of the star, the fallback is greatly affecting the final nickel mass that will be ejected. The effect is the highest for the classic piston explosions because the amount of the fallback is higher in these cases. For example, in the $26.6M_{\odot}$ progenitor, the amount of $^{56}$Ni is reduced to almost zero after the fallback which is not comparable to the thermal bomb or neutrino driven explosions.

In Section 5.4 the final $^{56}$Ni production after the detailed calculations of nucleosynthesis with an extended reaction network (262 isotopes) was analyzed for different mechanisms. We looked at the nickel that was produced during the explosion (in the first $\sim 10\,\mathrm{s}$) and what was left after fallback in the piston driven explosions (at around $10^4\,\mathrm{s}$). Piston driven explosions tend to overproduce nickel during the explosion which is compensated by the late fallback when the nickel is falling back on the proto-neutron star. This leaves very little nickel to be ejected. The classic piston and the short thermal bomb explosions produce comparable amounts of nickel during the explosion for both progenitors. The neutrino driven explosions produce less nickel than any of the thermal bombs, and, since the long thermal bombs tend to produce slightly less nickel than the short ones, the long thermal bomb cases could provide an upper limit on the nickel produced during the explosion.

After the fallback is taken into account, the classic piston can no longer represent the realistic values for the final nickel mass that is ejected into the interstellar medium. On the other hand, the special trajectory explosions reproduce the nickel production in the neutrino driven explosions the best, which is not that surprising, since these explosions use the neutrino driven explosions as a starting point. However, it would not be the best mechanism for the explosion since it cannot be calculated independently of the neutrino driven explosions, and it makes this mechanism rather inflexible.

Detailed nucleosynthesis calculations for alpha elements and for the iron group nuclei were considered in Section 5.5. We considered the regions of explosive Ne/C burning, explosive O burning, incomplete and complete Si burning for all the mechanisms and for both progenitors $21.0M_{\odot}$ and $26.6M_{\odot}$. While for the $21.0M_{\odot}$ progenitor the special trajectory piston is clearly producing less nickel than the classic piston because the mass cut is deeper for the classic piston, this is not the case for the $26.6M_{\odot}$ progenitor which produces almost the same amounts of nickel for both pistons. Generally, the results for the different mechanisms for the regions of the explosive Ne/C burning are not very dependent on the progenitor for the starting point of the region, but they are wider for more massive progenitors.

For the regions of the oxygen burning, we saw that the width of the region for the long thermal bomb and the special trajectory piston explosions are the closest to the neutrino driven explosion, which is not surprising, since they are both modeled to have a similar dynamics as in the neutrino driven explosion. The results for this region are again not very dependent on the progenitor mass.

Iron group nuclei are basically produced in the innermost regions of a star where in-

complete and complete Si burning processes are taking place. These are the areas that will be most affected by the explosion mechanism. Here the results are also slightly affected by a progenitor. For example, in the $21.0M_{\odot}$ progenitor there is a difference in the nickel production for the piston explosions, giving more nickel in the classic piston, because of the deeper mass cut in this case, while, for the $26.6M_{\odot}$ progenitor, the amount of nickel is quite comparable. Although the areas of incomplete Si burning are getting smaller for the special trajectory piston in the $26.6M_{\odot}$ progenitor, this is mainly affecting the production of $^{28}$Si and $^{52}$Fe. The sensitivity to the progenitor is not that visible in the thermal bomb explosions though.

Moreover, we saw again that there are general similarities for all the isotopes between the short thermal bomb and the classic piston explosions, but the final composition of the ejecta for the piston will be changed due to the fallback. The neutrino driven explosions show the smallest regions of incomplete and complete Si burning but are comparable with the long thermal bomb explosions. In general, the nucleosynthesis for the neutrino driven explosions in the innermost region is actually quite different from all the rest of the mechanisms, producing more isotopes of nickel $^{58}$Ni and $^{57}$Ni and less $^{28}$Si and $^{52}$Fe due to neutrino-induced reactions.

# Chapter 6

# Summary and Conclusions

Core collapse supernovae (CCSNe) are one of the most important sources of heavy elements in the Universe. During the explosion the density and temperature of a star are changing drastically, inducing synthesis of new elements. So the CCSNe serve both to distribute the elements produced in massive stars during their evolution and to synthesize and distribute new elements.

CCSNe have long been studied in spherical symmetry, as well as with 2 and 3 dimensional modeling. Multidimensional modeling is very important for understanding the underlying physics of the phenomenon and to look into the details of the contributing processes. But these simulations are too computationally expensive to allow for long term investigations. This is where one dimensional simulations come into play. They are able to provide the calculations over large sets of progenitors and parameters until late times. These models are very important for simulating the contribution of CCSN in galactic chemical evolution and for looking at general trends in the element production. Therefore, they are still widely used by the community.

A massive star does not explode by itself in spherical symmetry though, and the explosion has to be induced artificially. There are several well-known methods to do that. The most common approaches are the thermal bomb and the piston driven mechanisms, where the explosion is triggered by adding an extra thermal or kinetic energy respectively. There are also more sophisticated methods, including neutrinos, that are aiming at mimicking some of the physics of 3D CCSN in spherical symmetry.

In this thesis I am presenting the overview of two different 1D explosion mechanisms, thermal bomb and piston, and their comparison to the neutrino-driven explosions. Thermal bomb and piston driven explosions are rather simple mechanisms that are implemented in several codes such as MESA and SNEC. They are flexible in the parameters space and their usage is made very convenient. Therefore, it is important to understand the limitations of the mechanisms and to have a feeling for how changing certain parameters will change the dynamics of the explosion and the final results. I compare the results of these two mechanisms to the neutrino driven explosions, a more realistic mechanism. Our calculations in this work are presented for four progenitors: 12.3, 19.7, 21.0 and $26.6 M_{\odot}$. However, the $12.3 M_{\odot}$ progenitor was eliminated in most of the calculations based on the

results for this progenitor which is not relevant for the present work.

As an indicator for the comparison, I use the final mass of $^{56}$Ni produced in the explosion. It is a good diagnostic tool for the explosions mechanisms, since it can be obtained from light curve modeling and compared to the calculated value. The nickel mass is obtained after post-processing with the extended reaction network SkyNet to get more realistic values. Future plans for this project include taking a look at other elements produced in the explosion.

In Chapter 3 we consider the thermal bomb explosions with and without collapse phase. Thermal bomb is a widely used explosion mechanism, and, due to its flexibility, the dynamics of the explosion can also be controlled by parameters. The results are presented in comparison with the work SM19, where the uncollapsed explosions were used. On top of that, we simulated the explosions with a collapse phase while keeping the rest of the parameters fixed. Simulating the explosion with an uncollapsed thermal bomb leads to the clear dependence of the final nickel mass on the energy deposition timescale, namely the slower explosions tend to suppress the nickel production. This in fact contradicts the results of 3D simulations. Simulating a thermal bomb with a collapse phase, however, shows that this dependence was a clear consequence of not collapsing the core because the nickel mass is actually almost flat in these models. To confirm that it was a consequence of not collapsing the star, we also shifted the inner boundary further out to see whether the behavior stays the same. Our new inner boundary is now located at the base of oxygen shell, where the dimensionless entropy $s/k_{\mathrm{B}} = 4$, and in this case the result also has very little sensitivity to the energy deposition timescale.

In Chapter 4 we continued studying the thermal bomb explosion mechanism to see what else the results will be sensitive to. We drastically changed the mass layer of the energy deposition and saw that, in this case, the results still show the same behavior and only differ a bit in numbers. We also tried to inject the energy in the fixed volume instead of the fixed mass of the progenitor, and we saw that the behavior is still quite similar. These models demonstrate very little sensitivity to the energy deposition timescale, although there is systematically a bit less nickel produced in the fixed volume of the energy deposition. Moreover, we considered changing the collapse phase by reducing the minimum radius for the collapse. The minimum radius was changed from the default value of 500 km, that was guided by the classic piston driven explosions, to the new value of 150 km, which is very close to the radial location of the neutrino heating layer in neutrino driven explosions. Here we saw that, for longer heating timescales and fixed mass energy deposition, there is a new phenomenon in the extreme collapse models; namely, that the final nickel mass is higher for longer timescales. It means that slower explosions tend to overproduce nickel which is opposite to the behavior of the uncollapsed models. We also summarized the recommendations for the thermal bomb users:

- Including a collapse phase before the energy injection is crucial for getting a more realistic picture. Collapse is controlled by the time of bounce, $t_{\mathrm{coll}}$, and the minimum radius, $R_{\mathrm{min}}$. For the minimum radius, the value of 500 km is sufficient.

- The inner boundary should be chosen near the $s/k_{\mathrm{B}} = 4$ location, instead of putting

it close to the edge of the iron core.

- For this reason, $^{56}$Ni will be efficiently produced in the energy-injection layer, and the matter in this layer should be included in the ejecta if it becomes gravitationally unbound by the explosion.

- For the deposition of the energy, it is easier to use a fixed mass layer instead of the fixed volume deposition, and the results showed that neither choice leads to major differences. The value of the mass layer $\Delta M$ did not seem to greatly affect the final results.

- With these recommendations, the final mass of $^{56}$Ni is rather insensitive to the energy deposition timescale.

Of course, these recommendations are based on a small set of simulations for only three progenitors and a defined explosion energy of $10^{51}$ erg in all of our thermal-bomb calculations. A wider exploration is desirable to test the more general reliability of our proposed parameter settings. Beyond the prescriptions listed above, the value of the explosion energy is another crucial input into the thermal-bomb modelling. Its specification has to be guided by our first-principle understanding of the physics of the CCSN mechanism in stars of different masses.

In Chapter 5 the comparison of three explosion mechanisms, thermal bomb, piston and neutrino driven, is presented. For piston driven explosions, we consider two variations, the classic piston and the special trajectory piston. First, we underline the importance of considering the fallback for the piston driven explosions. The iron group nuclei are mainly produced in the innermost region of the star. Therefore, the fallback is greatly affecting the final nickel mass that will be ejected. We also compared the nickel that was produced during the explosion to what was left after the fallback in the piston driven explosions. Piston driven explosions tend to overproduce nickel during the explosion which is compensated by the late fallback. The classic piston and short thermal bomb explosions produce comparable amounts of nickel during the explosion. The neutrino driven explosions produce less nickel than any of the thermal bombs, and since the long thermal bombs tend to produce slightly less nickel than the short ones, the long thermal bomb could provide an upper limit on the nickel produced during the explosion.

We also looked at the detailed nucleosynthesis calculations for all the mechanisms for alpha elements and for the iron group nuclei. We saw that there are general similarities for all the isotopes between the short thermal bomb and the classic piston explosions, but the final composition of the ejecta for piston will be changed due to the fallback. The regions of incomplete and complete Si burning are the smallest for the neutrino driven explosions, but they are comparable with those of the long thermal bomb explosions. Moreover, more isotopes of the iron group nuclei are produced in the innermost regions for the neutrino driven explosions making the nucleosynthesis for these mechanisms quite different from the rest of the mechanisms.

Simulations of the CCSN explosions in spherical symmetry are quite important for understanding the origin of the elements in the Universe. When using one dimensional artificial explosion mechanisms, it is very important to understand the limitations of the models because it could lead to misinterpreting the results of the simulations.

# Appendix A

# List of Abbreviations

| | |
|---|---|
| 1D | one dimensional (spherically symmetric) |
| 2D | two dimensional (axially symmetric) |
| 3D | three dimensional (full geometry) |
| CCSN(e) | core collapse supernova(e) |
| IBED | inner boundary of the energy deposition |
| LMC | Large Magellanic Cloud |
| NSE | nuclear statistical equilibrium |
| OBED | outer boundary of the energy deposition |
| PNS | proto-neutron star |
| SM19 | the work by Sawada and Maeda (2019) |
| SN(e) | supernova(e) |
| ZAMS | zero age main sequence mass |

# Appendix B

# Model Indicators for Thermal Bomb Explosions

The standard model name for Chapter 3 and Chapter 4 looks like this: U$M_*$OM, where $M_*$ is the placeholder for the mass, $M_{\mathrm{ZAMS}}$, of the progenitor, $M_* = 12.3, 19.7, 21.0, 26.6 M_\odot$.

- The first letter in the model name indicates how the collapse phase is treated, with the following options and their explanations:

  | | |
  |---|---|
  | U | uncollapsed models, or models with no collapse phase |
  | C | collapsed models, characterized by $t_{\mathrm{coll}} = 0.45\,\mathrm{s}$ and $r_{\mathrm{min}} = 5.0 \cdot 10^7\,\mathrm{cm}$ |
  | xC | extremely collapsed models, characterized by $t_{\mathrm{coll}} = 0.45\,\mathrm{s}$ and $r_{\mathrm{min}} = 1.5 \cdot 10^7\,\mathrm{cm}$ |

- The letter after the placeholder $M_*$ in the model name indicates the initial position of the inner boundary:

  | | |
  |---|---|
  | D | deep inner grid boundary at the progenitor's location where $Y_e = 0.48$ |
  | O | the inner grid boundary located farther out, where $s/k_{\mathrm{B}} = 4$ |

- The next letter indicates how the energy was deposited in the model:

  | | |
  |---|---|
  | *no letter* | the standard case with the energy deposited into a fixed mass $\Delta M = 0.05\,M_\odot$ |
  | M or M' | the energy deposited into the changed fixed mass, compared to the standard case |
  | V | the energy deposited into a fixed volume $\Delta V$ instead of a fixed mass $\Delta M$ |

# Appendix C

# Dynamics of the explosions for the $19.7M_{\odot}$ and $26.6M_{\odot}$ progenitors

Additional mass shell plots for the progenitors $19.7M_{\odot}$ and $26.6M_{\odot}$ are presented in this appendix. The results for Figures C.1 and C.2 are in agreement with the results for the $21.0M_{\odot}$ progenitor in Figure 3.6, discussed in detail in Chapter 3. The upper panels represent the dynamics for the uncollapsed thermal bomb explosions with the deep mass cut, the middle panels show the explosions for collapsed thermal bomb with the deep mass cut, and lower panels represent the results for the collapsed models with the mass cut, placed at the base of the oxygen shell. It is possible to see that the peak temperature does not get as high for uncollapsed models as for the collapsed ones, affecting also the nickel production (see Figure 3.4). For the $19.7M_{\odot}$ progenitor in the middle panel of Figure C.1 we see the formation of the second wave, as well as for the $21.0M_{\odot}$ progenitor in Figure 3.6, and for the $26.6M_{\odot}$ progenitor in Figure C.2, which however does not lead to the increased nickel production for the $19.7M_{\odot}$ progenitor (see Figure 3.4, middle panel). It happens due to the structure of the $19.7M_{\odot}$ progenitor, which underproduces nickel for all the timescales of the explosions. It could also be seen, that even though there is the second wave formed in this case as well, the peak temperatures of this wave are actually lower than the same temperatures for the $21.0M_{\odot}$ and $26.6M_{\odot}$ progenitors, which ultimately leads to the increased nickel produced for these progenitors. In the lower panels of Figure C.1 and Figure C.2 it is clearly seen that the density between IBED and OBED for the $19.7M_{\odot}$ progenitor is much lower than for $26.6M_{\odot}$, which leads to nickel being very inefficiently produced in the case of $19.7M_{\odot}$ progenitor.

The results, discussed in Chapter 4, that are equivalent to Figure 4.3, are presented in Figures C.3 and C.4 for the $19.7M_{\odot}$ and $26.6M_{\odot}$ progenitors. The main difference that one can see, is that the density for the $19.7M_{\odot}$ progenitor is significantly lower, which again leads to the suppressed nickel produced for this progenitor (see Figure 4.2). Other than that, it is also visible, that the models with the extreme collapse (upper and lower right panels on Figures C.3 and C.4) reach higher peak temperatures, since the extreme collapse moves all the material to higher densities, which heats it up. Moreover, in the lower right panel of Figure C.4 the first mass shell above IBED does not go very far away from the

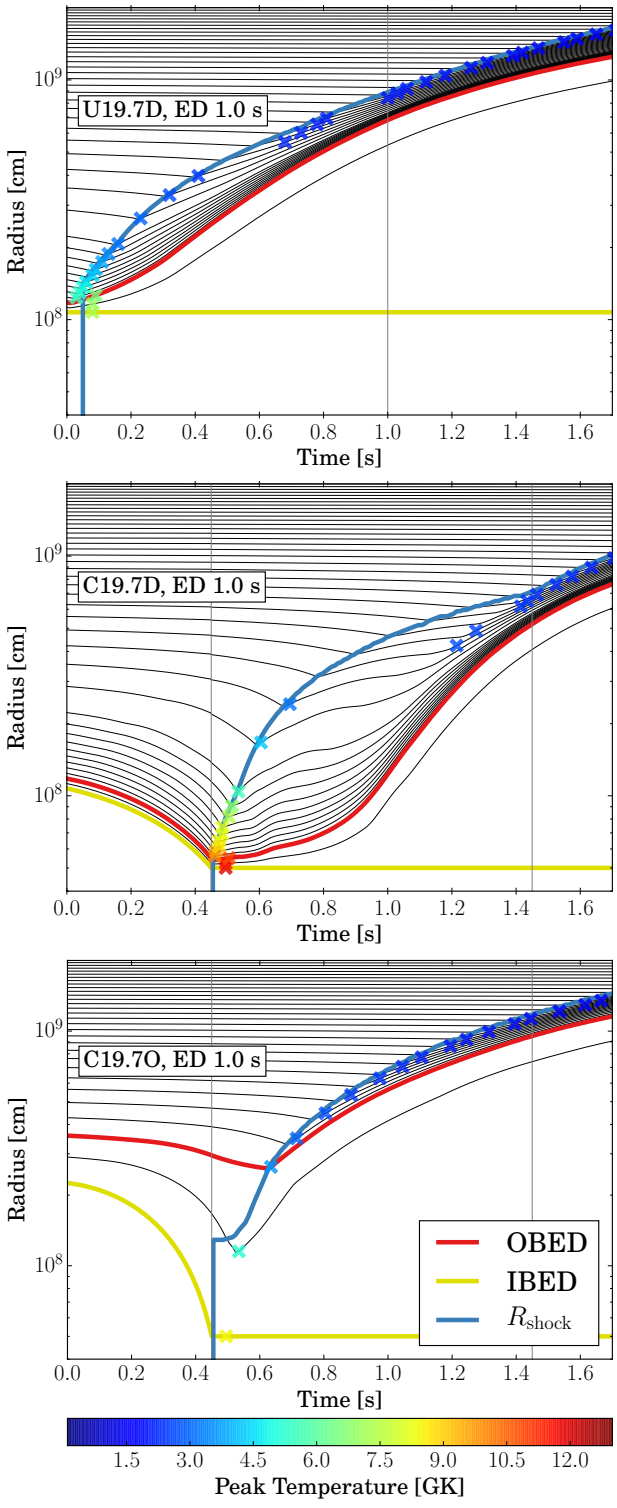


Figure C.1: Radius evolution of Lagrangian mass shells with time for the CCSN runs of the $19.7\,M_\odot$ progenitor with standard value of $\Delta M = 0.05\,M_\odot$ for the fixed mass in the energy-injection layer and a representative energy-deposition timescale of 1 s: uncollapsed (top), collapsed (middle) with deep inner grid boundary, and collapsed with inner grid boundary shifted farther out (bottom). The thin black solid lines are the mass shells, spaced in steps of $0.025\,M_\odot$, the blue line marks the shock radius, the red line indicates $R_{\rm OBED}$, and the yellow line $R_{\rm IBED}$. Crosses indicate the moment when the peak temperature of each mass shell is reached; their colors correspond to temperature values as given by the color bar. Vertical lines indicate the start and the end of the energy deposition.

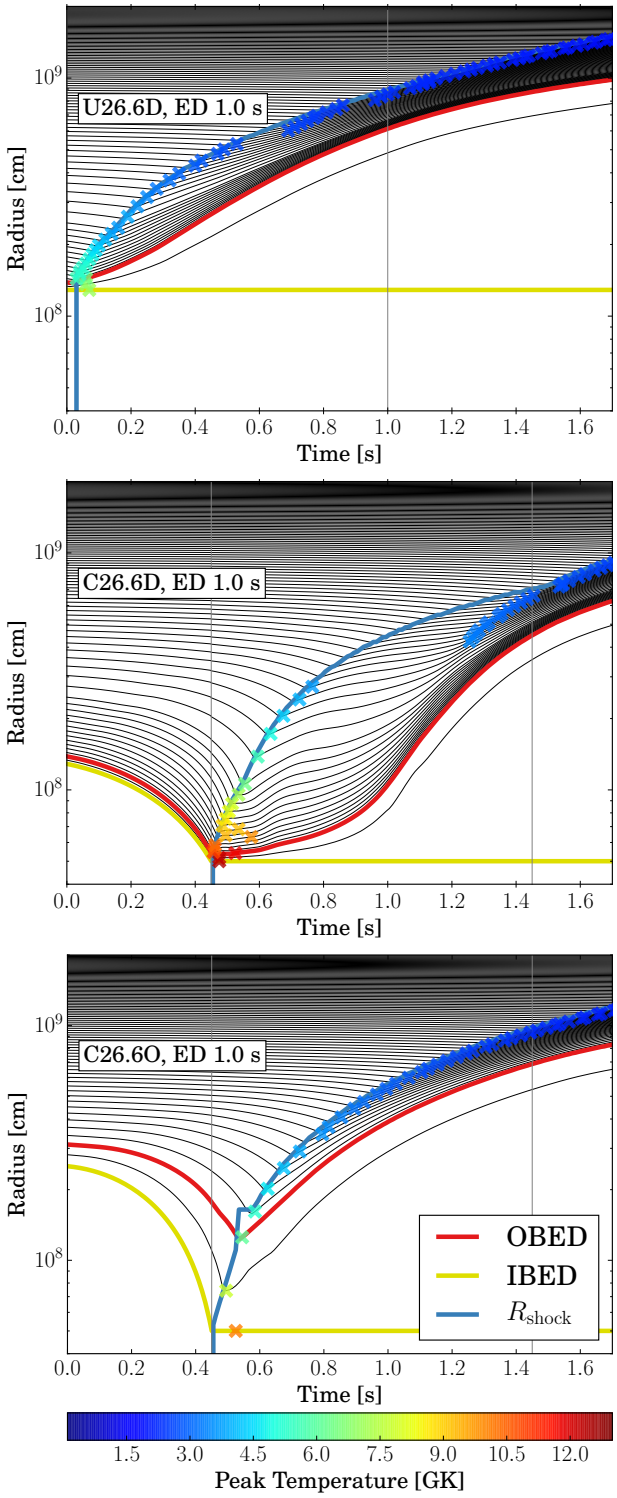


Figure C.2: Same as Figure C.1, but for the $26.6 M_{\odot}$ model.

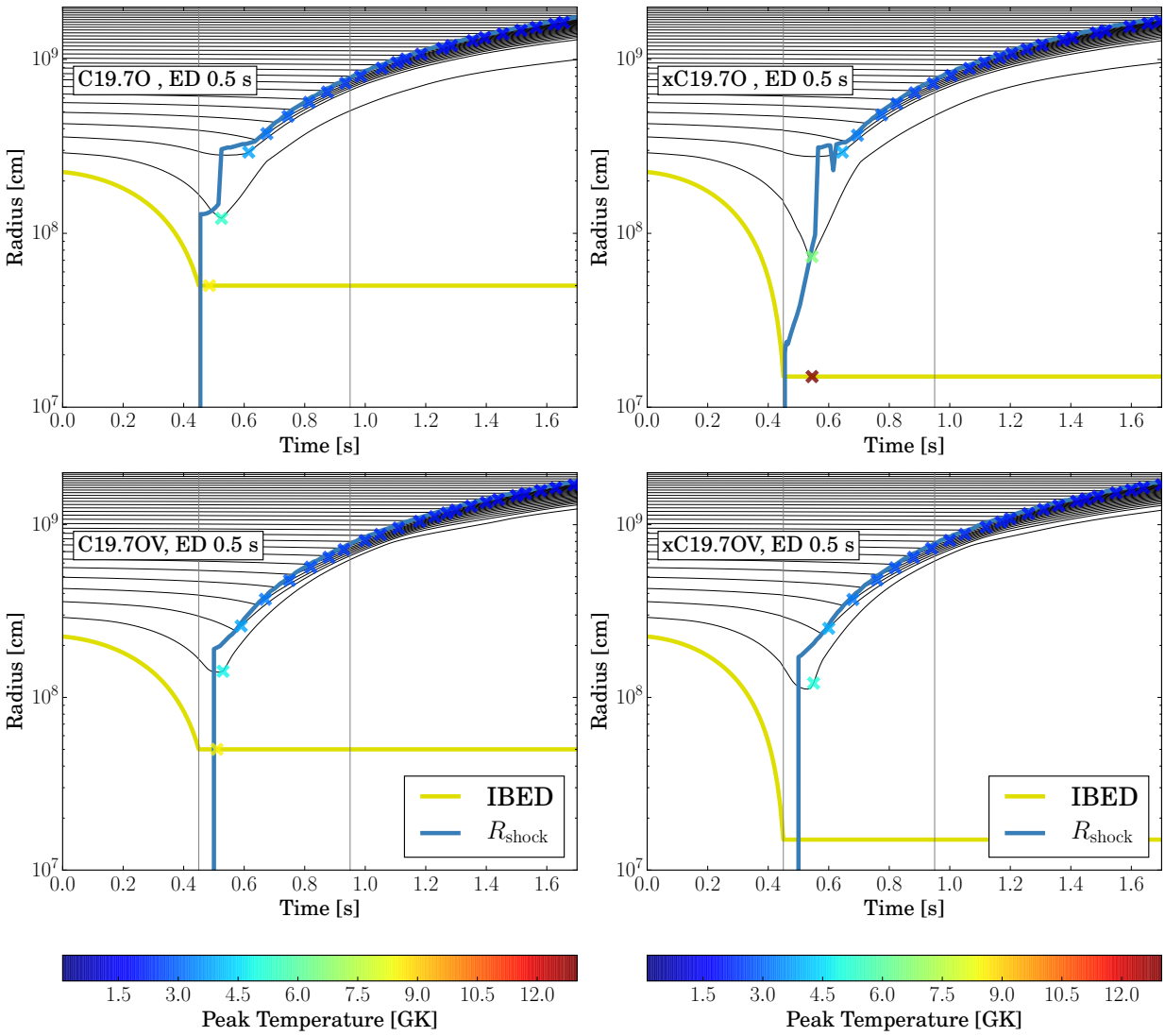


Figure C.3: Radius evolution of Lagrangian mass shells with time for the CCSN runs of the $19.7\,M_\odot$ progenitor with a representative energy-deposition timescale of 0.5 s: the fixed mass of the energy deposition with collapse to the $r_{\rm min} = 500$ km (top left), the fixed mass of the energy deposition with collapse to the $r_{\rm min} = 150$ km (top right), the fixed volume of the energy deposition with collapse to the $r_{\rm min} = 500$ km (bottom left) and the fixed volume of the energy deposition with collapse to the $r_{\rm min} = 150$ km (bottom right). The thin black solid lines are the mass shells, spaced in steps of $0.025\,M_\odot$, the blue line marks the shock radius, and the inner boundary is indicated by the yellow. Crosses indicate the moment when the peak temperature of each mass shell is reached; their colors correspond to temperature values as given by the color bar in Figure 3.6. Vertical lines indicate the start and the end of the energy deposition.

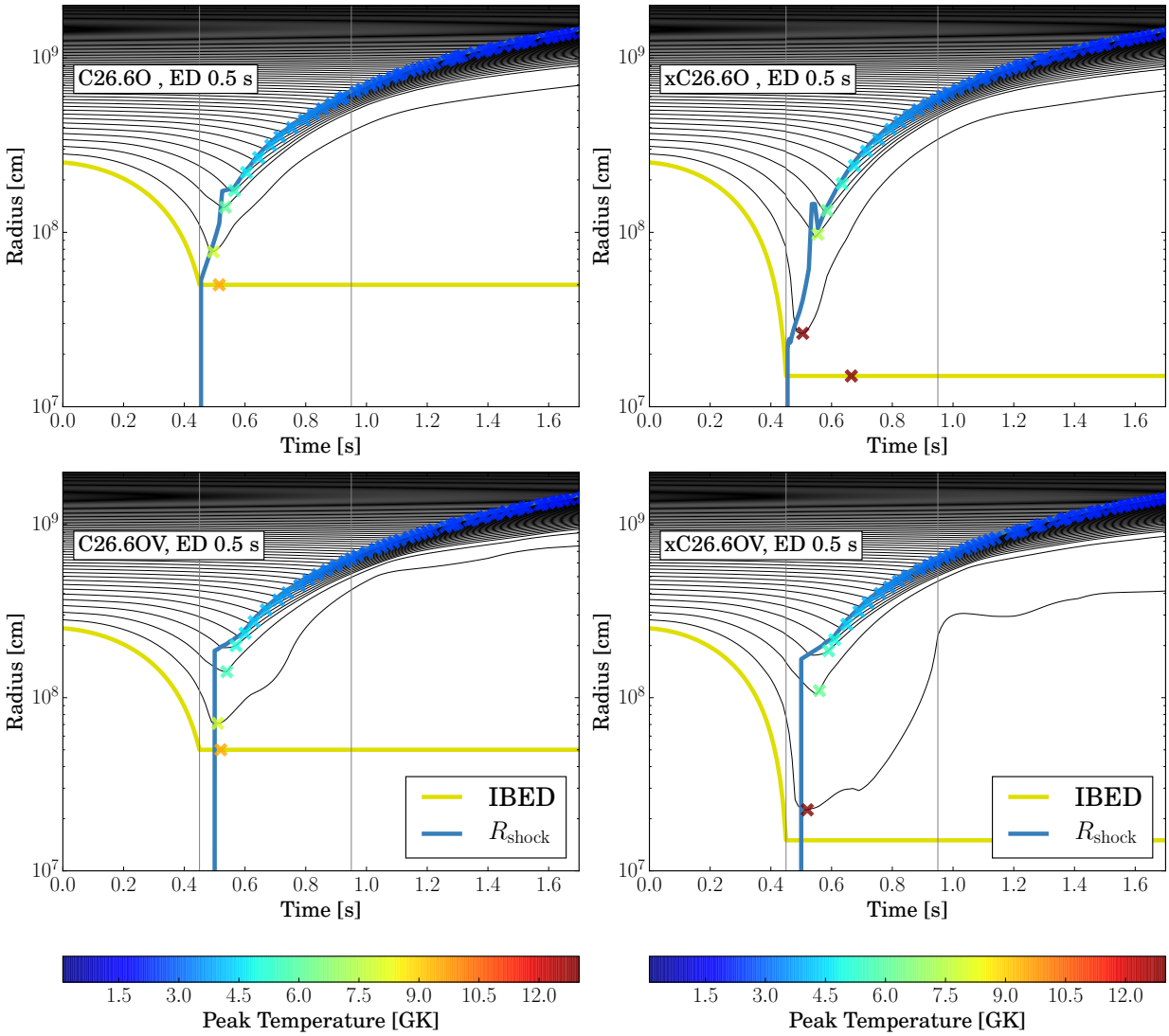


Figure C.4: Same as Figure C.3, but for the $26.6 M_{\odot}$ model.

inner boundary, indicating that this mass might fall back onto the proto-neutron star at later times. This does not happen for the $19.7M_{\odot}$ progenitor (see the lower right panel of Figure C.3) due to its low density in this region.

Overall, the results for the $19.7M_{\odot}$ and $26.6M_{\odot}$ progenitors in Figures C.1-C.4 are in agreement with the results for the $21.0M_{\odot}$ progenitor, shown in Figures 3.6 and 4.3, with the main differences coming from the progenitors structure, specifically the density behavior close to the inner boundary.

# Bibliography


Aguilera-Dena, D. R., Müller, B., Antoniadis, J., Langer, N., Dessart, L., Vigna-Gómez, A., and Yoon, S.-C. (2022). Stripped-envelope stars in different metallicity environments. II. Type I supernovae and compact remnants. *arXiv e-prints*, page arXiv:2204.00025.

Aloy, M. A., Müller, E., Ibáñez, J. M., Martí, J. M., and MacFadyen, A. (2000). Relativistic Jets from Collapsars. *The Astrophysical Journal Letters*, 531(2):L119–L122.

Arcones, A., Janka, H. T., and Scheck, L. (2007). Nucleosynthesis-relevant conditions in neutrino-driven supernova outflows. I. Spherically symmetric hydrodynamic simulations. *Astronomy and Astrophysics*, 467(3):1227–1248.

Arcones, A. and Thielemann, F. K. (2013). Neutrino-driven wind simulations and nucleosynthesis of heavy elements. *Journal of Physics G Nuclear Physics*, 40(1):013201.

Arnett, W. D., Bahcall, J. N., Kirshner, R. P., and Woosley, S. E. (1989). Supernova 1987A. *Annual Review of Astronomy and Astrophysics*, 27:629–700.

Aufderheide, M. B., Baron, E., and Thielemann, F. K. (1991). Shock Waves and Nucleosynthesis in Type II Supernovae. *Astrophysical Journal*, 370:630.

Bethe, H. A. (1990). Supernova mechanisms. *Reviews of Modern Physics*, 62(4):801–866.

Bollig, R., Yadav, N., Kresse, D., Janka, H.-T., Müller, B., and Heger, A. (2021). Self-consistent 3D Supernova Models From -7 Minutes to +7 s: A 1-bethe Explosion of a 19 $M_\odot$ Progenitor. *Astrophysical Journal*, 915(1):28.

Bouchet, P., Phillips, M. M., Suntzeff, N. B., Gouiffes, G., Hanuschik, R. W., and Wooden, D. H. (1991). The bolometric light curve of SN 1987A. II. Results from visible and infrared spectrophotometry. *Astronomy and Astrophysics*, 245:490.

Bruenn, S. W., Lentz, E. J., Hix, W. R., Mezzacappa, A., Harris, J. A., Messer, O. E. B., Endeve, E., Blondin, J. M., Chertkow, M. A., Lingerfelt, E. J., Marronetti, P., and Yakunin, K. N. (2016). The Development of Explosions in Axisymmetric Ab Initio Core-collapse Supernova Simulations of 12-25 M Stars. *Astrophysical Journal*, 818(2):123.

Burbidge, E. M., Burbidge, G. R., Fowler, W. A., and Hoyle, F. (1957). Synthesis of the Elements in Stars. *Reviews of Modern Physics*, 29(4):547–650.

Burrows, A., Radice, D., Vartanyan, D., Nagakura, H., Skinner, M. A., and Dolence, J. C. (2020). The overarching framework of core-collapse supernova explosions as revealed by 3D FORNAX simulations. *Monthly Notices of the Royal Astronomical Society*, 491(2):2715–2735.

Burrows, A. and Vartanyan, D. (2021). Core-collapse supernova explosion theory. *Nature*, 589(7840):29–39.

Chatzopoulos, E., Couch, S. M., Arnett, W. D., and Timmes, F. X. (2016). Convective Properties of Rotating Two-dimensional Core-collapse Supernova Progenitors. *Astrophysical Journal*, 822(2):61.

Couch, S. M. and Ott, C. D. (2015). The Role of Turbulence in Neutrino-driven Core-collapse Supernova Explosions. *Astrophysical Journal*, 799(1):5.

Couch, S. M., Warren, M. L., and O'Connor, E. P. (2020). Simulating Turbulence-aided Neutrino-driven Core-collapse Supernova Explosions in One Dimension. *Astrophysical Journal*, 890(2):127.

Curtis, S., Ebinger, K., Fröhlich, C., Hempel, M., Perego, A., Liebendörfer, M., and Thielemann, F.-K. (2019). PUSHing Core-collapse Supernovae to Explosions in Spherical Symmetry. III. Nucleosynthesis Yields. *Astrophysical Journal*, 870(1):2.

Demorest, P. B., Pennucci, T., Ransom, S. M., Roberts, M. S. E., and Hessels, J. W. T. (2010). A two-solar-mass neutron star measured using Shapiro delay. *Nature*, 467(7319):1081–1083.

Ebinger, K., Curtis, S., Fröhlich, C., Hempel, M., Perego, A., Liebendörfer, M., and Thielemann, F.-K. (2019). PUSHing Core-collapse Supernovae to Explosions in Spherical Symmetry. II. Explodability and Remnant Properties. *Astrophysical Journal*, 870(1):1.

Ebinger, K., Curtis, S., Ghosh, S., Fröhlich, C., Hempel, M., Perego, A., Liebendörfer, M., and Thielemann, F.-K. (2020). PUSHing Core-collapse Supernovae to Explosions in Spherical Symmetry. IV. Explodability, Remnant Properties, and Nucleosynthesis Yields of Low-metallicity Stars. *Astrophysical Journal*, 888(2):91.

Ertl, T. (2016). *Modelin Neutrino-Driven Supernova Explosions Across the Stellar Mass and Metallicity Range*. PhD thesis.

Ertl, T., Janka, H. T., Woosley, S. E., Sukhbold, T., and Ugliano, M. (2016). A Two-parameter Criterion for Classifying the Explodability of Massive Stars by the Neutrino-driven Mechanism. *Astrophysical Journal*, 818(2):124.

Ertl, T., Woosley, S. E., Sukhbold, T., and Janka, H. T. (2020). The Explosion of Helium Stars Evolved with Mass Loss. *Astrophysical Journal*, 890(1):51.

Foglizzo, T., Kazeroni, R., Guilet, J., Masset, F., González, M., Krueger, B. K., Novak, J., Oertel, M., Margueron, J., Faure, J., Martin, N., Blottiau, P., Peres, B., and Durand, G. (2015). The Explosion Mechanism of Core-Collapse Supernovae: Progress in Supernova Theory and Experiments. *Publications of the Astronomical Society of Australia*, 32:e009.

Fowler, W. A., Caughlan, G. R., and Zimmerman, B. A. (1975). Thermonuclear Reaction Rates, II. *Annual Review of Astronomy and Astrophysics*, 13:69.

Ghahramany, N., Gharaati, S., and Ghanaatian, M. (2012). New approach to nuclear binding energy in integrated nuclear model. *Journal of Theoretical and Applied Physics*, 6:3.

Glas, R., Janka, H. T., Melson, T., Stockinger, G., and Just, O. (2019). Effects of LESA in Three-dimensional Supernova Simulations with Multidimensional and Ray-by-ray-plus Neutrino Transport. *Astrophysical Journal*, 881(1):36.

Harris, J. A., Hix, W. R., Chertkow, M. A., Lee, C. T., Lentz, E. J., and Messer, O. E. B. (2017). Implications for Post-processing Nucleosynthesis of Core-collapse Supernova Models with Lagrangian Particles. *Astrophysical Journal*, 843(1):2.

Hashimoto, M., Nomoto, K., and Shigeyama, T. (1989). Explosive nucleosynthesis in supernova 1987A. *Astronomy and Astrophysics*, 210:L5–L8.

Hayden, M. R., Bovy, J., Holtzman, J. A., Nidever, D. L., Bird, J. C., Weinberg, D. H., Andrews, B. H., Majewski, S. R., Allende Prieto, C., Anders, F., Beers, T. C., Bizyaev, D., Chiappini, C., Cunha, K., Frinchaboy, P., García-Herńandez, D. A., García Pérez, A. E., Girardi, L., Harding, P., Hearty, F. R., Johnson, J. A., Mészáros, S., Minchev, I., O'Connell, R., Pan, K., Robin, A. C., Schiavon, R. P., Schneider, D. P., Schultheis, M., Shetrone, M., Skrutskie, M., Steinmetz, M., Smith, V., Wilson, J. C., Zamora, O., and Zasowski, G. (2015). Chemical Cartography with APOGEE: Metallicity Distribution Functions and the Chemical Structure of the Milky Way Disk. *Astrophysical Journal*, 808(2):132.

Hester, J. J. (2008). The Crab Nebula : an astrophysical chimera. *Annual Review of Astronomy and Astrophysics*, 46:127–155.

Hoyle, F., Fowler, W. A., Burbidge, G. R., and Burbidge, E. M. (1956). Origin of the Elements in Stars. *Science*, 124(3223):611–614.

Imasheva, L., Janka, H. T., and Weiss, A. (2022). Parameterisations of thermal bomb explosions for core-collapse supernovae and 56Ni production. *arXiv e-prints*, page arXiv:2209.10989.

Iwamoto, K., Nomoto, K., Höflich, P., Yamaoka, H., Kumagai, S., and Shigeyama, T. (1994). Theoretical Light Curves for the Type IC Supernova SN 1994I. *The Astrophysical Journal Letters*, 437:L115.

Janka, H. T., Langanke, K., Marek, A., Martínez-Pinedo, G., and Müller, B. (2007). Theory of core-collapse supernovae. *Physics Reports*, 442(1-6):38–74.

Janka, H.-T., Melson, T., and Summa, A. (2016). Physics of Core-Collapse Supernovae in Three Dimensions: A Sneak Preview. *Annual Review of Nuclear and Particle Science*, 66(1):341–375.

Janka, H. T. and Müller, E. (1996). Neutrino heating, convection, and the mechanism of Type-II supernova explosions. *Astronomy and Astrophysics*, 306:167.

Khokhlov, A. M., Höflich, P. A., Oran, E. S., Wheeler, J. C., Wang, L., and Chtchelkanova, A. Y. (1999). Jet-induced Explosions of Core Collapse Supernovae. *The Astrophysical Journal Letters*, 524(2):L107–L110.

Kifonidis, K., Plewa, T., Janka, H. T., and Müller, E. (2000). Nucleosynthesis and Clump Formation in a Core-Collapse Supernova. *The Astrophysical Journal Letters*, 531(2):L123–L126.

Kifonidis, K., Plewa, T., Janka, H. T., and Müller, E. (2003). Non-spherical core collapse supernovae. I. Neutrino-driven convection, Rayleigh-Taylor instabilities, and the formation and propagation of metal clumps. *Astronomy and Astrophysics*, 408:621–649.

Kifonidis, K., Plewa, T., Scheck, L., Janka, H. T., and Müller, E. (2006). Non-spherical core collapse supernovae. II. The late-time evolution of globally anisotropic neutrino-driven explosions and their implications for SN 1987 A. *Astronomy and Astrophysics*, 453(2):661–678.

Kobayashi, C., Karakas, A. I., and Lugaro, M. (2020). The Origin of Elements from Carbon to Uranium. *Astrophysical Journal*, 900(2):179.

Lentz, E. J., Bruenn, S. W., Hix, W. R., Mezzacappa, A., Messer, O. E. B., Endeve, E., Blondin, J. M., Harris, J. A., Marronetti, P., and Yakunin, K. N. (2015). Three-dimensional Core-collapse Supernova Simulated Using a 15 M $_{\odot}$ Progenitor. *The Astrophysical Journal Letters*, 807(2):L31.

Liebendörfer, M. (2005). A Simple Parameterization of the Consequences of Deleptonization for Simulations of Stellar Core Collapse. *Astrophysical Journal*, 633(2):1042–1051.

Lippuner, J. and Roberts, L. F. (2017). SkyNet: A Modular Nuclear Reaction Network Library. *The Astrophysical Journal Supplement*, 233(2):18.

MacFadyen, A. I. and Woosley, S. E. (1999). Collapsars: Gamma-Ray Bursts and Explosions in "Failed Supernovae". *Astrophysical Journal*, 524(1):262–289.

MacFadyen, A. I., Woosley, S. E., and Heger, A. (2001). Supernovae, Jets, and Collapsars. *Astrophysical Journal*, 550(1):410–425.

Maeda, K. and Nomoto, K. (2003). Bipolar Supernova Explosions: Nucleosynthesis and Implications for Abundances in Extremely Metal-Poor Stars. *Astrophysical Journal*, 598(2):1163–1200.

Matteucci, F. (2003). What determines galactic evolution? *Astrophysics and Space Science*, 284(2):539–548.

Moriya, T., Tominaga, N., Tanaka, M., Nomoto, K., Sauer, D. N., Mazzali, P. A., Maeda, K., and Suzuki, T. (2010). Fallback Supernovae: A Possible Origin of Peculiar Supernovae with Extremely Low Explosion Energies. *Astrophysical Journal*, 719(2):1445–1453.

Morozova, V., Piro, A. L., Renzo, M., Ott, C. D., Clausen, D., Couch, S. M., Ellis, J., and Roberts, L. F. (2015). Light Curves of Core-collapse Supernovae with Substantial Mass Loss Using the New Open-source SuperNova Explosion Code (SNEC). *Astrophysical Journal*, 814(1):63.

Müller, B. (2015). The dynamics of neutrino-driven supernova explosions after shock revival in 2D and 3D. *Monthly Notices of the Royal Astronomical Society*, 453(1):287–310.

Müller, B., Heger, A., Liptai, D., and Cameron, J. B. (2016). A simple approach to the supernova progenitor-explosion connection. *Monthly Notices of the Royal Astronomical Society*, 460(1):742–764.

Müller, B., Melson, T., Heger, A., and Janka, H.-T. (2017a). Supernova simulations from a 3D progenitor model - Impact of perturbations and evolution of explosion properties. *Monthly Notices of the Royal Astronomical Society*, 472(1):491–513.

Müller, B., Tauris, T. M., Heger, A., Banerjee, P., Qian, Y.-Z., Powell, J., Chan, C., Gay, D. W., and Langer, N. (2019). Three-dimensional simulations of neutrino-driven core-collapse supernovae from low-mass single and binary star progenitors. *Monthly Notices of the Royal Astronomical Society*, 484(3):3307–3324.

Müller, E. (1986). Nuclear-reaction networks and stellar evolution codes - The coupling of composition changes and energy release in explosive nuclear burning. *Astronomy and Astrophysics*, 162(1-2):103–108.

Müller, T., Prieto, J. L., Pejcha, O., and Clocchiatti, A. (2017b). The Nickel Mass Distribution of Normal Type II Supernovae. *Astrophysical Journal*, 841(2):127.

Murphy, J. W., Dolence, J. C., and Burrows, A. (2013). The Dominance of Neutrino-driven Convection in Core-collapse Supernovae. *Astrophysical Journal*, 771(1):52.

Nagataki, S., Hashimoto, M.-a., Sato, K., and Yamada, S. (1997). Explosive Nucleosynthesis in Axisymmetrically Deformed Type II Supernovae. *Astrophysical Journal*, 486(2):1026–1035.

Nagataki, S., Mizuta, A., and Sato, K. (2006). Explosive Nucleosynthesis in GRB Jets Accompanied by Hypernovae. *Astrophysical Journal*, 647(2):1255–1268.

Nagataki, S., Mizuta, A., Yamada, S., Takabe, H., and Sato, K. (2003). Explosive Nucleosynthesis Associated with Formation of Jet-induced Gamma-Ray Bursts in Massive Stars. *Astrophysical Journal*, 596(1):401–413.

Nakamura, T., Umeda, H., Iwamoto, K., Nomoto, K., Hashimoto, M.-a., Hix, W. R., and Thielemann, F.-K. (2001). Explosive Nucleosynthesis in Hypernovae. *Astrophysical Journal*, 555(2):880–899.

Nomoto, K., Sparks, W. M., Fesen, R. A., Gull, T. R., Miyaji, S., and Sugimoto, D. (1982). The Crab Nebula's progenitor. *Nature*, 299(5886):803–805.

Nomoto, K., Tominaga, N., Umeda, H., Kobayashi, C., and Maeda, K. (2006). Nucleosynthesis yields of core-collapse supernovae and hypernovae, and galactic chemical evolution. *Nuclear Physics A*, 777:424–458.

Obergaulinger, M. and Aloy, M. Á. (2021). Magnetorotational core collapse of possible GRB progenitors - III. Three-dimensional models. *Monthly Notices of the Royal Astronomical Society*, 503(4):4942–4963.

O'Connor, E. and Ott, C. D. (2011). Black Hole Formation in Failing Core-Collapse Supernovae. *Astrophysical Journal*, 730(2):70.

Ott, C. D., Roberts, L. F., da Silva Schneider, A., Fedrow, J. M., Haas, R., and Schnetter, E. (2018). The Progenitor Dependence of Core-collapse Supernovae from Three-dimensional Simulations with Progenitor Models of 12-40 M $_{\odot}$. *The Astrophysical Journal Letters*, 855(1):L3.

Palme, H., Lodders, K., and Jones, A. (2014). Solar System Abundances of the Elements. In Davis, A. M., editor, *Planets, Asteriods, Comets and The Solar System*, volume 2, pages 15–36.

Paxton, B., Marchant, P., Schwab, J., Bauer, E. B., Bildsten, L., Cantiello, M., Dessart, L., Farmer, R., Hu, H., Langer, N., Townsend, R. H. D., Townsley, D. M., and Timmes, F. X. (2015). Modules for Experiments in Stellar Astrophysics (MESA): Binaries, Pulsations, and Explosions. *The Astrophysical Journal Supplement*, 220(1):15.

Pejcha, O. and Thompson, T. A. (2015). The Landscape of the Neutrino Mechanism of Core-collapse Supernovae: Neutron Star and Black Hole Mass Functions, Explosion Energies, and Nickel Yields. *Astrophysical Journal*, 801(2):90.

Perego, A., Hempel, M., Fröhlich, C., Ebinger, K., Eichler, M., Casanova, J., Liebendörfer, M., and Thielemann, F. K. (2015). PUSHing Core-collapse Supernovae to Explosions in Spherical Symmetry I: the Model and the Case of SN 1987A. *Astrophysical Journal*, 806(2):275.

Qian, Y. Z. and Woosley, S. E. (1996). Nucleosynthesis in Neutrino-driven Winds. I. The Physical Conditions. *Astrophysical Journal*, 471:331.

Radice, D., Ott, C. D., Abdikamalov, E., Couch, S. M., Haas, R., and Schnetter, E. (2016). Neutrino-driven Convection in Core-collapse Supernovae: High-resolution Simulations. *Astrophysical Journal*, 820(1):76.

Sandoval, M. A., Hix, W. R., Messer, O. E. B., Lentz, E. J., and Harris, J. A. (2021). Three-dimensional Core-collapse Supernova Simulations with 160 Isotopic Species Evolved to Shock Breakout. *Astrophysical Journal*, 921(2):113.

Sawada, R. and Maeda, K. (2019). Nucleosynthesis Constraints on the Energy Growth Timescale of a Core-collapse Supernova Explosion. *Astrophysical Journal*, 886(1):47.

Scheck, L., Kifonidis, K., Janka, H.-T., and Müller, E. (2006). Multidimensional supernova simulations with approximative neutrino transport. I. Neutron star kicks and the anisotropy of neutrino-driven explosions in two spatial dimensions. *Astronomy and Astrophysics*, 457:963–986.

Schneider, F. R. N., Podsiadlowski, P., and Müller, B. (2021). Pre-supernova evolution, compact-object masses, and explosion properties of stripped binary stars. *Astronomy and Astrophysics*, 645:A5.

Shigeyama, T., Nomoto, K., and Hashimoto, M. (1988). Hydrodynamical models and the light curve of Supernova 1987A in the Large Magellanic Cloud. *Astronomy and Astrophysics*, 196:141–151.

Shimizu, T. M., Ebisuzaki, T., Sato, K., and Yamada, S. (2001). Effect of Anisotropic Neutrino Radiation on Supernova Explosion Energy. *Astrophysical Journal*, 552(2):756–781.

Siegel, D. M., Barnes, J., and Metzger, B. D. (2019). Collapsars as a major source of r-process elements. *Nature*, 569(7755):241–244.

Smith, N. (2013). The Crab nebula and the class of Type IIn-P supernovae caused by sub-energetic electron-capture explosions. *Monthly Notices of the Royal Astronomical Society*, 434(1):102–113.

Sukhbold, T., Ertl, T., Woosley, S. E., Brown, J. M., and Janka, H. T. (2016). Core-collapse Supernovae from 9 to 120 Solar Masses Based on Neutrino-powered Explosions. *Astrophysical Journal*, 821(1):38.

Sukhbold, T. and Woosley, S. E. (2014). The Compactness of Presupernova Stellar Cores. *Astrophysical Journal*, 783(1):10.

Suntzeff, N. B., Phillips, M. M., Elias, J. H., Depoy, D. L., and Walker, A. R. (1992). The Energy Sources Powering the Late-Time Bolometric Evolution of SN 1987A. *The Astrophysical Journal Letters*, 384:L33.

Suwa, Y., Tominaga, N., and Maeda, K. (2019). Importance of $^{56}$Ni production on diagnosing explosion mechanism of core-collapse supernova. *Monthly Notices of the Royal Astronomical Society*, 483(3):3607–3617.

Takiwaki, T., Kotake, K., and Suwa, Y. (2014). A Comparison of Two- and Three-dimensional Neutrino-hydrodynamics Simulations of Core-collapse Supernovae. *Astrophysical Journal*, 786(2):83.

Thielemann, F.-K., Hashimoto, M.-A., and Nomoto, K. (1990). Explosive Nucleosynthesis in SN 1987A. II. Composition, Radioactivities, and the Neutron Star Mass. *Astrophysical Journal*, 349:222.

Thielemann, F.-K., Nomoto, K., and Hashimoto, M.-A. (1996). Core-Collapse Supernovae and Their Ejecta. *Astrophysical Journal*, 460:408.

Timmes, F. X., Woosley, S. E., and Weaver, T. A. (1995). Galactic Chemical Evolution: Hydrogen through Zinc. *The Astrophysical Journal Supplement*, 98:617.

Ugliano, M. (2012). *Explosion and Remnant Systematics for Core-Collapse Supernovae in one Dimension*. PhD thesis.

Ugliano, M., Janka, H.-T., Marek, A., and Arcones, A. (2012). Progenitor-explosion Connection and Remnant Birth Masses for Neutrino-driven Supernovae of Iron-core Progenitors. *Astrophysical Journal*, 757(1):69.

Umeda, H. and Nomoto, K. (2002). Nucleosynthesis of Zinc and Iron Peak Elements in Population III Type II Supernovae: Comparison with Abundances of Very Metal Poor Halo Stars. *Astrophysical Journal*, 565(1):385–404.

Umeda, H. and Nomoto, K. (2008). How Much $^{56}$Ni Can Be Produced in Core-Collapse Supernovae? Evolution and Explosions of 30-100 $M_\odot$ Stars. *Astrophysical Journal*, 673(2):1014–1022.

Umeda, H. and Yoshida, T. (2017). Nucleosynthesis in Spherical Explosion Models of Core-Collapse Supernovae. In Alsabti, A. W. and Murdin, P., editors, *Handbook of Supernovae*, page 1753. Cham, Switzerland: Springer Nature.

Utrobin, V. P., Wongwathanarat, A., Janka, H. T., and Müller, E. (2015). Supernova 1987A: neutrino-driven explosions in three dimensions and light curves. *Astronomy and Astrophysics*, 581:A40.

Valerin, G., Pumo, M. L., Pastorello, A., Reguitti, A., Elias-Rosa, N., Gútierrez, C. P., Kankare, E., Fraser, M., Mazzali, P. A., Howell, D. A., Kotak, R., Galbany, L., Williams, S. C., Cai, Y. Z., Salmaso, I., Pinter, V., Müller-Bravo, T. E., Burke, J., Padilla Gonzalez, E., Hiramatsu, D., McCully, C., Newsome, M., and Pellegrino, C. (2022). Low luminosity Type II supernovae - IV. SN 2020cxd and SN 2021aai, at the edges of the sub-luminous supernovae class. *eprint*, arXiv:2203.03988.

Weaver, T. A., Zimmerman, G. B., and Woosley, S. E. (1978). Presupernova evolution of massive stars. *Astrophysical Journal*, 225:1021–1029.

Wirth, H., Jerabkova, T., Yan, Z., Kroupa, P., Haas, J., and Šubr, L. (2021). How many explosions does one need? Quantifying supernovae in globular clusters from iron abundance spreads. *Monthly Notices of the Royal Astronomical Society*, 506(3):4131–4138.

Wongwathanarat, A., Janka, H.-T., and Müller, E. (2010). Hydrodynamical Neutron Star Kicks in Three Dimensions. *The Astrophysical Journal Letters*, 725(1):L106–L110.

Wongwathanarat, A., Janka, H. T., and Müller, E. (2013). Three-dimensional neutrino-driven supernovae: Neutron star kicks, spins, and asymmetric ejection of nucleosynthesis products. *Astronomy and Astrophysics*, 552:A126.

Wongwathanarat, A., Janka, H.-T., Müller, E., Pllumbi, E., and Wanajo, S. (2017). Production and Distribution of $^{44}$Ti and $^{56}$Ni in a Three-dimensional Supernova Model Resembling Cassiopeia A. *Astrophysical Journal*, 842(1):13.

Wongwathanarat, A., Müller, E., and Janka, H. T. (2015). Three-dimensional simulations of core-collapse supernovae: from shock revival to shock breakout. *Astronomy and Astrophysics*, 577:A48.

Woosley, S. E. (1988). SN 1987A: After the Peak. *Astrophysical Journal*, 330:218.

Woosley, S. E. and Heger, A. (2007). Nucleosynthesis and remnants in massive stars of solar metallicity. *Physics Reports*, 442(1-6):269–283.

Woosley, S. E., Heger, A., and Weaver, T. A. (2002). The evolution and explosion of massive stars. *Reviews of Modern Physics*, 74(4):1015–1071.

Woosley, S. E. and Hoffman, R. D. (1992). The alpha -Process and the r-Process. *Astrophysical Journal*, 395:202.

Woosley, S. E. and Weaver, T. A. (1995). The Evolution and Explosion of Massive Stars. II. Explosive Hydrodynamics and Nucleosynthesis. *The Astrophysical Journal Supplement*, 101:181.

Yamamoto, Y., Fujimoto, S.-i., Nagakura, H., and Yamada, S. (2013). Post-shock-revival Evolution in the Neutrino-heating Mechanism of Core-collapse Supernovae. *Astrophysical Journal*, 771(1):27.

Yang, H. and Chevalier, R. A. (2015). Evolution of the Crab Nebula in a Low Energy Supernova. *Astrophysical Journal*, 806(2):153.

Yang, S., Sollerman, J., Strotjohann, N. L., Schulze, S., Lunnan, R., Kool, E., Fremling, C., Perley, D., Ofek, E., Schweyer, T., Bellm, E. C., Kasliwal, M. M., Masci, F. J., Rigault, M., and Yang, Y. (2021). A low-energy explosion yields the underluminous Type IIP SN 2020cxd. *Astronomy and Astrophysics*, 655:A90.

Young, P. A. and Fryer, C. L. (2007). Uncertainties in Supernova Yields. I. One-dimensional Explosions. *Astrophysical Journal*, 664(2):1033–1044.

Zhang, W., Woosley, S. E., and Heger, A. (2008). Fallback and Black Hole Production in Massive Stars. *Astrophysical Journal*, 679(1):639–654.

# Acknowledgements

First, I would like to say special thanks to my supervisor Achim Weiss for his scientific guidance, encouragement, and always constructive and very helpful feedback. I really appreciate the fun group and work environment created by him, and extremely thankful for giving me the opportunity to work at MPA. I am also very grateful to my second supervisor Thomas Janka, for his patience and for investing his time and effort in our work. I am thankful for all the lengthy discussions we had and for all his assistance, that I learned a lot from. They have been a constant support during the worldwide pandemic, not letting me fail with my project.

I am thankful to my office mate Felix for all the interesting discussions we had about being a PhD student and for his support when I was nervous or stressed about giving a talk, presenting my work in the group, or writing this thesis. Thank you to my colleague Eirini for always encouraging me to go a little bit further, and for being a great company, be it at a winter school, at a workshop, or organizing a journal club. I would also like to say special thanks to Bryce for his super helpful comments, his feedback greatly improved this work. I am extremely grateful to Thomas Ertl for introducing me to the code I worked with over my PhD, thank you for answering all of my questions and being very patient and kind. Moreover, I am thankful to Earl, Damien and Daniel for helping me to prepare for the exam, I really appreciate it!

I would like to thank the MPA secretary staff, Sonja, Maria, and Gabi. They really made my life in Munich much easier by helping me with the apartment search, German courses, getting residence permit, and all the other endless issues I had over the years. I want to thank the MPA admins, and especially Andi and Goran, for their help on every technical problem I had.

I am extremely grateful to my long-distance friends, that our friendships are still very strong over all these years. I want to thank Eldar for always being there for me, за все путешествия, интересные истории и яркие впечатления, всё это остаётся со мной. Moahan, I want to thank you for always listening to me, even when I repeat the same things a million times, for all the visits, words of encouragement and for your tremendous support especially during the very stressful time of writing this work. Я благодарна Лиде и Алине за все длинные дискуссии в видео сообщениях, за то что всегда были рядом, несмотря на то расстояние которое нас разделяет, и их поддержку в нелегкий период написания этой работы. Я благодарна Мише, Даше и Серёже за все звонки, сообщения и визиты. Обнимаю вас!

I am very grateful to my amazing army of friends whom I met here in Munich throughout these years. You guys made my day-to-day life here very enjoyable. I want to thank Yru, for being by my side from the very beginning to the end of my PhD. Marko, Mario and Danko, you are the best covid buddies a girl could ask for! I really appreciate your constant support and your company. I want to thank Rohan and Jonas for organizing many fun events, like poker games, movie nights, hikes and weekend trips, all of which significantly contributed to me feeling at home here. I want to thank Julia for her moral support during the writing of this work, and Ivan for running a Munich marathon with me. All the parties we had together with y'all, all the other activities, like baking cakes, rafting, cycling trips, it all left me with very warm memories and a lot of love.

Last but not least, I want to thank my family. Я благодарна папе за то, что активно поддерживал мой интерес к науке, и маме за то, что всегда была рядом. Особенная благодарность моим старшим сестрам, Алие и Ирине, за их бесконечную поддержку, за то, что всегда находят теплые слова и видят только лучшее во мне. Я очень люблю вас!